INTEGRATED AIR & MISSILE DEFENCE

CENTRE OF EXCELLENCE

Analysis of the Related Physical Phenomena and Aerodynamic Performance of Hypersonic Vehicle(s) and Possible Ways of Exploiting Those Data in Order to Improve Surveillance Capabilities

Mar 2024

EXTENDED ABSTRACT

	"Analysis of the related Physical Phenomena and Aerodynamic Performance of Hypersonic Vehicle(s) and possible ways of exploiting those data in order to improve Surveillance Capabilities"
Angelos Klothakis *Ph.D. Candidate* *Dr. Ioannis K. Nikolos* *Professor*	*(Item – 1) Writing and delivery of a study report under the subject: "Analysis of the related Physical Phenomena and Aerodynamic Performance of Hypersonic Vehicle(s) and possible ways of exploiting those data in order to improve Surveillance Capabilities."*

Chania, March 30, 2024

Summary

The main objectives of this Report are the following: a) firstly, to review some of the available design methodologies proposed for the design of waverider hypersonic vehicles, b), to apply such a methodology for the design of a typical waverider hypersonic vehicle under specific flight conditions, c) to simulate the hypersonic flow around this vehicle in order to evaluate the design itself and to provide an insight to the related flow phenomena (at an altitude of 90 km, using the open-source SPARTA DSMC simulation software), d) to design and simulate a preliminary two-dimensional geometry of a scramjet-powered hypersonic vehicle, e) to design a typical scramjet-powered hypersonic three-dimensional vehicle (based on the geometry of the successful X-51A vehicle), f) to simulate the aforementioned vehicle and derive flow properties for specific flow conditions (at an altitude of 90 km, using SPARTA DSMC simulation software), g) to simulate the designed waverider vehicle at lower altitudes (45 km, 30 km), using SU2 an open-source, non-equilibrium Navier-Stokes solver, h) to take a first look to the sensing problem of a hypersonic vehicle. Finally, some conclusions are addressed, based on the findings of this work.

Acknowledgement

1. Introduction to waveriders

The potential benefits derived from the practical implementation of reusable hypersonic flight vehicles are desirable for all developed societies. However, the natural phenomena that occur during a hypersonic flight within the atmosphere introduce technological challenges that render the design and development of such a vehicle a very difficult task. The technical complexities associated with the development of reusable hypersonic vehicles that are capable of controlled performance while withstanding sustained high temperature in a low-density aerodynamic environment are enormous. These natural phenomena, which define hypersonic speeds, are discussed by Anderson [1] and are listed below:

- shock waves, causing large flow and entropy gradients,
- high level of viscous interaction between the fluid and the vehicle geometry, causing high heat flux and thick boundary layers,
- thin shock layers, due to the close vicinity of the shock to the surface of the vehicle, trapping high temperature flow around the hypersonic vehicle.

All the aforementioned physical phenomena produce large heat loads, which pose a challenge to materials to endure for long time periods. Therefore, material options for hypersonic vehicles are very slim and the residence time in the hypersonic regime very limited. The major technological challenges are the undesirable properties of existing materials and limited capabilities of existing thermal protection systems.

Furthermore, there are limited options and capabilities of current propulsion systems to provide and sustain the thrust required for hypersonic speeds. This is the main reason why most of the successful hypersonic crafts, such as missiles and spacecraft, use rockets to provide the thrust needed to achieve hypersonic speeds. Rockets, which have proven to be very effective, are expensively inefficient and dangerous. The required fuel accounts for a large portion of the take-off weight and success of rocket propulsion requires a very accurate and precise design. Alternatively, with the recent successful test flights of the X-51A [2] and X-43A [3], the scramjet is showing promise as another feasible option for hypersonic propulsion. The scramjet is a dynamic thrust airbreathing propulsion system that uses oxygen from the atmosphere. This feature dramatically decreases the weight of the required onboard fuel and entails higher performance efficiency than rockets, as shown in Figure 1.

Research efforts are also made in the design of the Magneto-HydroDynamics (MHD) supersonic turbojet engine [4], which is projected to be capable of operational speeds of Mach 0-7, utilizing existing technology. Both the scramjet and MHD supersonic turbojet are immature technologies still undergoing research studies and are not yet ready for extensive practical use.
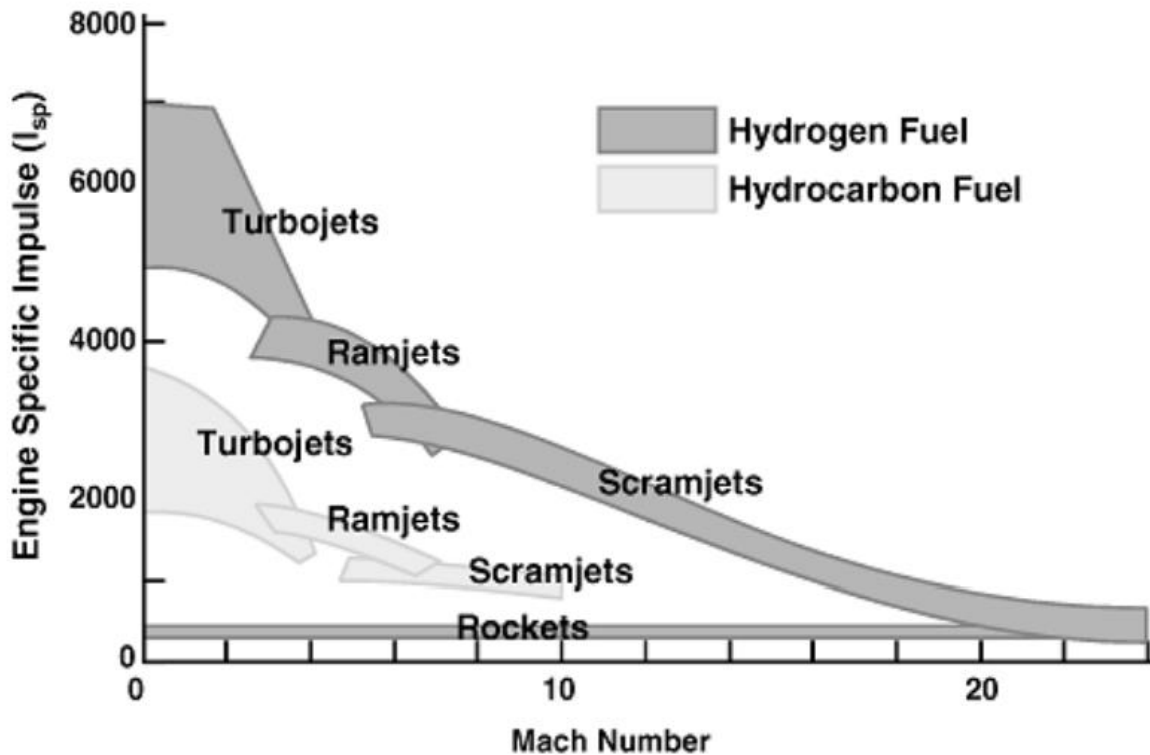
Figure 1: Mach number versus Specific Impulse, for various propulsion systems [5, 6].

A waverider is a hypersonic vehicle configuration designed in such a way that the shock wave emanating from the vehicle itself stays attached to the vehicle's leading edge, providing several benefits [7]: (a) the shock separates the flow filed on the upper surface from the flow field on the lower surface of the vehicle, therefore no spillage of high-pressure flow takes place from the lower to the upper surface at the tip; (b). the uniform flow on the lower surface is ideal for entering a scramjet engine; (c) the geometry configuration of the waverider can be achieved through an inverse design methodology from a known flow filed around a conical geometry. Such a methodology will be used in the following sections of this work.

The waverider concept was introduced by Nonweiler [8] in 1963, but the technology of that time was incapable of producing a hypersonic air-breathing vehicle. In the work of Sandlin and Pessin [9] a detailed description of the methodology used to design a waverider is provided. A comprehensive review of the most serious design issues of hypersonic flight vehicles can be found in the work of Sziroczak and Smith [10], where two distinct classes of vehicles are reviewed, namely hypersonic transports and space launchers; although different than waveriders, most of the design and construction issues are common. In the work of Zhang et al. [11] the three-dimensional class/shape function transformation (CST) approach is used to define the geometrical shapes of hypersonic gliding vehicles (HGVs). Inviscid methods, based on modified Newton theory and Prandtl–Meyer equation, are employed to estimate the vehicle's aerodynamic properties. In order to obtain vehicles with high lift-to-drag ratio as well as large volumetric efficiency, multi-objective optimization

4

algorithm, NSGA-II, has been also applied. In the Ph.D. Thesis of K. Kontogiannis the parameterization and handling of waverider forebody geometries is first considered; a new three-dimensional leading edge waverider design method is proposed, being a step away from inverse methods and a step towards direct waverider design [12]. In the work of Son et al. [13] an optimization framework for the inverse design of hypersonic waveriders is presented.

Since its inception, the waverider has been an object of study. Once a conceptual design is devised, the next step is its analysis. Aerodynamic analyses of flight vehicle configurations are obtained through various means. The typical methods are the use of engineering correlations, flight tests, wind tunnel testing and numerical simulations. These methods are not only used for analyses but also for proof of concept and building of knowledge. In the subsonic regime, each method has shown to be effective in conclusively determining performance and gaining scientific perspective. However, in hypersonic speeds, each method has shown to have some issues in its reliability and/or implementation. Still research continues to improve upon these methods to gain knowledge for mastering the hypersonic regime.

During the early quest for hypersonic flight, NASA designed, constructed and tested a hypersonic vehicle. The vehicle, illustrated in Figure 2, demonstrated that it was capable of achieving speeds up to Mach 8. However, a closer look at wind tunnel data revealed an interesting phenomenon. It was observed that the vehicle's aerodynamic performance parameter L/D decreased as Mach number increased.
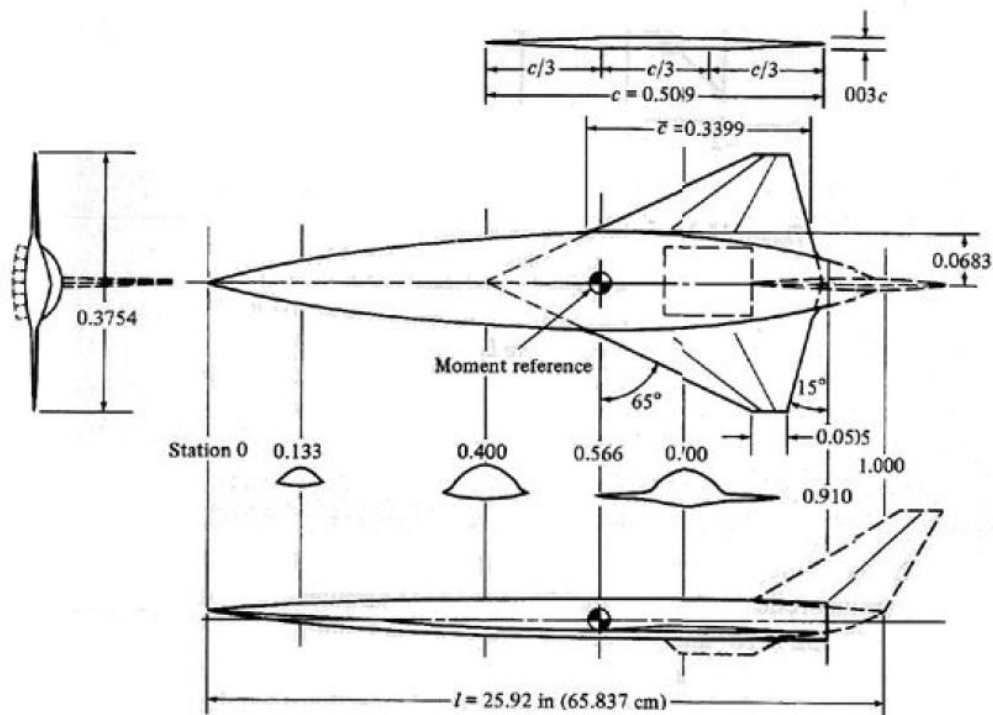

Figure 2: NASA first hypersonic vehicle [14].

Consequently, Kuchemann [15] conducted an extended number of empirical studies of supersonic/hypersonic research and vehicle performance of that time over a range of Mach numbers and documented the trend that the maximum L/D observed decreased as Mach number increased, establishing the so-called "*L/D barrier*". This detail highlights another challenge in the realization of hypersonic flight vehicles; the traditional aerodynamic designs and design methodology were not effective in the hypersonic regime. Bowcutt [16] showed a method to optimize waverider configurations using a multidisciplinary approach, yielding geometric configurations with relatively higher L/D ratios at higher Mach numbers. Bowcutt's findings were later supported by other researchers [17, 18]. Figure 3 illustrates the comparison of findings of Kuchemann, Bowcutt and Corda; the non-filled circles represent experimental data, obtained from flight tests and experiments. Kuchemann established the solid line and Bowcutt established the dashed line. The work of Bowcutt renewed interest in the waverider design technique that was first introduced in the 1950's by Nonweiler [19] in his attempt to design a hypersonic wing for re-entry purposes. Figure 4a, established by Kuchemann, represents vehicle configurations that will likely achieve maximum L/D in their respective flight regime. The trend shows that a highly integrated vehicle configuration, with aerodynamic and propulsion features fused together, would fare as the optimum aerodynamic configuration for the hypersonic regime. The waverider design methodology inherently yields geometries that support this type of configuration. Figure 4b describes the four distinct classes of hypersonic aircraft with the major hypersonic aerodynamic effects they experience.
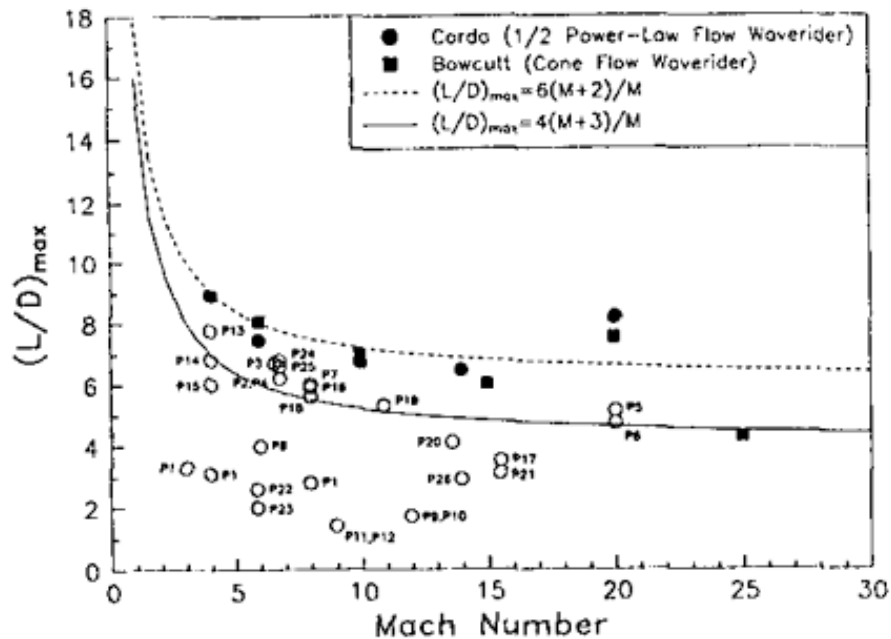

Figure 3: L/D barriers [20].

At the time of its creation, the waverider design concept solved a major re-entry problem by yielding configurations with the L/D needed for long-range glided re-entry landings. However, the leading edge of a waverider is inherently sharp, which yields an extreme aerothermodynamic load at the corresponding region. Also, early configurations[14] of the 1950's and 1960's were thin and presented limited 'volumetric efficiencies, while their performance analysis did not consider viscous effects. Advanced numerical methods and computational resources were not available in the 1950s, so as to

produce a wider range of configurations or perform viscous analyses, due to required high computational load. Such circumstances rendered waveriders unrealistic at the time. However, the work of Bowcutt during the 1980s optimized waveriders by implementing established engineering relations and computational resources to predict the viscous effects on their performance. With the renewed interest, many more research efforts of the waverider followed. However, even with the excitement of the waverider's potential, its design methodology has yet to extend to a practical design of a working and producible hypersonic vehicle.
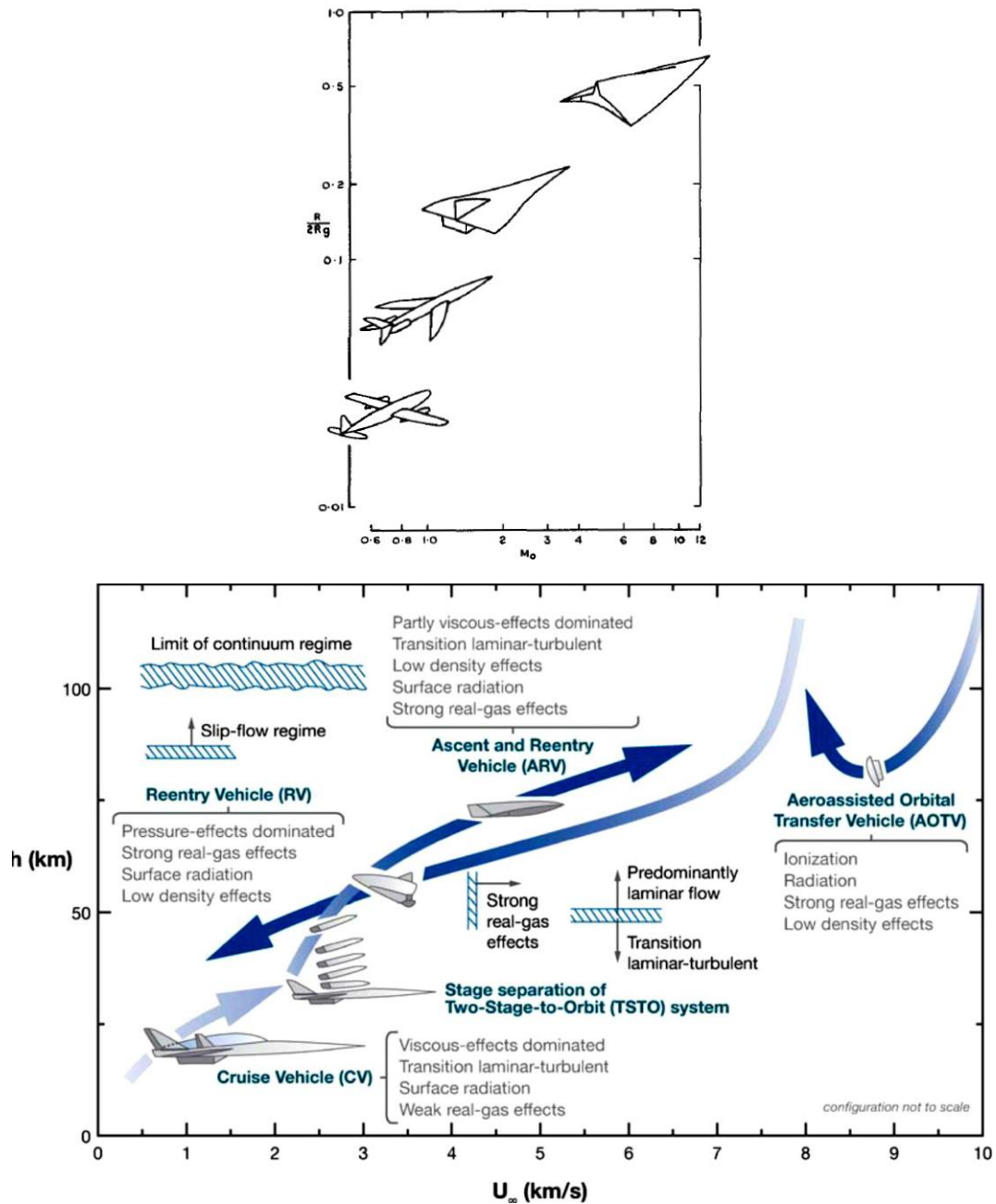

Figure 4: (a - top) Aircraft flight spectrum; (b - bottom) four distinct classes of hypersonic aircraft with their major hypersonic aerodynamic effects [21, 22].
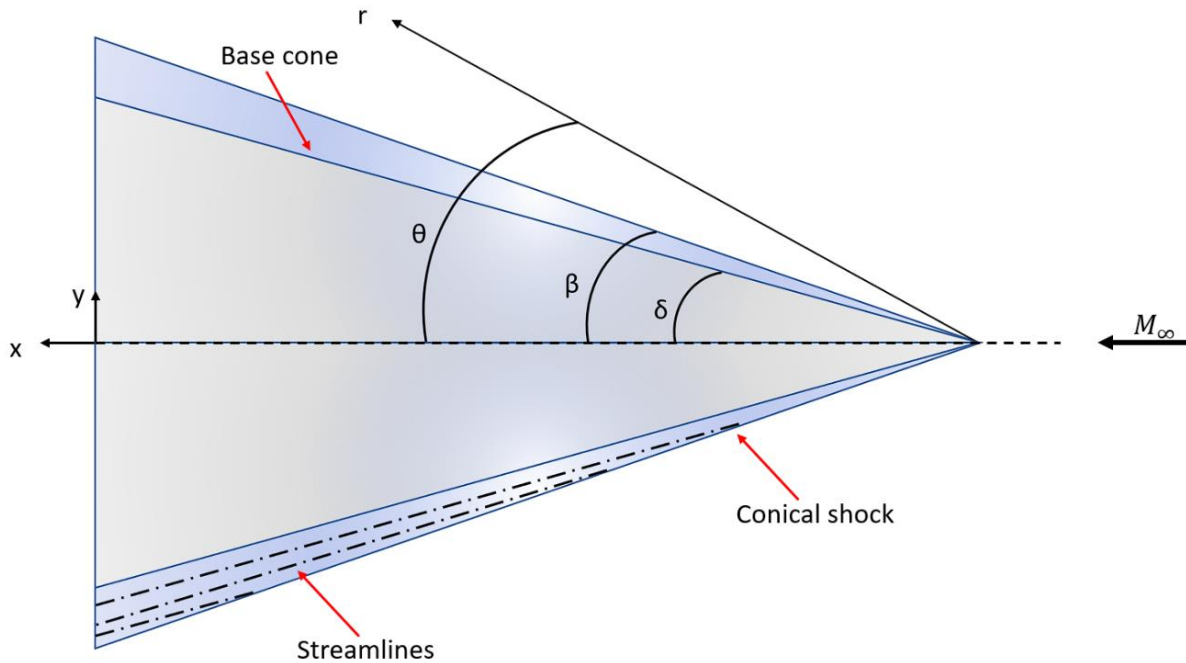
2. Waverider Design Methodology

Waveriders are designed as products of a hypersonic flow environment through an inverse design methodology. The inverse design approach uses the streamlines of a post shock inviscid flow field as the design space for the *compression stream surface* (usually the lower surface) of waverider geometries. The waverider methodology ideally produces a streamlined geometry for the hypersonic flow regime. The lower surface formed by a set of neighboring streamlines yields the attachment of the leading edge to the shock. A design algorithm for a waverider geometry generation is presented below.

- Selection and design of the basic flow field in the flow direction.
- Solving the basic flow field, using Taylor-Maccoll equation, or Euler or Navier-Stokes equations.
- Tracing the streamlines.
- Application of the osculating cone theory in the spanwise direction.
- Remodel the final model.

More specifically, in order to define the initial flow field (from which the waverider will be derived), a cone is designed with a pre-specified angle δ. Then the inlet boundary conditions are defined, such as Mach number, pressure, and temperature, and the flow field is calculated using a computational fluid dynamics method. After obtaining the flow field, the streamlines can be traced by numerically evaluating Equation 1, by marching from points located on the shock to obtain streamline points [23, 24].

$$\frac{dr}{V_r} = \frac{r\,d\theta}{V_\theta} \tag{1}$$

A schematic representation of the traced streamlines from the conical shock is shown in Figure 5. In order to specify a waverider geometry using the cone waverider derived method, a base curve must be specified. The base curve is then projected into the shock parallel to the freestream so as to obtain the leading-edge. After that, streamlines are traced from the leading-edge locations on the shock back to the base plane to generate the compression (lower) surface of the waverider. Apart from the analytical Equation 1, another more simplified technique can be also used to trace the streamlines as well. Streamlines can be traced tangential to the base cone surface to easily obtain the compression surface geometry. The base curve equation used for the waverider design is shown around the symmetry plane in Figure 6. Denoted as l is the total width of the waverider, while l_u is the flat part of the curve. The curved part of the curve can be calculated by the equation shown in Figure 6. The value of b can be calculated given the l_u, l and h, which can be specified after the solution of the initial conical flow field.

Figure 5: *Schematic representation of the waverider design methodology.*
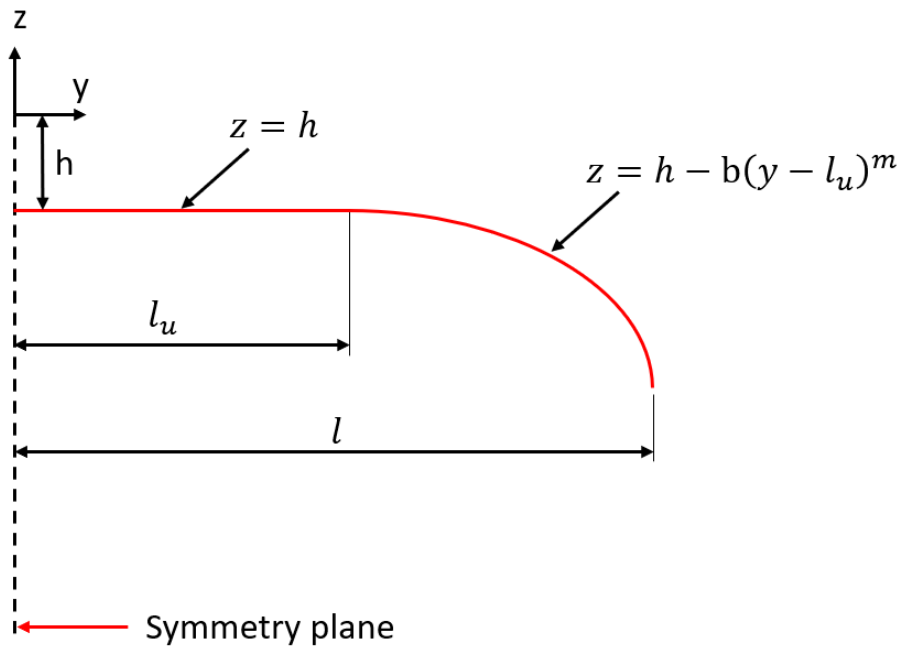
Figure 6: *Base curve equation.*

In order to produce a practical waverider design, the inherently sharp leading edge must be handled. Therefore, a practical design approach must incorporate blunting techniques to handle this task. Blunting the leading edge, as well as areas where two stream surfaces meet, relieves heating effects and yields a more realistic shape for manufacturing processes. On the other hand, blunting inherently

deviates from a true waverider design and allows some leakage of pressure from the lower surface to upper surface. Hence, drag is increased and aerodynamic performance of the waverider is decreased. It has been shown through studies [25, 26] that blunting decreases the heat flux experienced by a vehicle while negatively affecting its L/D. Even with this effect, a blunted waverider design will still potentially provide exceptional aerodynamic performance compared to other alternative designs. The seepage of pressure can be controlled and potentially minimized through the design of the leading edge. The amount and type of blunting must be determined via a compromise between minimizing heating and maximizing aerodynamic performance. As there is a variety of configurations for a waverider, there is a variety of designs for a blunt leading edge.

There are two main approaches to blunting a leading edge, as shown in Figure 7. One approach removes material and the other adds material. Tincher and Burnett [27] suggested the addition of material will have less of an aerodynamic cost.
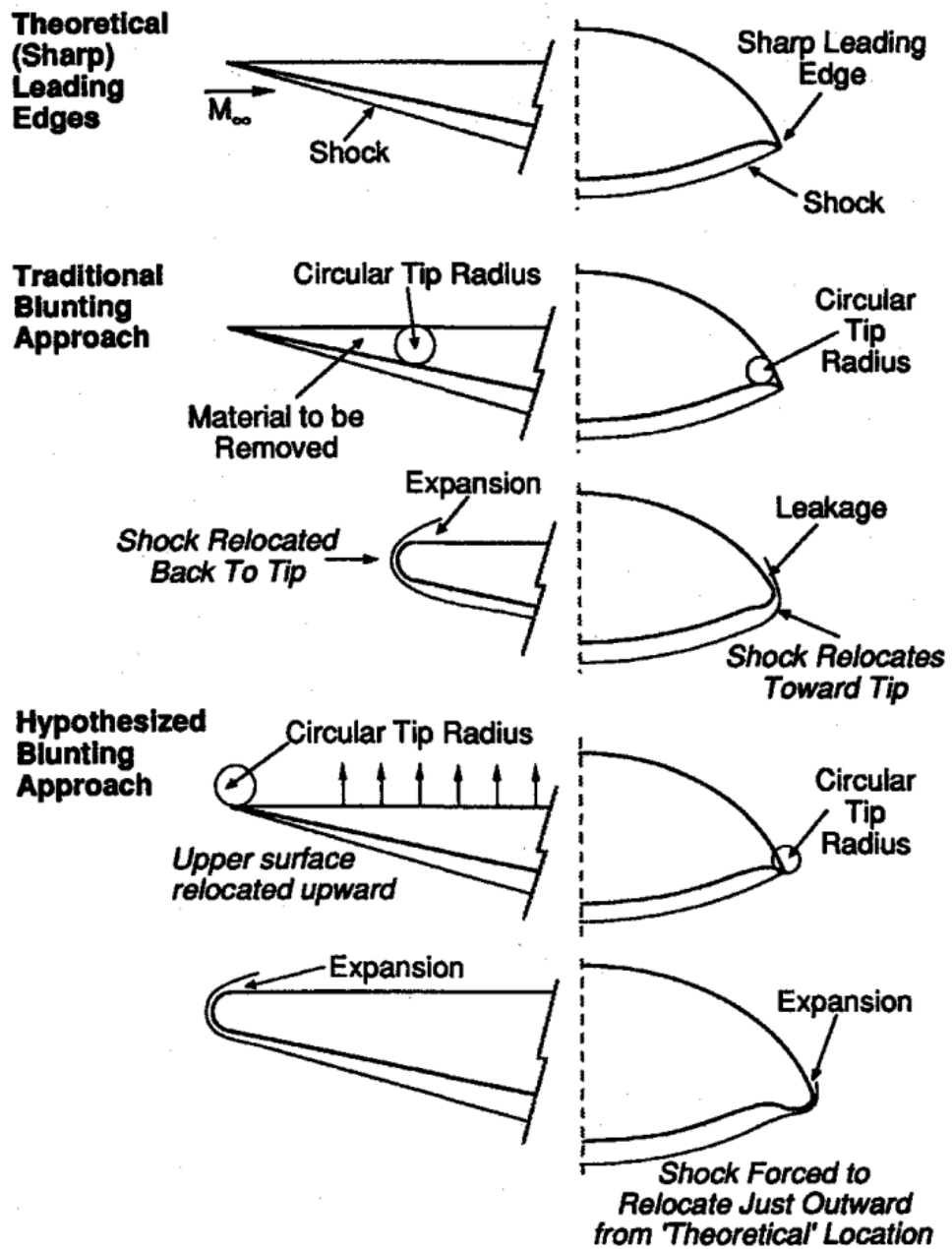
Figure 7: *The two main leading-edge curving techniques [27].*

3. Application to a Specific Waverider Design

In accordance to the aforementioned procedure, a waverider for a speed of Mach 7 was designed. To generate the initial flow field, a 7-degree *2 m* in length cone with a *1 cm* blunt leading-edge was designed at first (Figure 8). Then, the three-dimensional flow field around the cone was solved, using the Direct Simulation Monte Carlo (DSMC) method. The utilized flow conditions simulate the flow at *90 km* altitude and were taken from the US standard atmosphere model. The corresponding flow conditions, along with the DSMC simulation parameters, can be found in Tables 1 and 2 respectively.
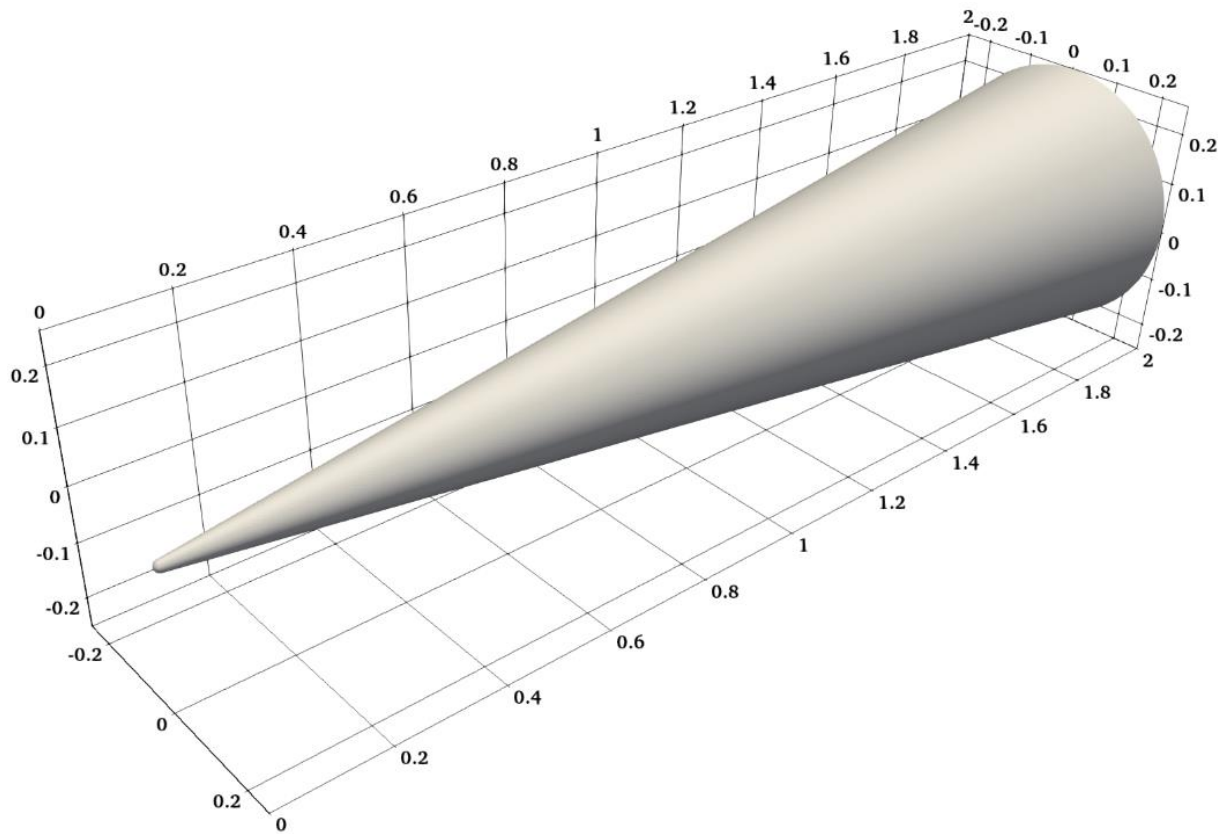
Figure 8: The geometry of the 7-degree half cone, used for the calculation of the initial flow field.

All calculations presented in this section were done using the open-source parallel DSMC code SPARTA (Stochastic Parallel Rarefied-gas Time-accurate Analyzer), developed in Sandia National Laboratories [28]. After the three-dimensional flow field around the 7-degree cone was calculated, the flow streamlines (at specific parallel planes) around the cone were extracted in order to identify the shockwave boundaries. An overview of the calculated flow field streamlines can be seen in Figure 9. The shock boundaries in the side and top plane can be identified by the bending of the flow streamlines, whereas in the rear plane at the back of the cone the shock boundary is identified by the color change in the streamwise velocity flow field.

Table 1: *Flow parameters for a Mach 7 flow at 90 km altitude.*

Mach number, Ma_∞	*7*
Reynolds, Re_∞ (1/m)	*2873*
Freestream velocity, U_∞ (m/s)	*1965*
Knudsen number, (Kn)	*0.6*
Angle of attack, α (degrees)	*0*
Freestream density, ρ_∞ (kg/m³)	*9.62×10^{-6}*
Freestream pressure, p_∞ (Pa)	*0.55*
Freestream temperature, T_∞ (K)	*196*
Wall temperature, T_w (K)	*300*
Gas	*Air*

Table 2: *DSMC computational parameters for Mach 7 flow at 90 km altitude.*

Number density, Nd_∞ (#/m³)	*2.00×10^{20}*
Timestep (s)	*3.0×10^{-7}*
Transient period	*40,000*
Sample period	*100,000*
Number of particles (#)	*10.5×10^{9}*
Number of cells	*183,664,000*
Wall-clock time (CPU hours)	*195,840*
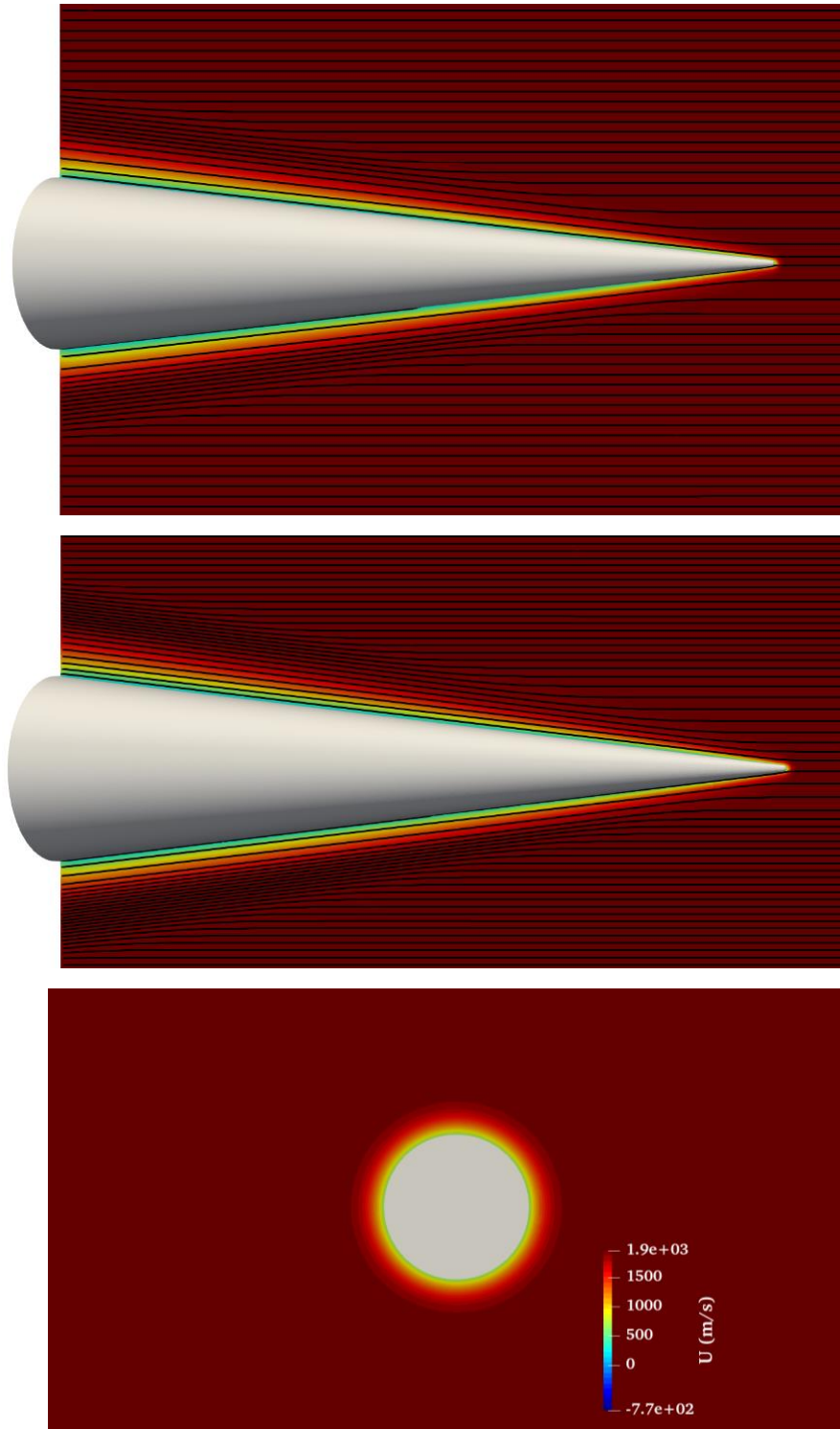
Figure 9: *Streamlines of the three-dimensional flow field around the 7-degree cone.*
*Side view (top), top view (middle), rear view (bottom).*

After extracting the aforementioned flow planes then these planes are imported to a CAD (Computer Aided Design) software in order to design the exact geometry of the waverider. We start from the

back of the geometry by producing curves that are tangent to the circular shock shape. The first characteristic section can be seen in Figure 10. In order for the design to be realistic, the leading edges must be blunt and not sharp. To control the bluntness of the leading edges, a four-point Bezier curve was used to generate the leading-edge shape. In the same manner a different section of the waverider is designed along the longitudinal axis of the vehicle, every 30 cm. The upper and lower surfaces of the waverider are limited by the produced shockwave of the prescribed 7-degree cone geometry.
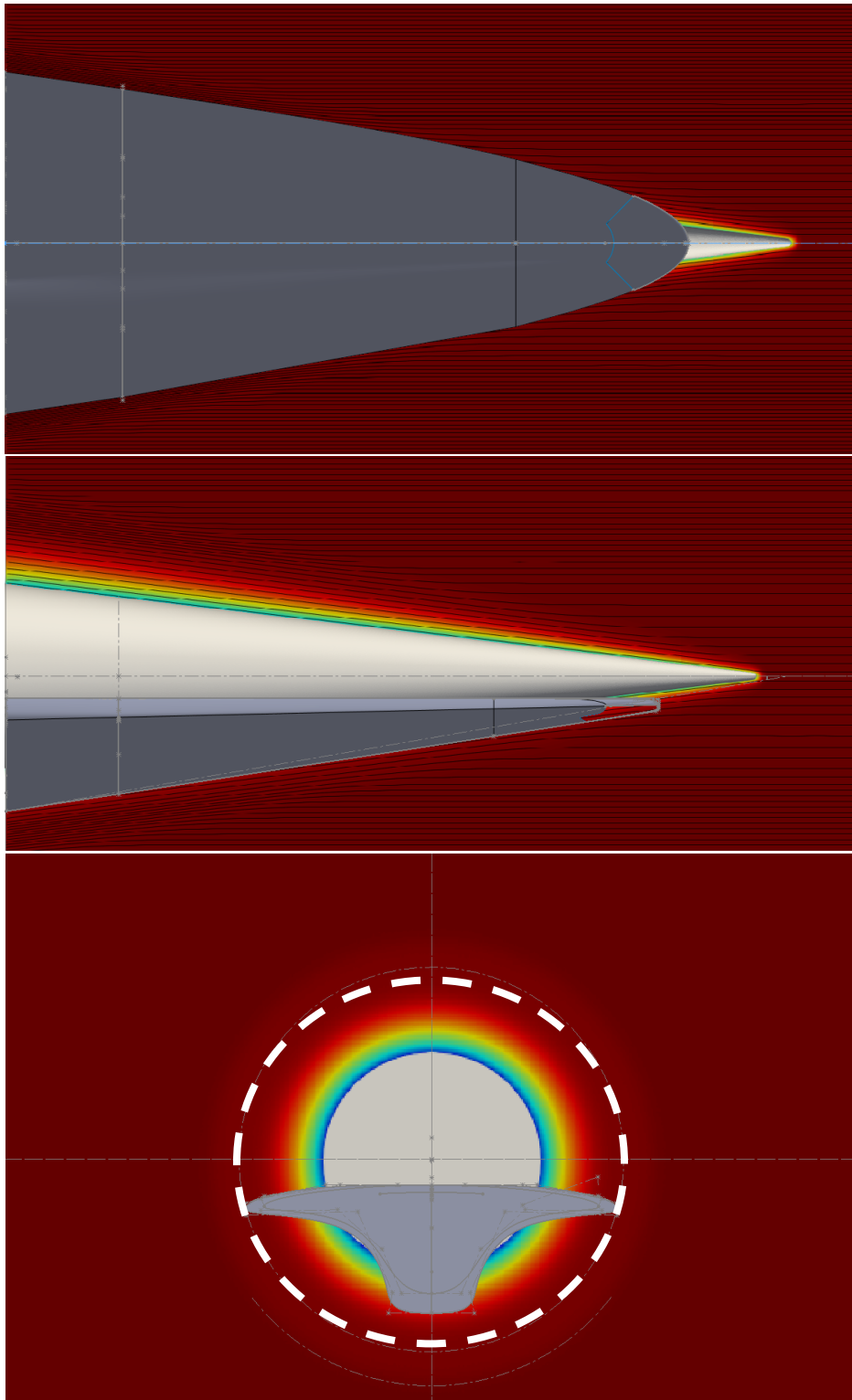
Figure 10: *Waverider surfaces along the flow streamlines. Top view (top), side view (middle), rear view (bottom).*

Figure 11 shows an overview of these geometry sections. For clarity, not all the produced sections are demonstrated. Finally, when all sections are produced, a loft operation with tangency constraints was used to generate the waverider surfaces. To reduce the design complexity and to take advantage of the symmetry of the flow field, only half of the final geometry is designed and then mirrored around the symmetry plane.
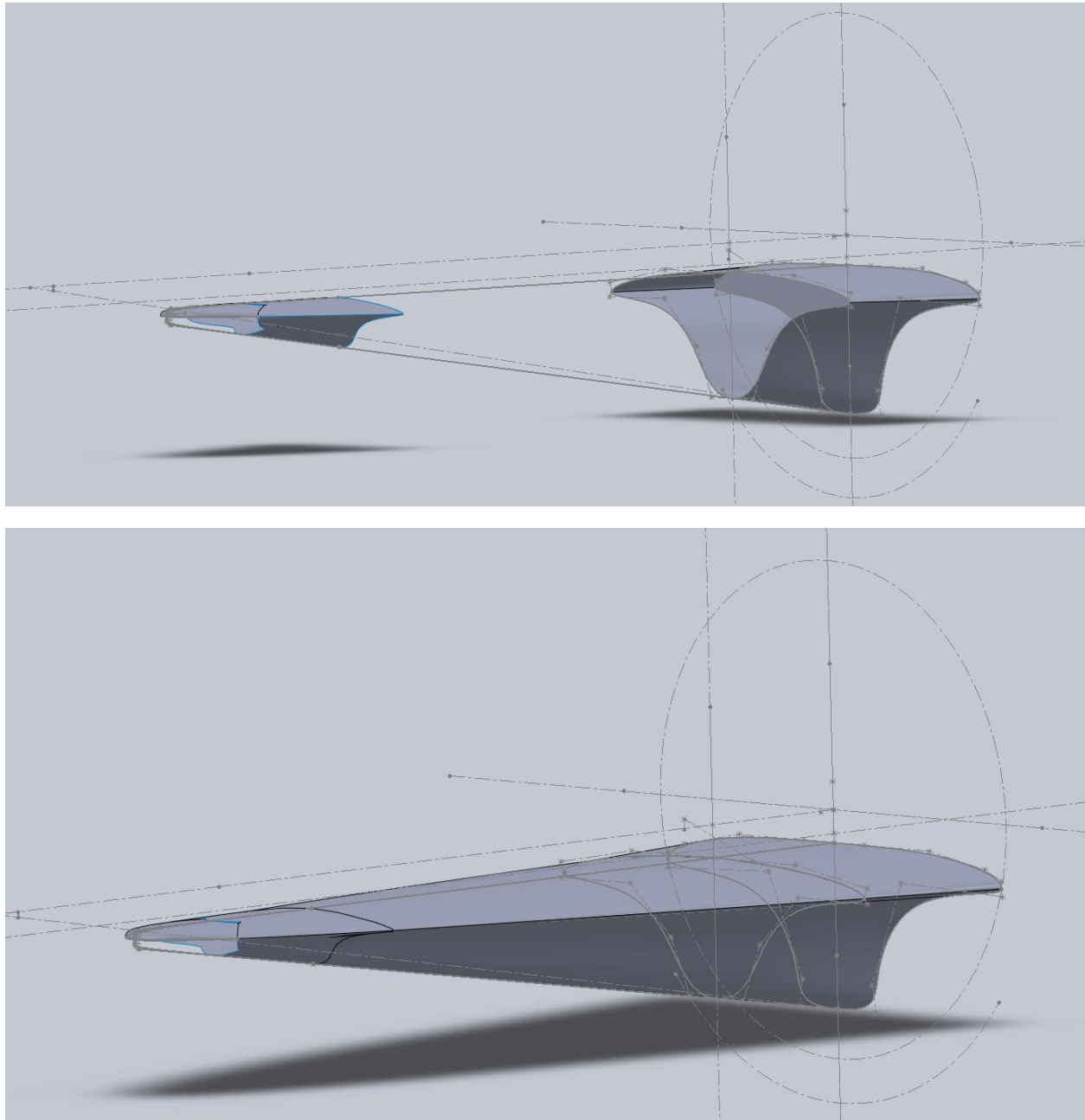
Figure 11: Surface lofts along the vehicle profiles (top). Vehicle overview without the nose section (bottom).

The osculating cones methodology described previously presents a robust, computational framework for designing hypersonic waveriders. Given the intricate challenges of hypersonic aerodynamics, such as extreme temperatures, high pressures, and complex shock-wave interactions,

the design process is inherently complex. Here, we break down this methodology into discrete steps, focusing on both the theoretical and practical elements that guide the design of these revolutionary vehicles.

Step 1: Initiating from the Aft End of the Cone

The journey of waverider design begins at the trailing end of a cone, specifically used to generate a predefined flow field. At this point, the critical task is to delineate the shock wave boundaries, which are clearly marked by dashed white lines in Figure 10 (bottom). This initial step is pivotal, as it lays the foundation for the entire design by establishing the first profile of the waverider. Both the leading edge and the lower surface of this profile are sculpted to be tangential to the shock wave boundaries. The tangential approach minimizes drag and optimizes aerodynamic performance, key parameters for any hypersonic vehicle.

## Step 2: Sequential Cross-sectional Profiling

The design then progresses by taking cross-sectional planes at approximately 30 to 40-centimeter intervals along the length of the cone. Each of these planes serves as a canvas for developing a unique profile that accurately corresponds to the flow field conditions at that location. It is like creating slices of the vehicle's body, each designed to work most efficiently with its specific flow conditions.

Step 3: Lofting Operation

After generating these individual profiles, the next step is to connect them. This is accomplished through a lofting operation, which essentially stitches the profiles together, forming the waverider's outer skin. This procedure relies on interpolation techniques to ensure a smooth transition between profiles (Figure 11). However, as we proceed towards the cone's apex, these profiles start becoming significantly slender, and this is where the lofting operation reaches its limitations.

Step 4: Addressing the Nose Region

In the nose region, conventional lofting operations often fail, due to the progressively diminishing cross-sectional area of the profiles. To mitigate this, boundary surfaces are strategically employed. As illustrated in Figure 12, these boundary surfaces are sculpted to match the curvature of the original cone. They serve as the outer skin for the nose section, integrating seamlessly with the previously lofted surface.
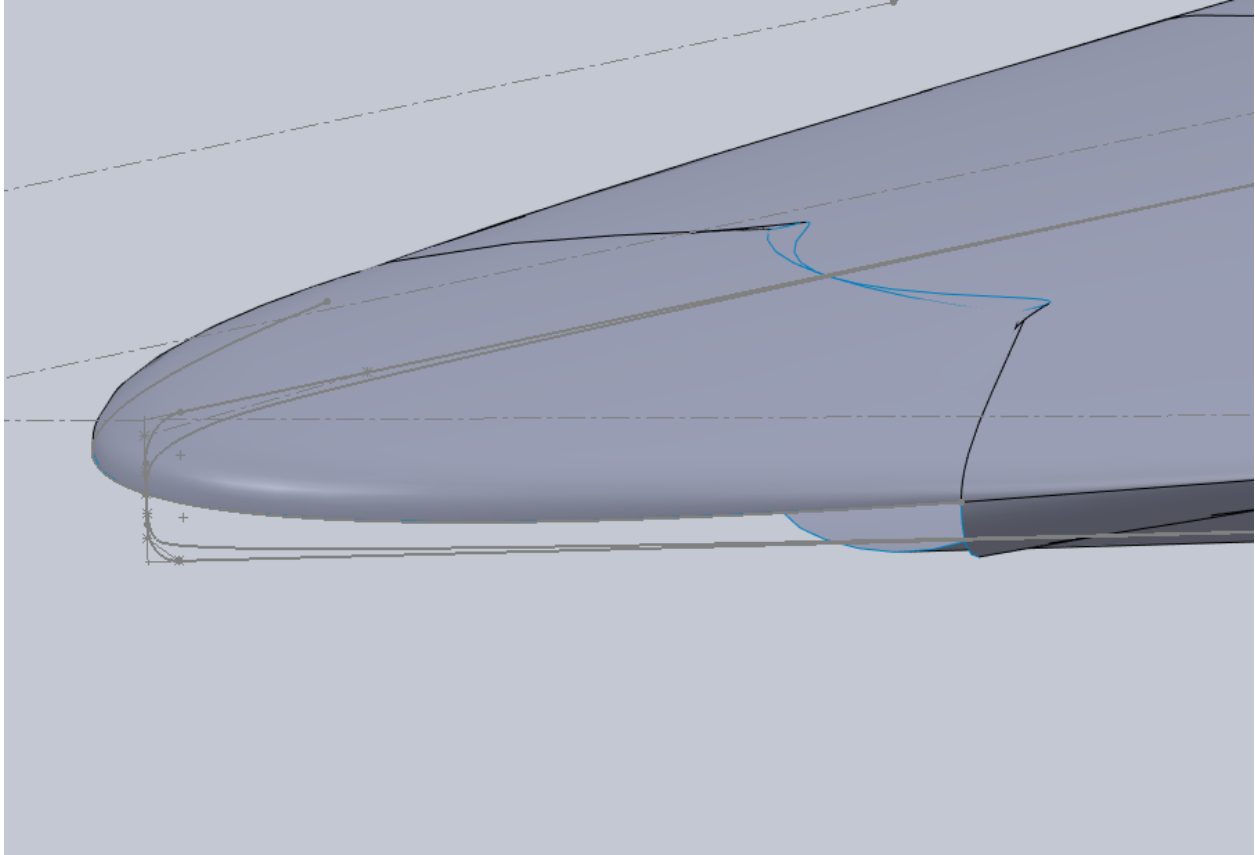
Figure 12: *Nose section with upper boundary surface.*

## Step 5: Knitting Surfaces for Fluid Simulation

Once the nose section and the lofted body are fully designed, a knitting operation binds all these disparate surfaces into a cohesive, watertight body (Figures 13 and 14). This step is imperative for the subsequent fluid dynamics simulations, as any gaps or inconsistencies would introduce errors or instabilities in the computational model. The completion of this knitting operation results in a unified vehicle geometry, as showcased in Figure 15.

Step 6: Mirroring Operation

For computational efficiency and simplified construction, only one half of the vehicle is initially modeled. The remaining half is generated through a mirroring process, aligned along a symmetry plane. This reduces both the computational load and the design complexity, enabling more rapid iterations during the development phase.
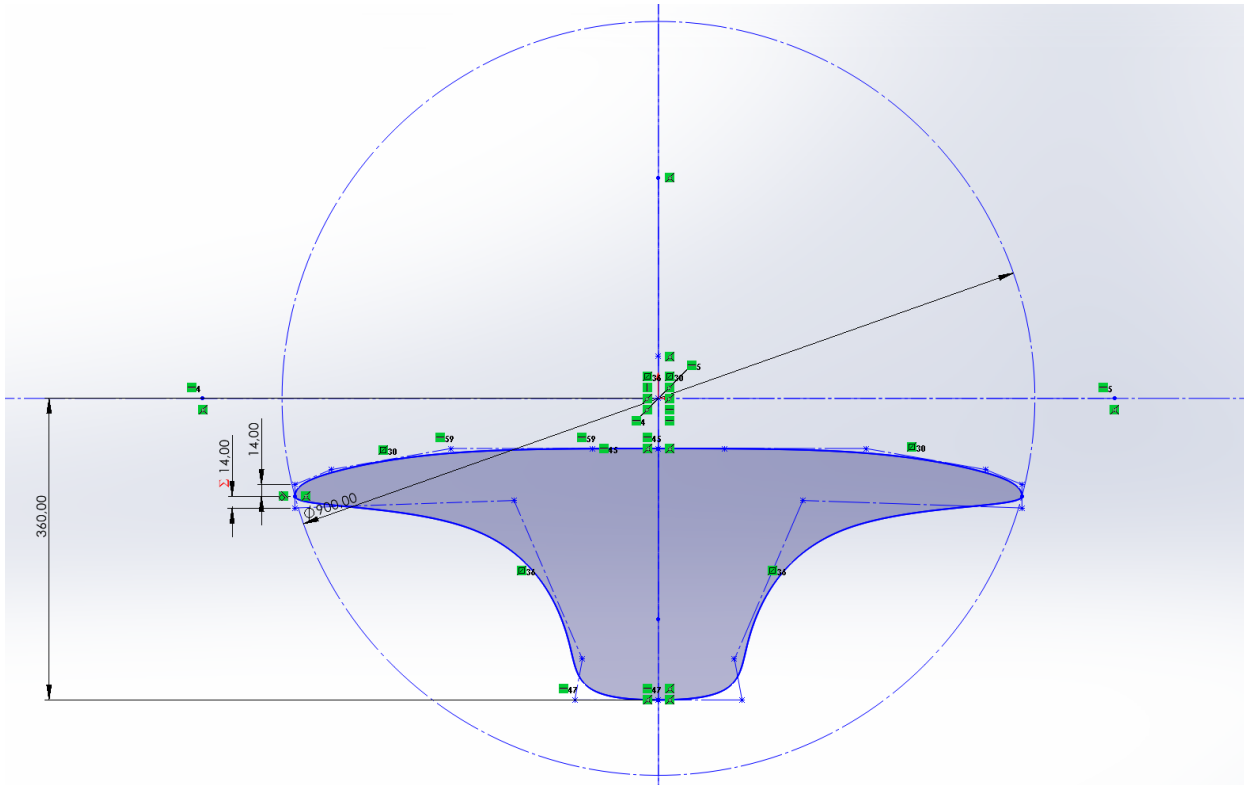
Figure 13: *Back section of the waverider (units in mm).*
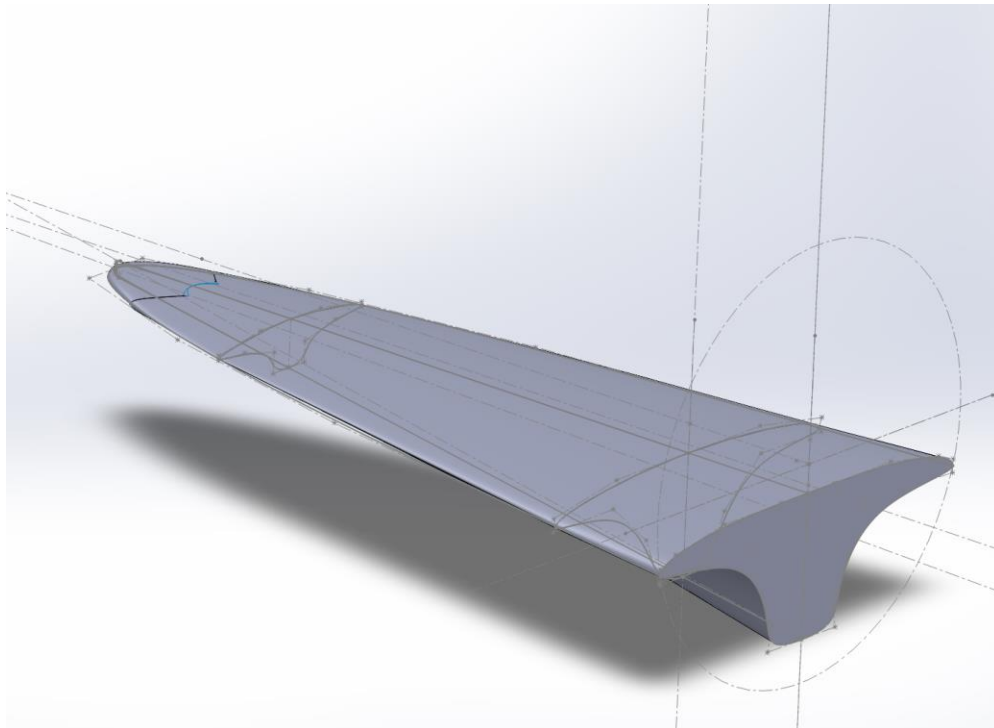
Figure 14: *Waverider sections and the complete geometry.*
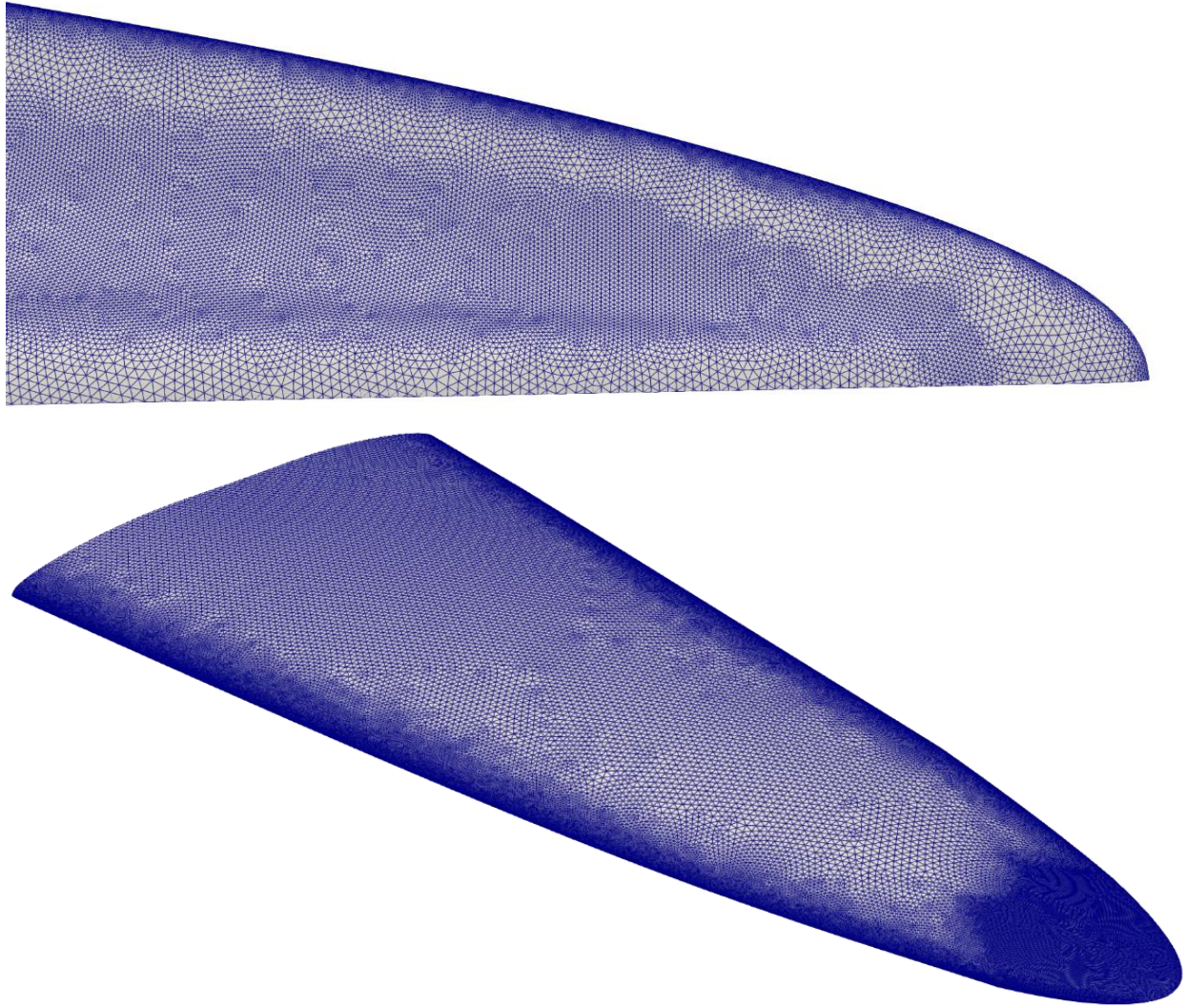
Figure 15: The utilized surface mesh. Lower surface (top), isometric view (bottom).

Step 7: Refined Leading-Edge Design

A standout feature of this methodology is the intricate attention given to the design of the waverider's leading edges. Unlike conventional hypersonic vehicles, which typically employ sharp leading edges, this method adopts a nuanced approach. Sharp leading edges are known to induce high stress concentrations and are less thermally robust, often failing under the extreme conditions of hypersonic flight. To counteract this, three-point Bezier curves are used to blunt the leading edges. These curves provide the dual advantage of enabling curvature and tangency control, thus yielding a geometrically realistic and thermodynamically resilient design.

The osculating cones methodology, steeped in aerodynamics, computational fluid dynamics, and applied mathematics, offers a comprehensive and nuanced pathway for designing hypersonic waveriders. By integrating these multi-disciplinary domains, this approach addresses the intricate

complexities of hypersonic flow and structure, yielding a waverider design that is not only aerodynamically efficient but also thermally and structurally robust.

The first phase in the computational exploration of the waverider's aerodynamics entails creating a precise computational mesh. This mesh is instrumental in accurately capturing the intricate geometric features of the waverider, particularly around high-sensitivity areas like the leading edges. A meticulous approach has been adopted to model the leading edges as faithfully as possible to the original design. This is vital because even minor deviations can have significant aerodynamic consequences. The computational surface mesh employed in the Direct Simulation Monte Carlo (DSMC) method is illustrated in Figure 15.

Given the intense computational demands of hypersonic flow simulations, strategic methods are employed to optimize resource usage. One such strategy is to simulate only one-half of the waverider's geometry. The computed flow field is then mirrored along a pre-defined plane of symmetry, effectively reducing computational resources without compromising accuracy. One of the paramount goals of this simulation is to verify the attachment of the shock wave to the vehicle's leading edges. This is critically assessed through the visualization of pressure contours and Q-criterion plots, as shown in Figures 16 and Figure 17, respectively. More specifically, the Q-criterion is calculated using equation (2), where Ω is the antisymmetric part of the velocity gradient, known as the vorticity tensor, and S is the symmetric part, known as the rate of strain.

$$Q = \frac{1}{2}(\|\Omega\|^2 - \|S\|^2) \tag{2}$$

According to the definition, positive values of Q-criterion indicate areas in the flowfield where the vorticity dominates the flow, while negative values are indicative of strain rate or viscous stress dominated areas [29, 30]. The Q-criterion serves as an essential diagnostic metric for the flow field around the waverider. In Figure 18, below the leading edge a negative value of Q-criterion is observed, which is evident of a shock existing in that area. The pressure contour plots (Figure 16) show a noticeable pressure buildup around the leading edges of the waverider, strongly suggesting that the shock wave is well-attached to the vehicle's geometry.
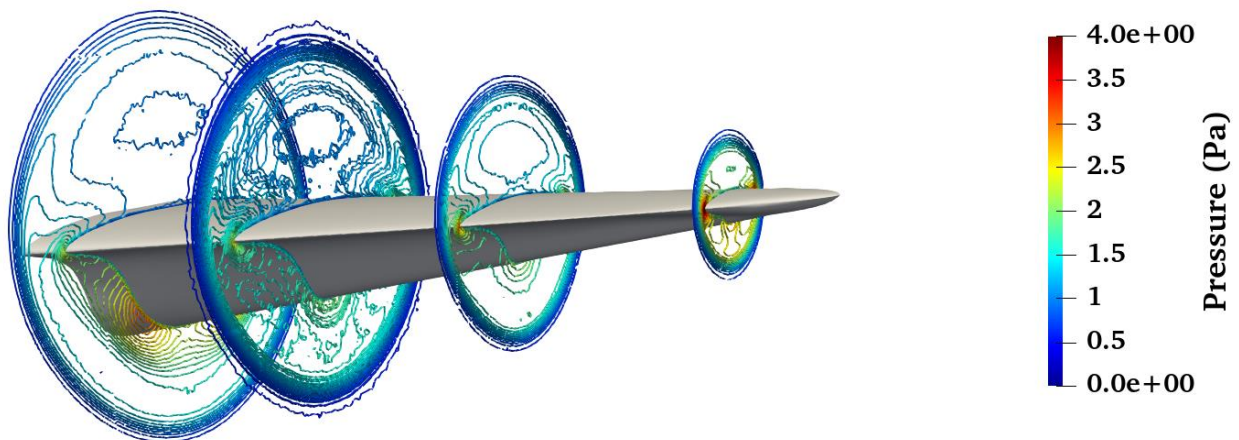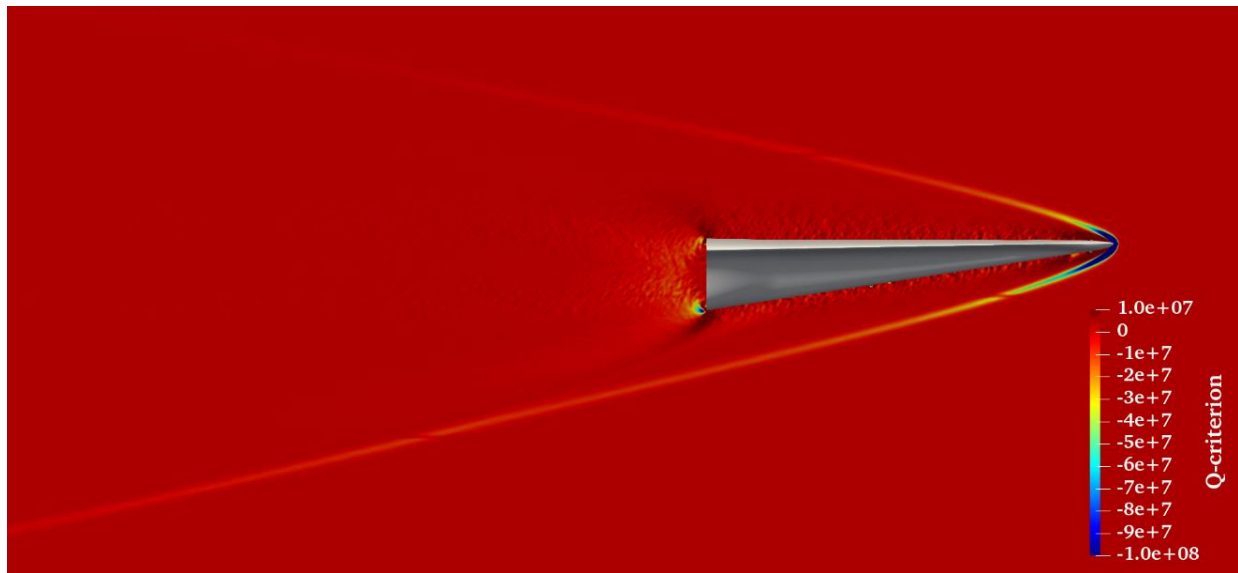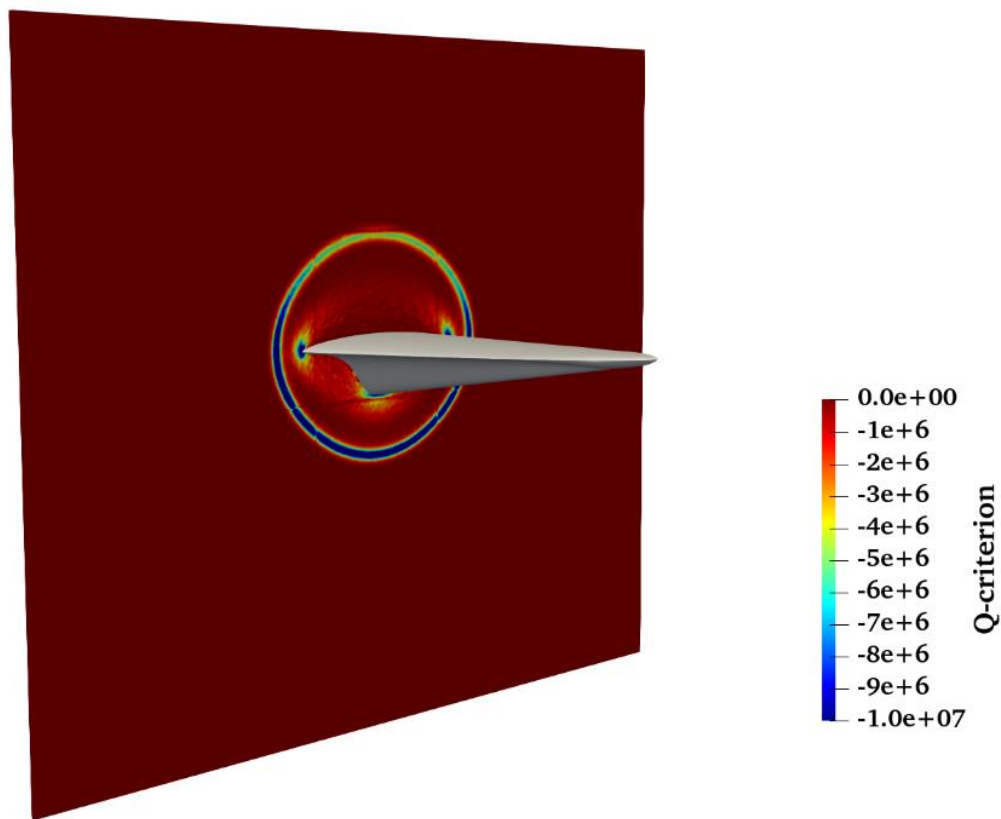

Figure 16: Pressure contours around the vehicle.

22
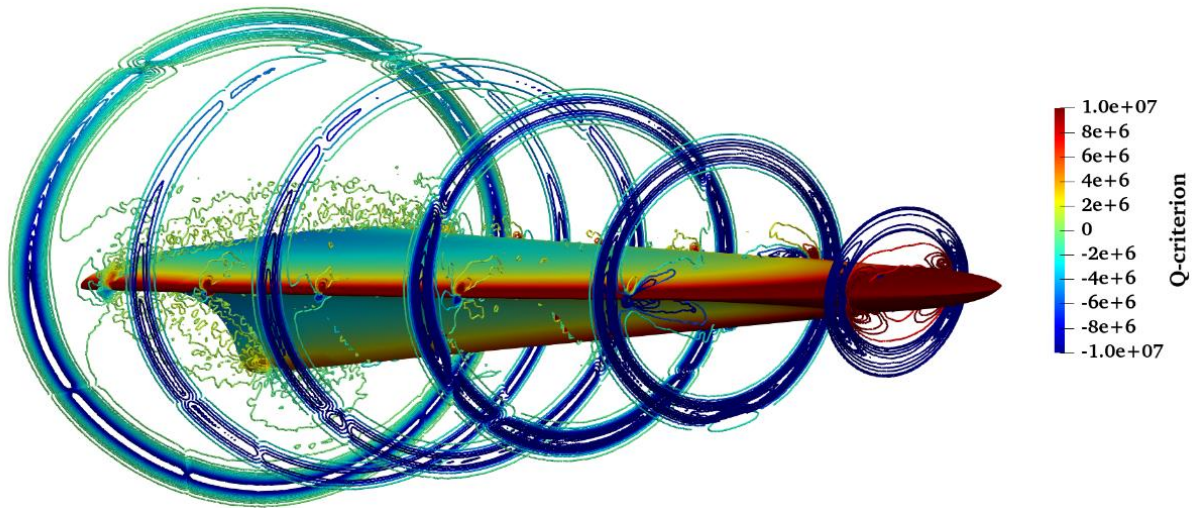
Figure 17: *Q-criterion contours around the vehicle.*

Furthermore, Figure 17 visually represents the pressure distribution on the waverider's surface. As expected, elevated pressure levels are observed around the leading edges and the nose section, substantiating the presence of an attached shock wave. The amalgamation of these various computational diagnostics—ranging from mesh optimization to pressure and Q-criterion analyses provides a comprehensive evaluation of the waverider's aerodynamic performance. These findings serve as a testament to the computational integrity and physical feasibility of the waverider design, particularly in the context of shock wave attachment to the leading edges. Figure 19 presents the Q-criterion contours on a vertical plane at the back face of the vehicle. The concentrated blue regions at the wing tips and under the fuselage are attached shocks.
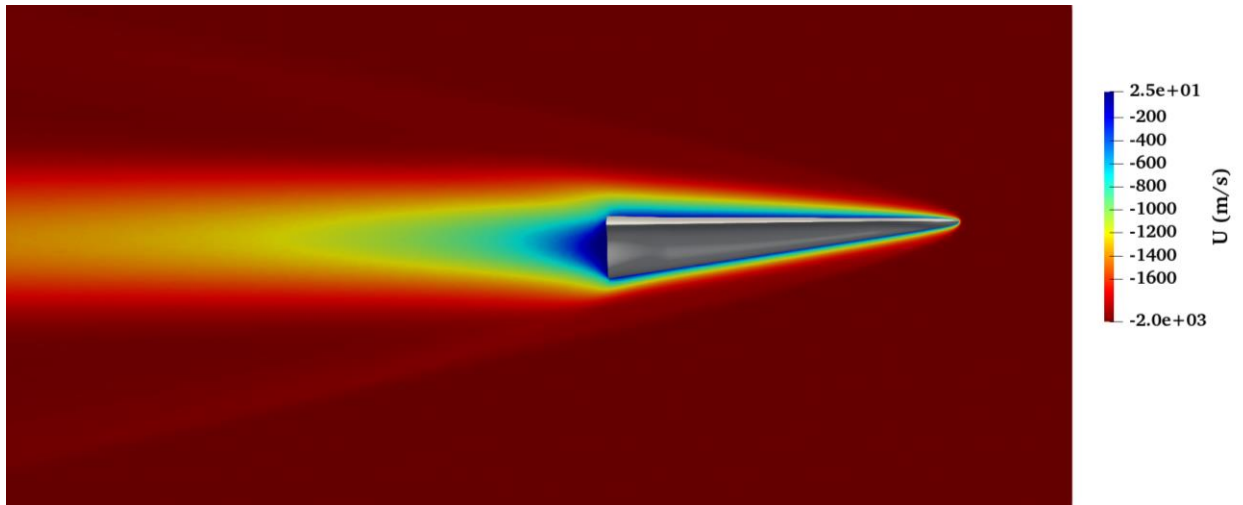
***Figure 18:*** *Q-criterion contours on the plane of symmetry.*

Figure 19: *Q-criterion contours on a vertical plane.*

Figures 20 and 21 present the streamwise velocity and the temperature field around the vehicle. For the flow conditions used in this work a maximum temperature of *1400 K* is identified in front of the nose.

Figure 20: *Streamwise velocity contours on the symmetry plane of the waverider.*
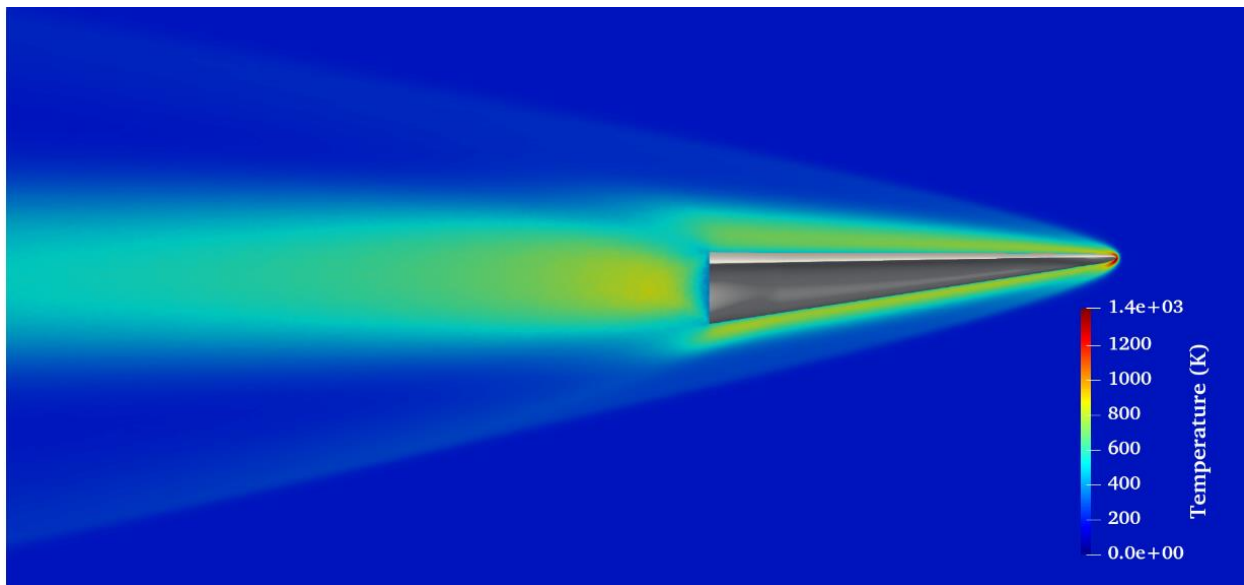
Figure 21: *Temperature field around the vehicle (on the symmetry plane of the waverider).*

In Figures 22 to 25 different flow properties are presented on a plane parallel to the waverider, while the surface of the vehicle is colored by surface pressure. Figure 22 contains the pressure contours on the aforementioned plane. Taking into account that the free-stream pressure is equal to *0.55 Pa,* a pressure rise of one order of magnitude around the nose is observed. The pressure around the leading edges is about four times higher than the free-stream pressure.
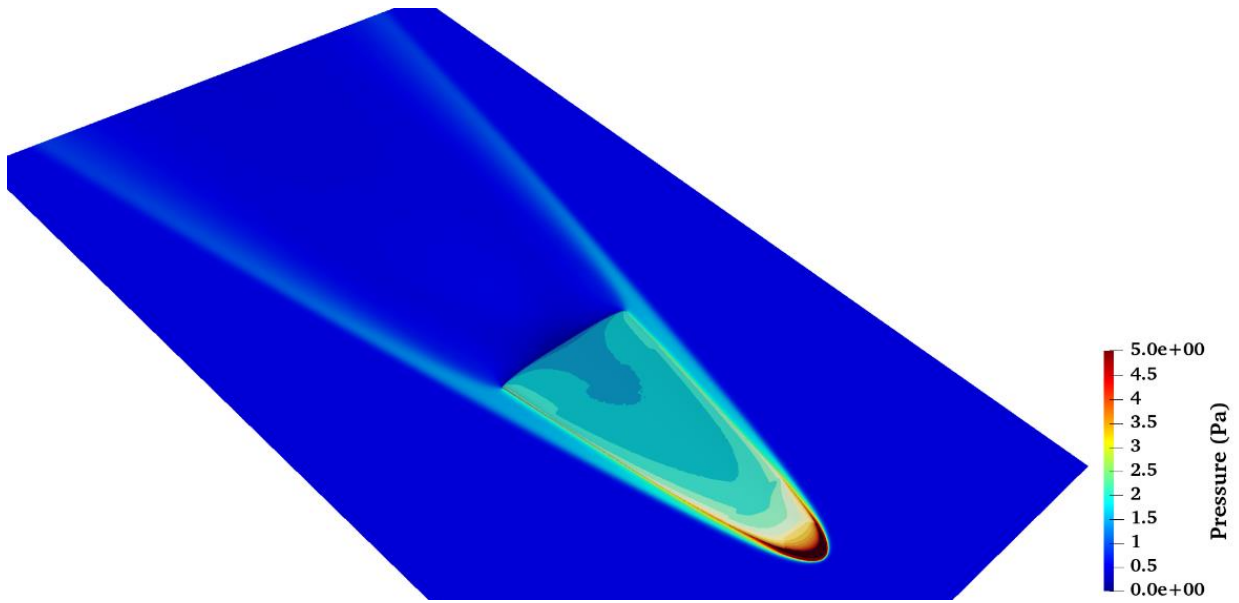
Figure 22: Pressure contours on a horizontal plane parallel to the vehicle.

Figure 23 contains the velocity contours on the same plane. In this Figure the attachment of the shock to the leading edge and the nose of the vehicle can be clearly observed. As it can be observed in Figure 24, the temperature around the leading edges is *800 K,* which is about four times higher than the free-stream temperature of *196 K*.
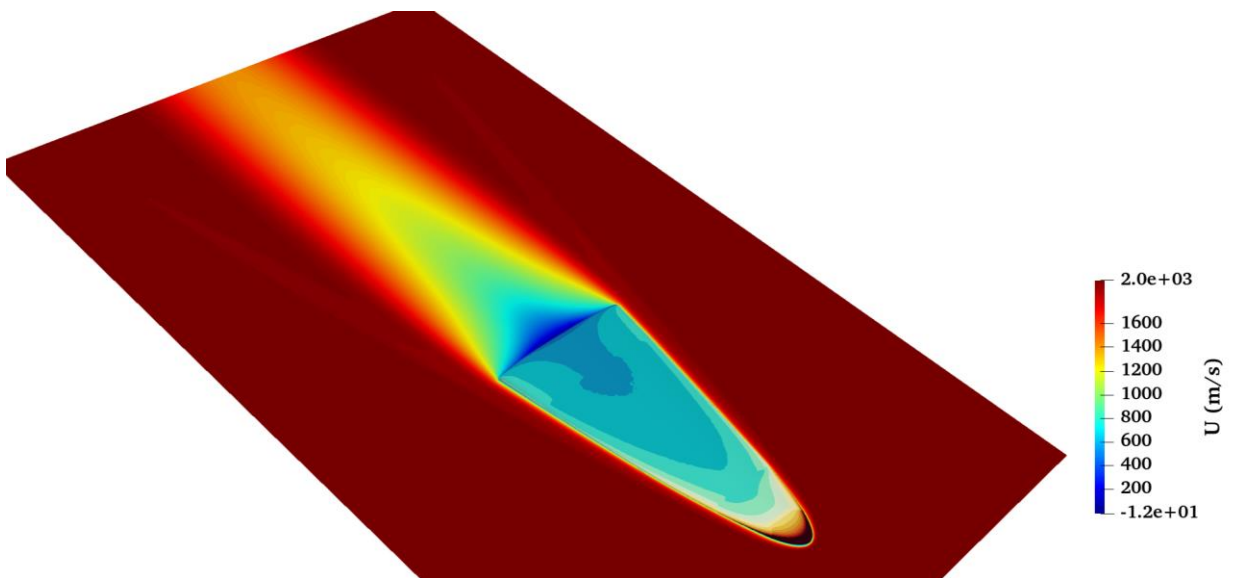
Figure 23: Streamwise velocity contours on a horizontal plane parallel to the vehicle.
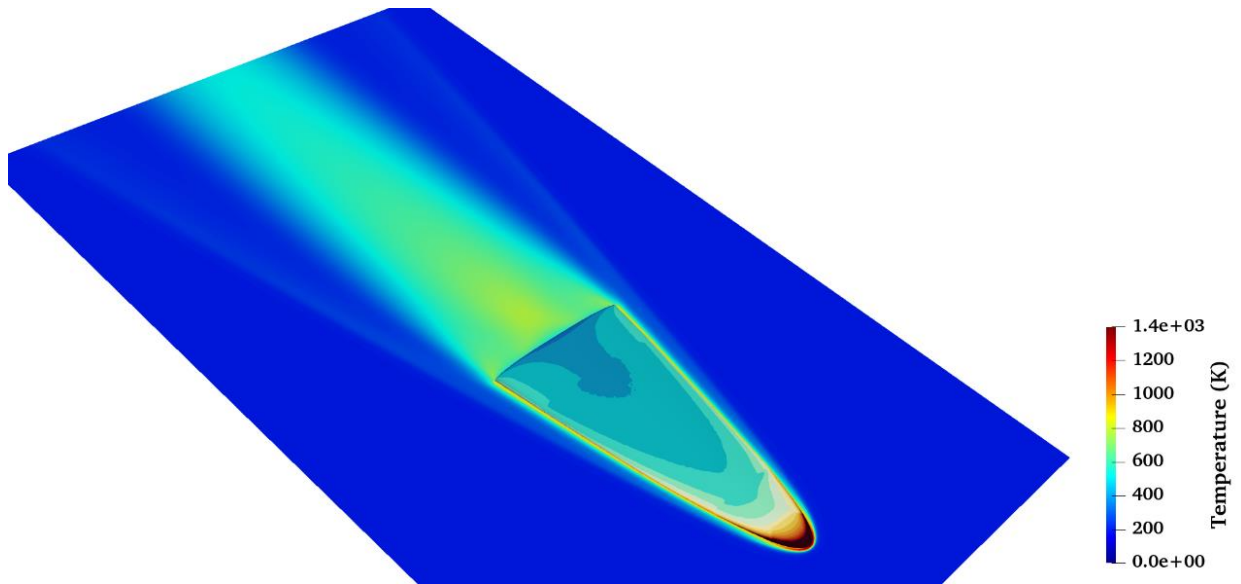
Figure 24: Temperature contours on a horizontal plane parallel to the vehicle.

Finally, the Q-criterion on the same plane is presented in Figure 25, which demonstrates the complete field of the attached shock. Furthermore, the positive values of Q-criterion revealed the formation of two vortices, one on the left and one on the right side, at the tip of the back section of the vehicle. A better view of these two vortices can be seen in Figure 26, where the vorticity is plotted at the back of the vehicle. The two vortices are rendered in red color.
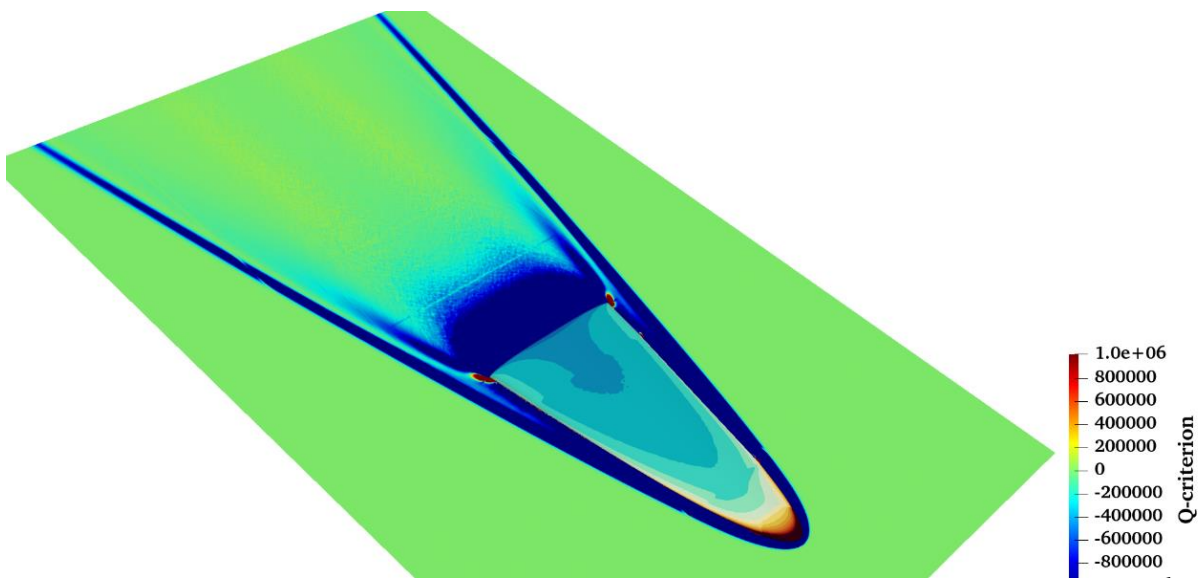
Figure 25: Q-criterion contours on a horizontal plane parallel to the vehicle.
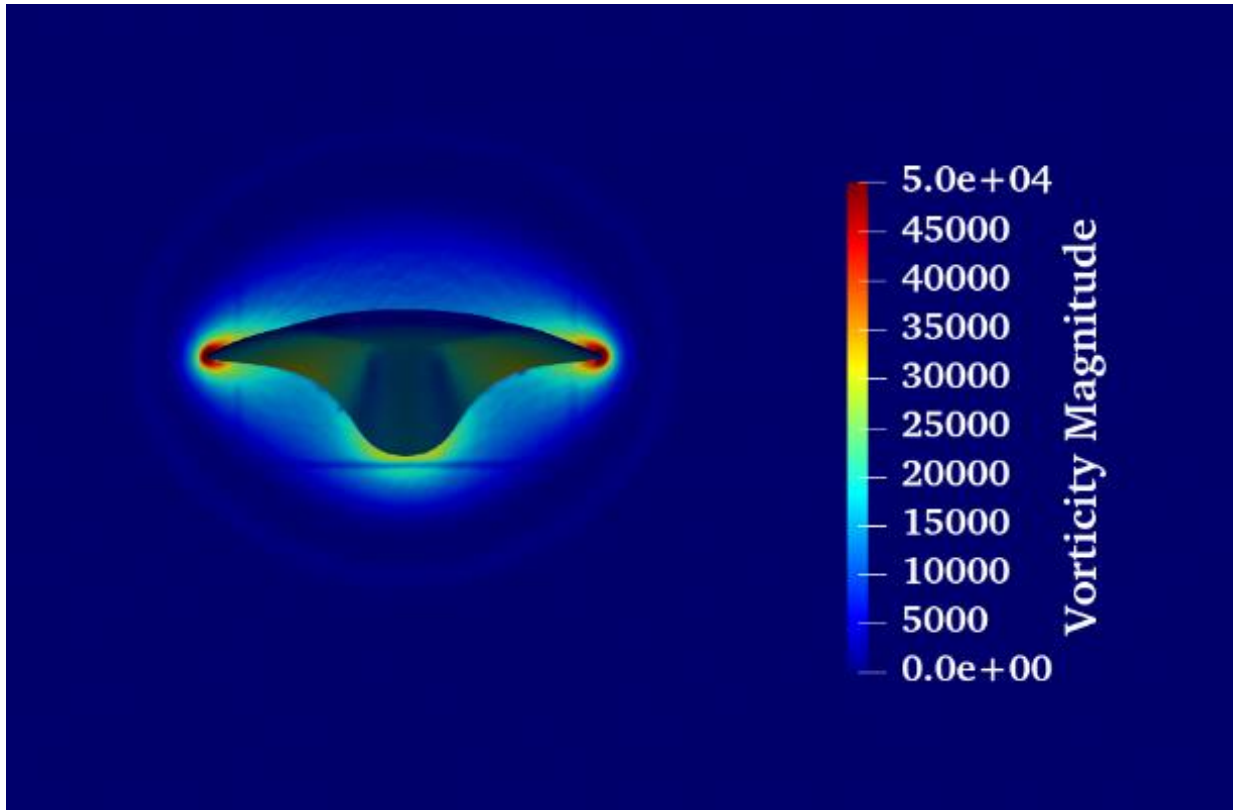
Figure 26: *Vorticity magnitude at the back of the vehicle.*

Due to the complexity of the vehicle, it was considered appropriate to also present three-dimensional iso-surfaces of the Q-criterion around the vehicle, so as to identify the three-dimensional shape of the shock and the structured vortices. Figure 27 presents the three-dimensional Q-criterion contours around the vehicle, colored by vorticity magnitude. The transparent grey contours correspond to the three-dimensional outer shape of the shock. A part of the shockwave close to the compression surface can be also observed in the same Figure 27.

In Figure 28 the same contours are plotted but this time colored by the velocity magnitude. As it can be observed in Figure 28, about *30 cm* downstream the nose of the vehicle, where the compression surface is steeper, the vortices separate from the flow and continue downstream to the higher pressure area towards the back side of the vehicle. Due to the angle of the compression surface towards the end of the vehicle, a pressure rise is evidenced and the flow slows down about *1000 m/s* within a few centimeters.
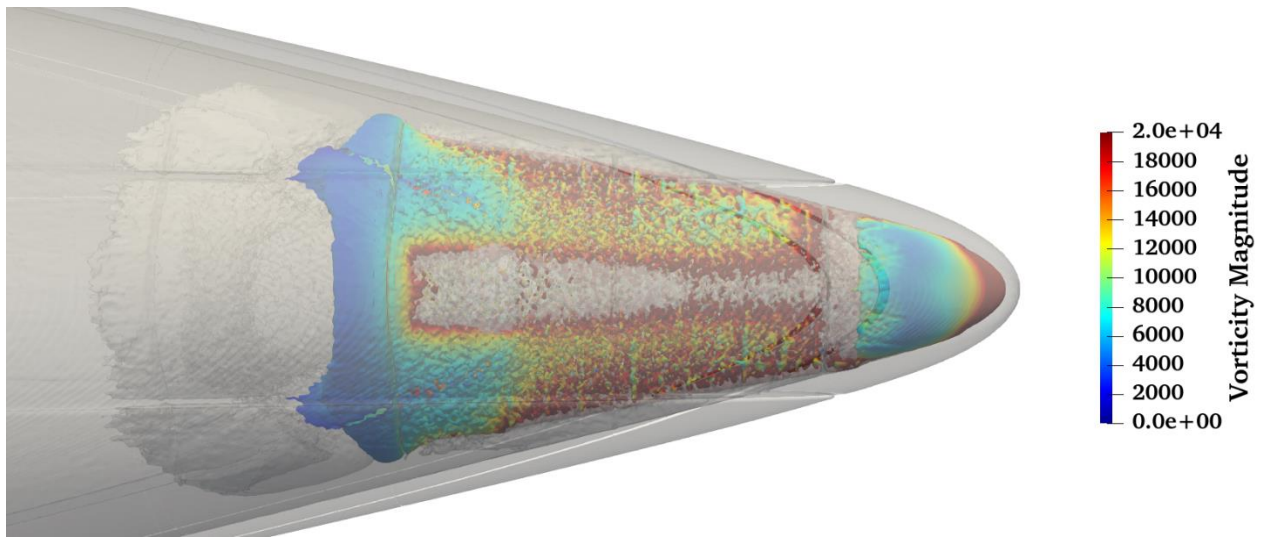
Figure 27: Three-dimensional Q-criterion contours colored by vorticity magnitude.
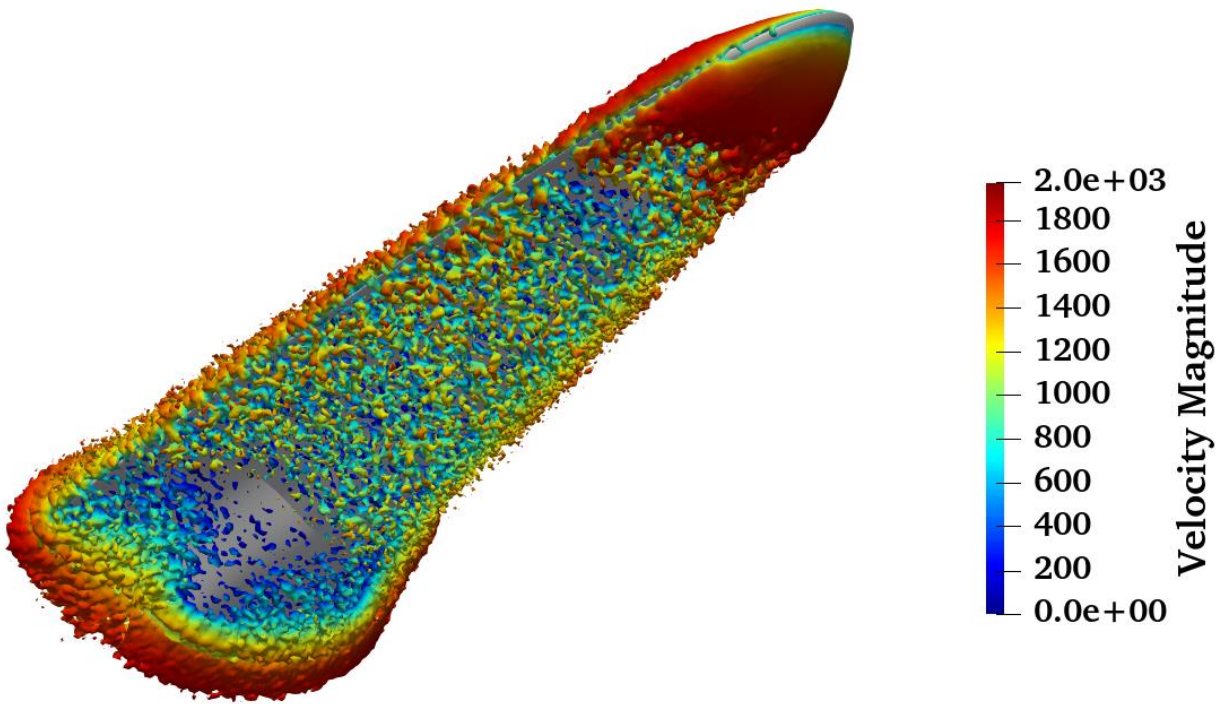
Figure 28: Overview of the three-dimensional Q-criterion contours around the vehicle colored by velocity magnitude.

To calculate lift and drag the shear stresses and the pressure three-dimensional components have been computed. The lift and drag (per unit surface) at each surface cell can be seen in Figure 29. From that figure we can also see that the maximum drag is concentrated at the tip of the nose whereas the

area below the nose generates also a large amount of lift. By integrating the values of all cells, the total lift and drag have been calculated, while the ratio L/D was calculated being equal to **2.18**. According to the open literature, this value if a typical one for a waverider flying at 0-degrees angle of attack [31]. A value of L/D of above 2.0 yields a good vehicle performance for the design condition selected. Only one angle of attack was examined in this case; according to reference 29 a slightly positive angle of attack can increase the L/D ratio, thus performance, two to three times compared to the reference one.

In the open literature, waveriders are usually analyzed between 25 km and 40 km and not in 90 km, as in this work. This fact has an impact to lift generation on the surface by the fluid, thus in this design the compression surface is larger than a conventional compression surface seen in waveriders flying in lower altitudes.
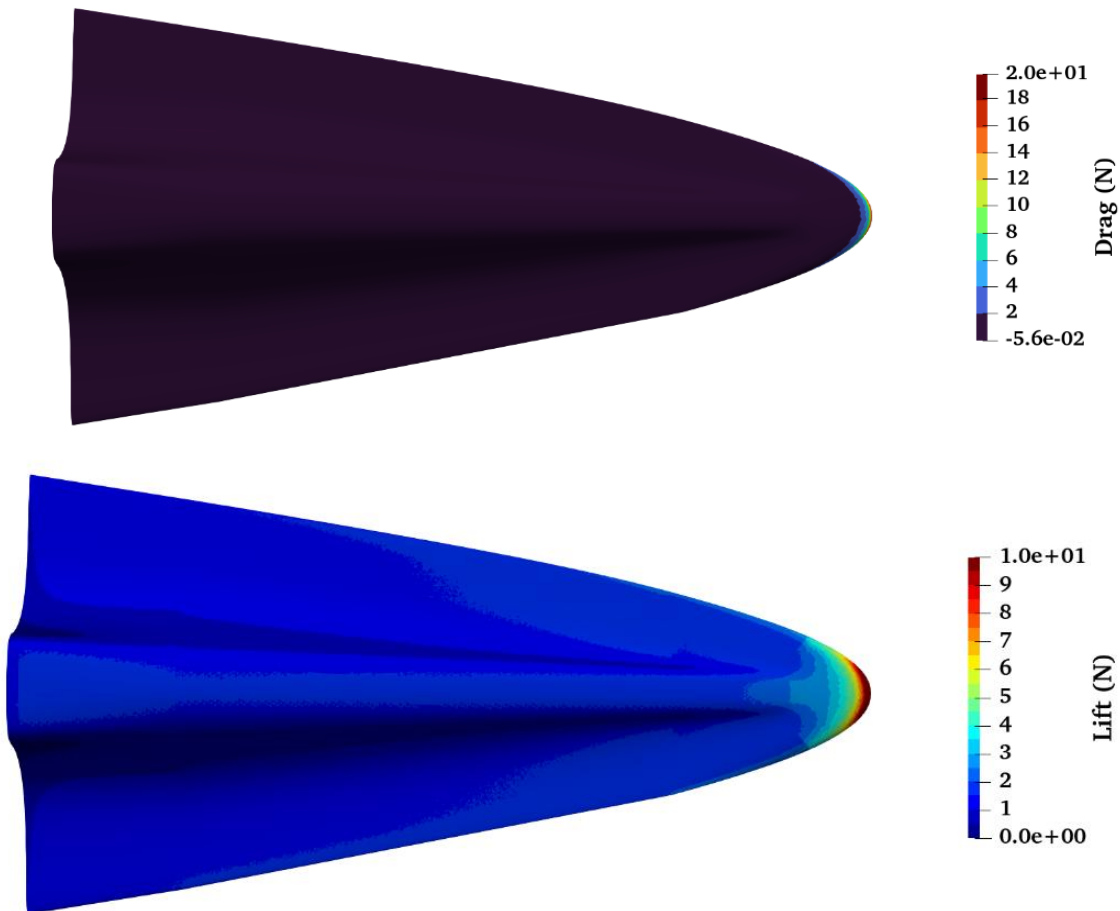
Figure 29*. Overview of the lift (bottom) and drag (top) exerted on the waverider's surface.*

# 4. Preliminary design of a scramjet-powered hypersonic vehicle

In the 1980s, aerospace researchers and engineers initiated the ambitious National Aerospace Plane (NASP) program. This endeavor was designed to investigate the viability of a single-stage to orbit (SSTO) vehicle capable of both taking off and landing horizontally. A cornerstone of the program was the development and integration of supersonic combustion ramjet (scramjet) engines into the vehicle. Although the program was prematurely terminated in the 1990s, its foundational work became a vital reference for future initiatives in hypersonic aerodynamics. The dissolution of the NASP program gave rise to the Hypersonic Systems Technology Program (HySTP) in late 1994. Although short-lived, being discontinued in 1995, HySTP aimed to transform the technical insights acquired from NASP into technology demonstrators. However, a more significant stride in hypersonic research was made by the NASA X-43A. Under NASA's Hyper-X program, this vehicle attained world speed records, reaching Mach 6.8 and Mach 9.6 on separate missions, thanks to its scramjet propulsion [32].

In the context of renewed global interest in space exploration, hypersonic vehicles powered by scramjets are gaining traction. Scramjets present an engineering innovation over conventional turbojet engines. Unlike their turbojet counterparts, which utilize high-speed rotating gas turbines to power the air compressors, scramjets employ oblique shock waves generated in front of the engine's inlet to compress incoming air. Notably, the entire airflow within the scramjet engine remains supersonic, unlike in ramjets where combustion occurs at subsonic speeds. The synergy between the airframe and engine—demonstrated in configurations like NASP and X-43A, is critical for the optimal performance of scramjet-powered vehicles. The versatility and cost-efficiency of scramjets have spurred interest in their integration into multi-stage launch systems. Scramjets, being air-breathing engines, offer the advantage of eliminating the need for onboard oxidizers. This, in turn, leads to substantial weight reductions and increased payload capacities, thereby lowering overall mission costs.

In the present study, an exploratory design framework for a hypersonic vehicle found in the open literature [33] has been established through a two-dimensional geometry simulation, and is shown in Figure 30. The choice to commence with a 2D model is motivated by several factors: it provides crucial insights into the shock wave dynamics, offers rapid simulation times, and serves as a robust preliminary design model for subsequent 3D studies. The vehicle's specifications are informed by the dimensions of the X-51 A [34] (as an order of magnitude), resulting in a design that is 7.62 meters long, featuring a 3.58-meter forebody, a 1.52-meter engine length, and a 0.27-cm engine intake width. The angle of the upper surface is set at 3 degrees, while the lower surface is inclined at 6 degrees to facilitate air compression.
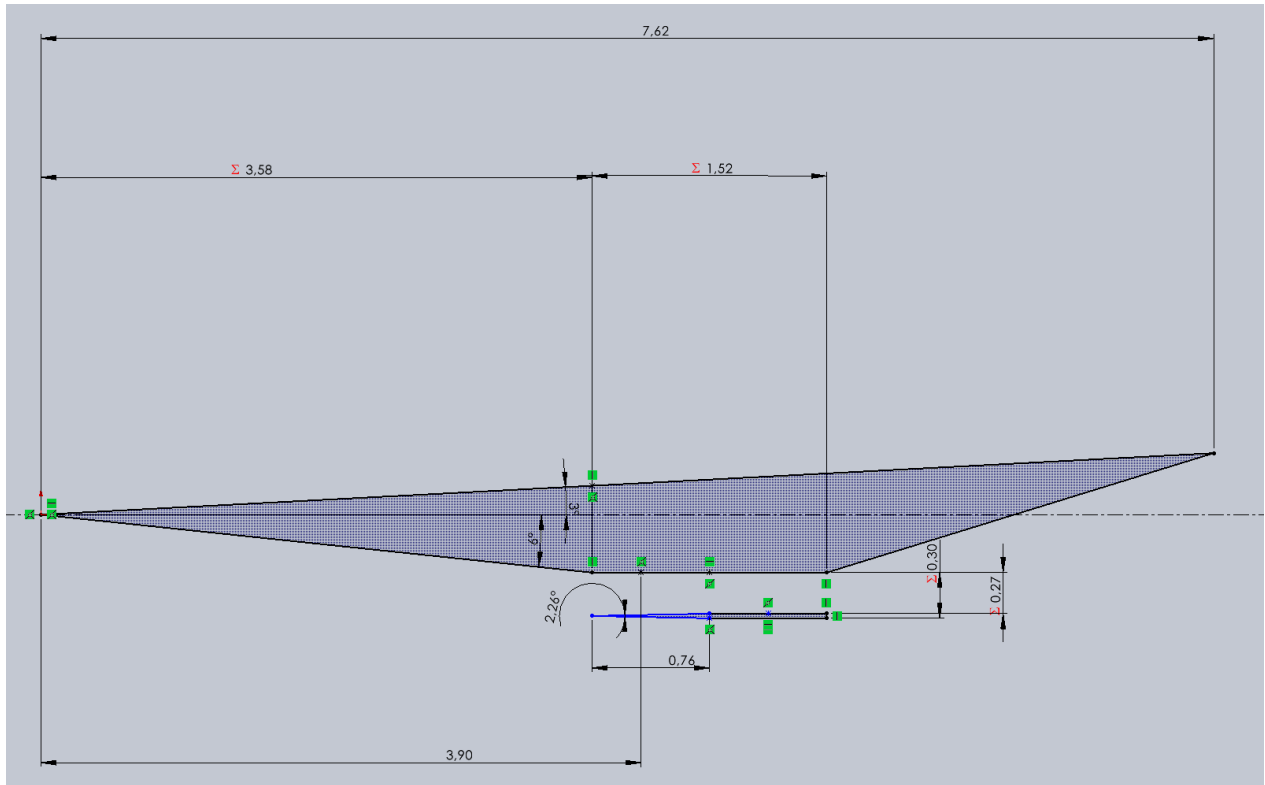
Figure 30: *Hypersonic vehicle two-dimensional geometry.*

The flow simulation was performed using the DSMC code SPARTA, with inlet flow conditions corresponding to a flight altitude of 90 km and a Mach Number 6 (the US Standard Atmosphere Model was used as a reference). The engine is fed with compressed air through an oblique shock originating from the nose of the vehicle, as demonstrated in Figure 31. It can be observed in Figure 32 that the density of air at the engine's inlet is approximately twice the density of the freestream. The engine's inlet geometry compresses the flow further to a final value of 3.75 times the freestream value. Figure 31 confirms the accurate positioning and opening of the engine.
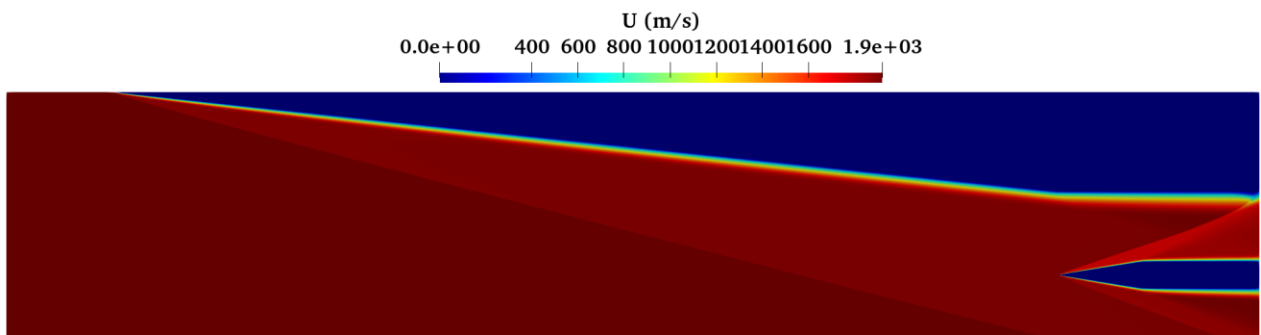
Figure 31: *Flow velocity along x-axis, for the two-dimensional geometry of Figure 30.*
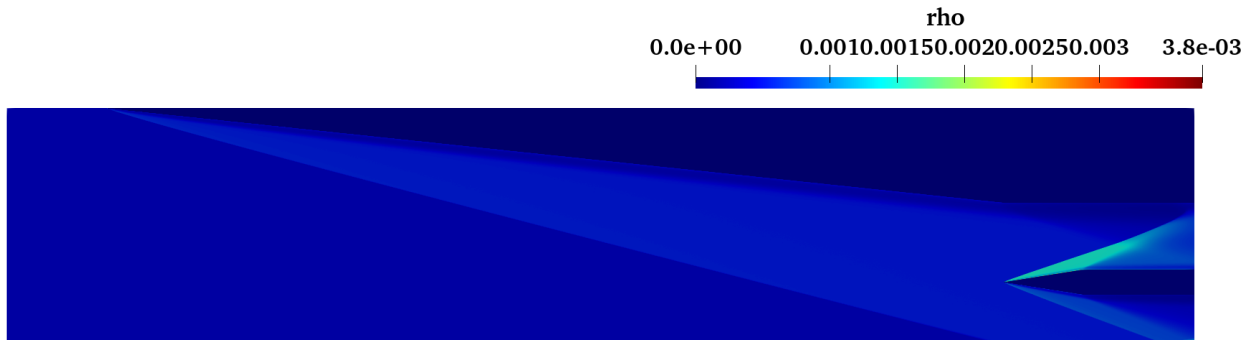
Figure 32: *Flow field density, for the two-dimensional geometry of Figure 30.*

5. Design of a scramjet-powered hypersonic vehicle

The theoretical foundation of scramjet engines was laid in the mid-20th century [35], but it took decades of research to achieve the first successful flight. The X-43, developed by NASA, set a record speed for an air-breathing engine in 2004 [36]. These hypersonic vehicles face many challenges, such as strong shock waves causing high temperatures and pressures [37], while understanding the interaction between the boundary layers and shock waves is essential for stability [38]; furthermore, specialized materials and cooling systems are needed to manage the extreme temperatures exerted during a hypersonic flight [39].

The scramjet engine design is divided in three stages. The inlet design, combustion chamber design and nozzle design. According to Heiser et al. [40] the inlet must generate efficient compression without subsonic deceleration (which means that only oblique shocks with small angles, with respect to the direction of flight, should be generated). The combustion chamber must provide a stable combustion at supersonic speeds [41]. The nozzle on the other hand must optimize thrust across varying flow conditions [42]. Scramjet-powered hypersonic vehicles are a complex and fascinating field, bridging aerodynamics, CFD, propulsion, materials science, and more. Continuous advancements are being driven by researchers worldwide, setting the stage for potential revolutionary changes in aerospace transportation and defense.
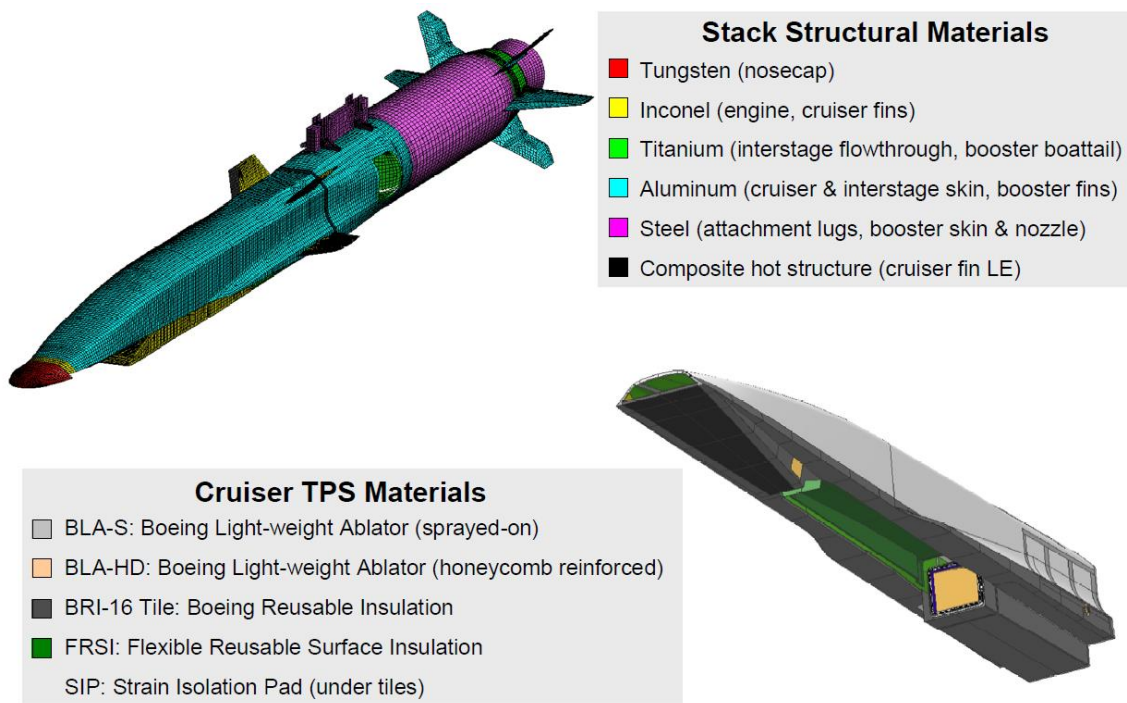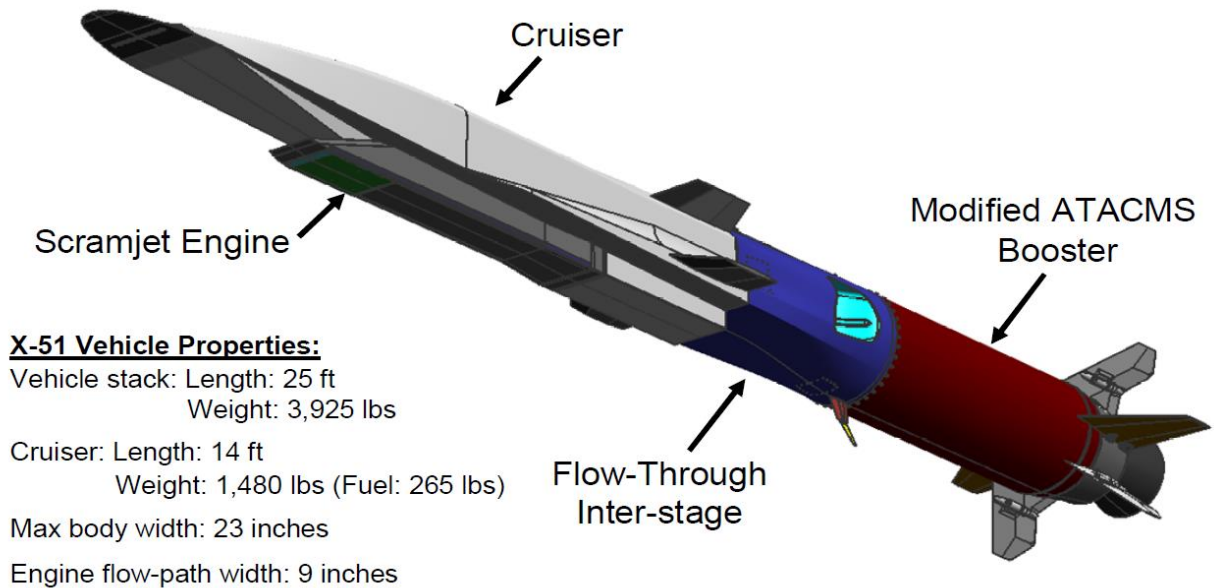
Furthermore, one of the vital aspects of hypersonic vehicles is the selection of materials that can withstand extreme thermal loads. This is not only pertinent to the external surface, but also to the internal structure, including engine components. Advanced materials such as Ceramic Matrix Composites and Nickel alloys have been explored to fulfill these requirements [43]. Moreover, effective cooling strategies are equally crucial in maintaining structural integrity. Active and passive cooling systems have been employed to manage the intense heat. Active cooling systems typically involve circulating a coolant, such as water, liquid fuel, or liquid metal, within the structure, while passive systems rely on heat-resistant materials and coatings [44].

To extend the aforementioned findings, a three-dimensional scramjet-powered hypersonic vehicle was designed, specifically targeting performance enhancements and optimization in both aerodynamics and propulsion systems. As the most successful hypersonic vehicle to date, the geometry of the X-51A was used as a foundational reference, given its proven success in achieving sustained hypersonic flight. The major objective of the X-51A program was to test the HyTech scramjet engine, using endothermic hydrocarbon fuel, by accelerating the corresponding vehicle from boost, at approximately Mach 4.5, to Mach 6.5 and beyond. Additional goals of the program were: a) to acquire ground and flight data on an actively cooled, self-controlled operating scramjet engine, b) to demonstrate the viability of an endothermically fueled scramjet in flight and c) to produce higher thrust than drag and demonstrate the feasibility of a free-flying, scramjet powered vehicle.
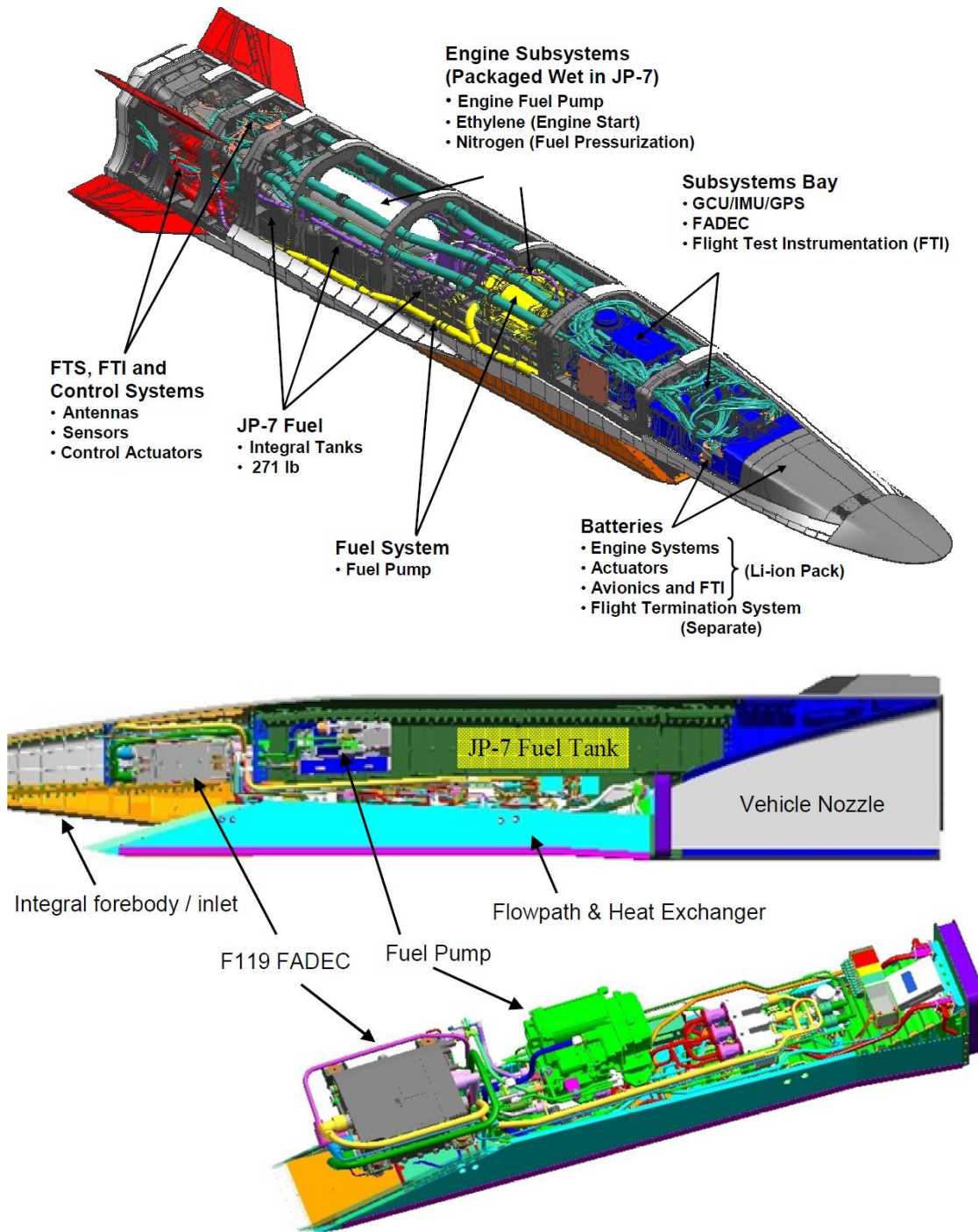
After a thorough research, two-dimensional plans of the aforementioned vehicle were found, and although the authors cannot guarantee the accuracy of the plans, they offer a critical starting point [45]. Taking these plans as a reference, a three-dimensional geometry similar to X-51A was designed

empirically, carefully considering the critical areas of design that influence performance at hypersonic speeds.

Additional information was retrieved from related publications; characteristic views of some critical parts and systems of the vehicle are presented in the following Figures 33 to 35.

Cruiser

Scramjet Engine

Modified ATACMS Booster

Flow-Through Inter-stage

X-51 Vehicle Properties:
Vehicle stack: Length: 25 ft
            Weight: 3,925 lbs

Cruiser: Length: 14 ft
           Weight: 1,480 lbs (Fuel: 265 lbs)

Max body width: 23 inches

Engine flow-path width: 9 inches

Stack Structural Materials
- ■ Tungsten (nosecap)
- ■ Inconel (engine, cruiser fins)
- ■ Titanium (interstage flowthrough, booster boattail)
- ■ Aluminum (cruiser & interstage skin, booster fins)
- ■ Steel (attachment lugs, booster skin & nozzle)
- ■ Composite hot structure (cruiser fin LE)

Cruiser TPS Materials
- ■ BLA-S: Boeing Light-weight Ablator (sprayed-on)
- ■ BLA-HD: Boeing Light-weight Ablator (honeycomb reinforced)
- ■ BRI-16 Tile: Boeing Reusable Insulation
- ■ FRSI: Flexible Reusable Surface Insulation
-   SIP: Strain Isolation Pad (under tiles)

Figure 33: The X-51A vehicle and materials used [46].

**Engine Subsystems
(Packaged Wet in JP-7)**
• Engine Fuel Pump
• Ethylene (Engine Start)
• Nitrogen (Fuel Pressurization)

Subsystems Bay
• GCU/IMU/GPS
• FADEC
• Flight Test Instrumentation (FTI)

**FTS, FTI and
Control Systems**
• Antennas
• Sensors
• Control Actuators

JP-7 Fuel
• Integral Tanks
• 271 lb

Fuel System
• Fuel Pump

Batteries
• Engine Systems
• Actuators
• Avionics and FTI   } (Li-ion Pack)
• Flight Termination System
  (Separate)

JP-7 Fuel Tank

Vehicle Nozzle

Integral forebody / inlet

Flowpath & Heat Exchanger

F119 FADEC   Fuel Pump

*Figure 34:* *The X-51A subsystems and propulsion configuration [46].*
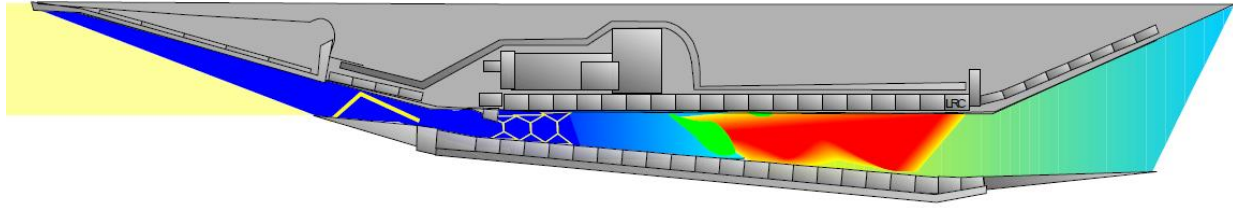
Figure 35: Typical flow formations inside a scramjet engine [47].

Figure 36 shows an overview of the designed 3D hypersonic vehicle. As seen, the basic shape of the X-51A vehicle has been preserved, adhering to the well-established principles of hypersonic aerodynamics. Furthermore, an approximate geometry of the scramjet inlet underneath the vehicle has been designed, reflecting the complex flow characteristics typical of hypersonic inlets, as well as an approximate internal geometry of the engine, as shown in Figure 37, which contains sectional views of the vehicle.
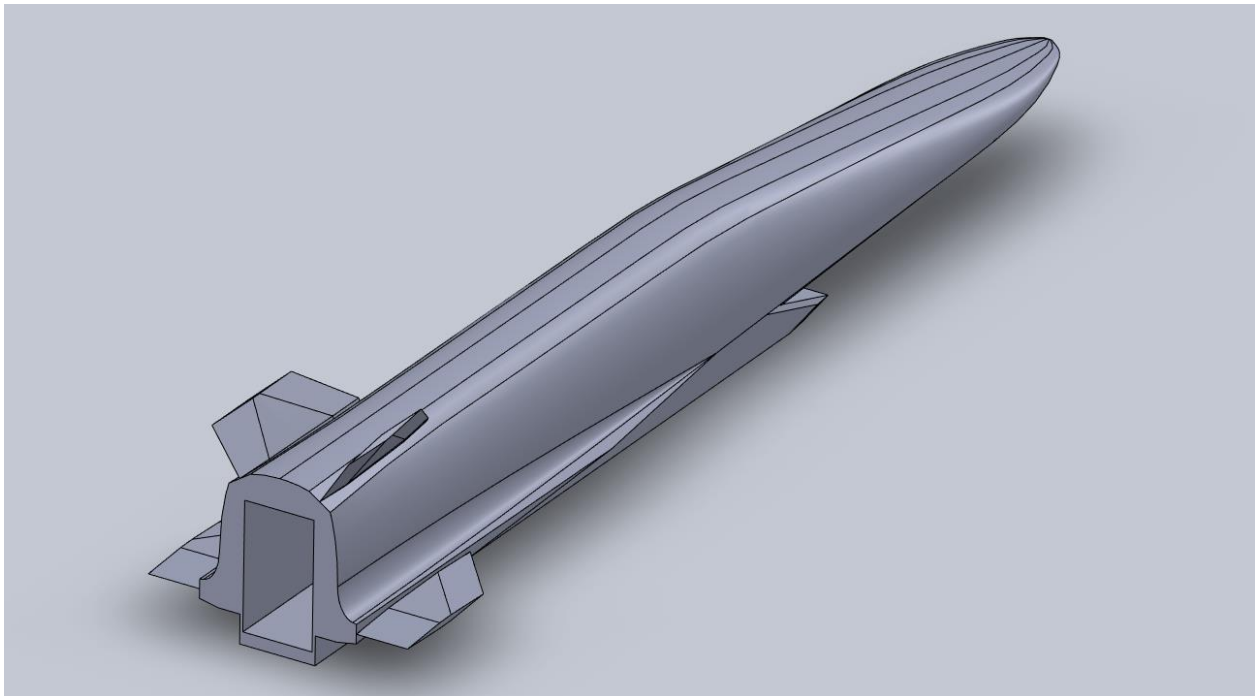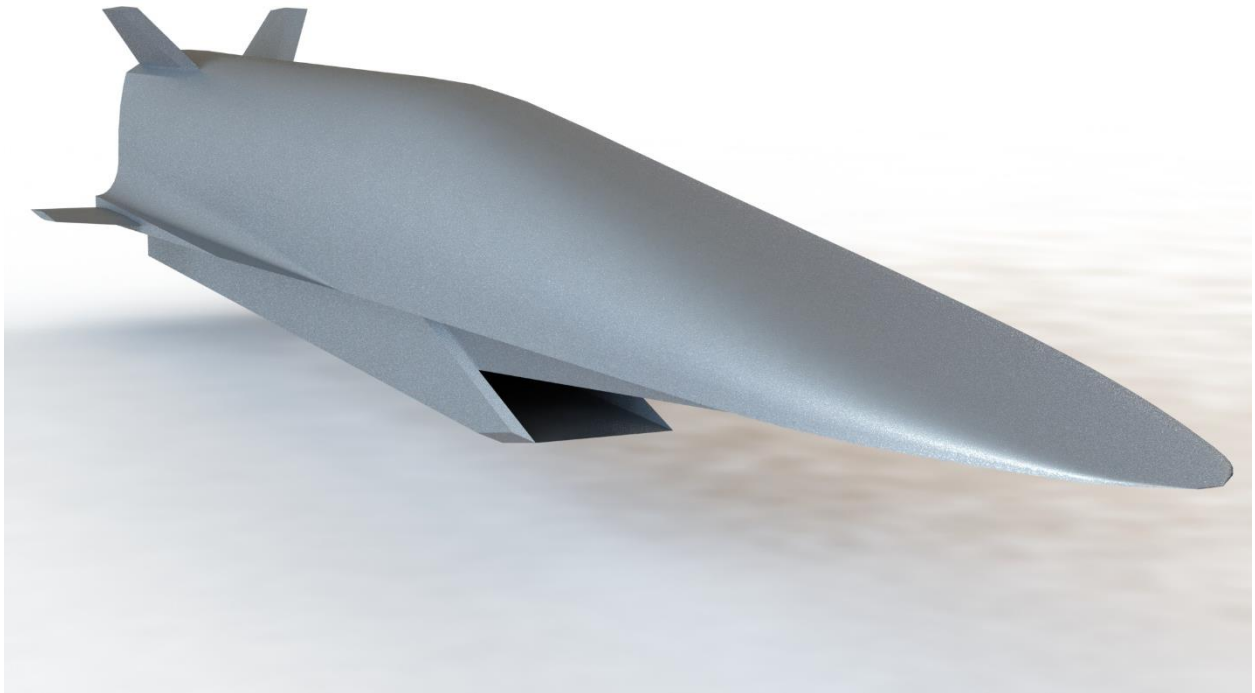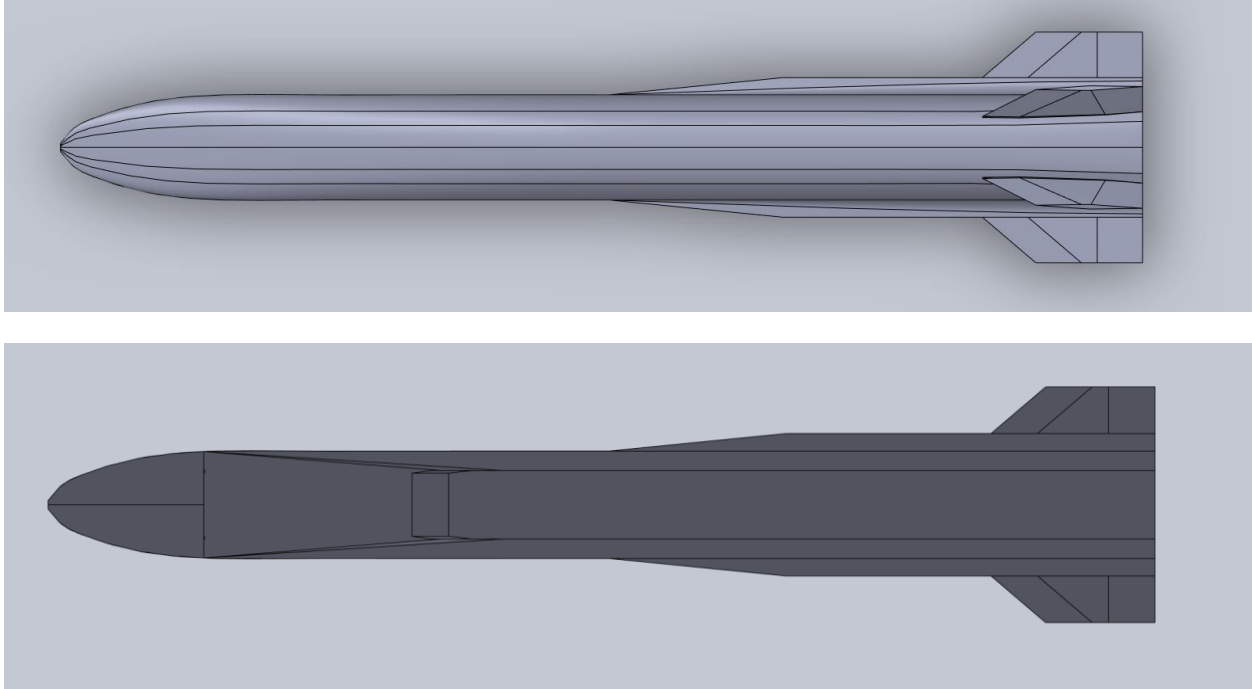
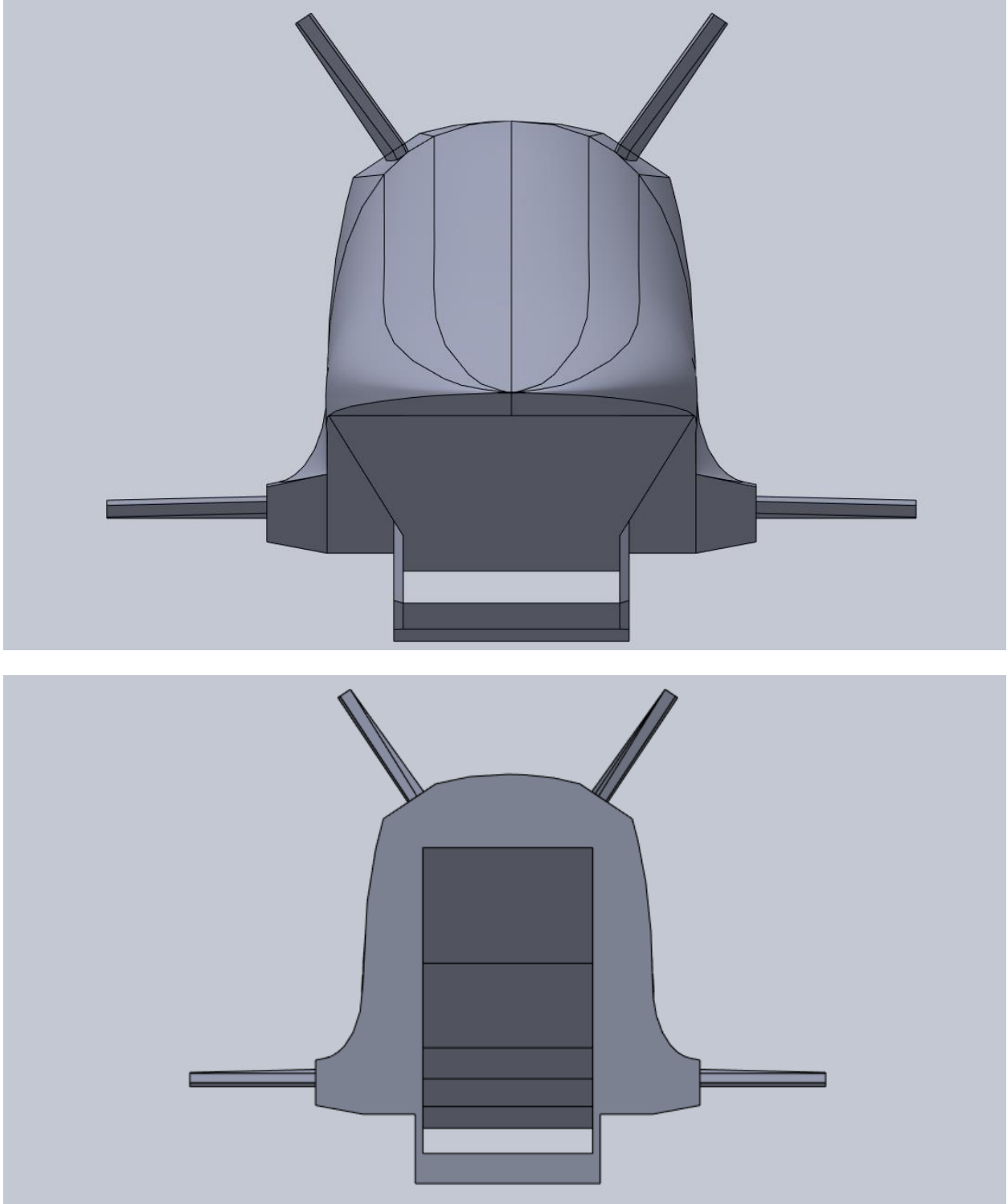*Figure 36:* *Overview of the three-dimensional CAD model of the designed hypersonic vehicle.*
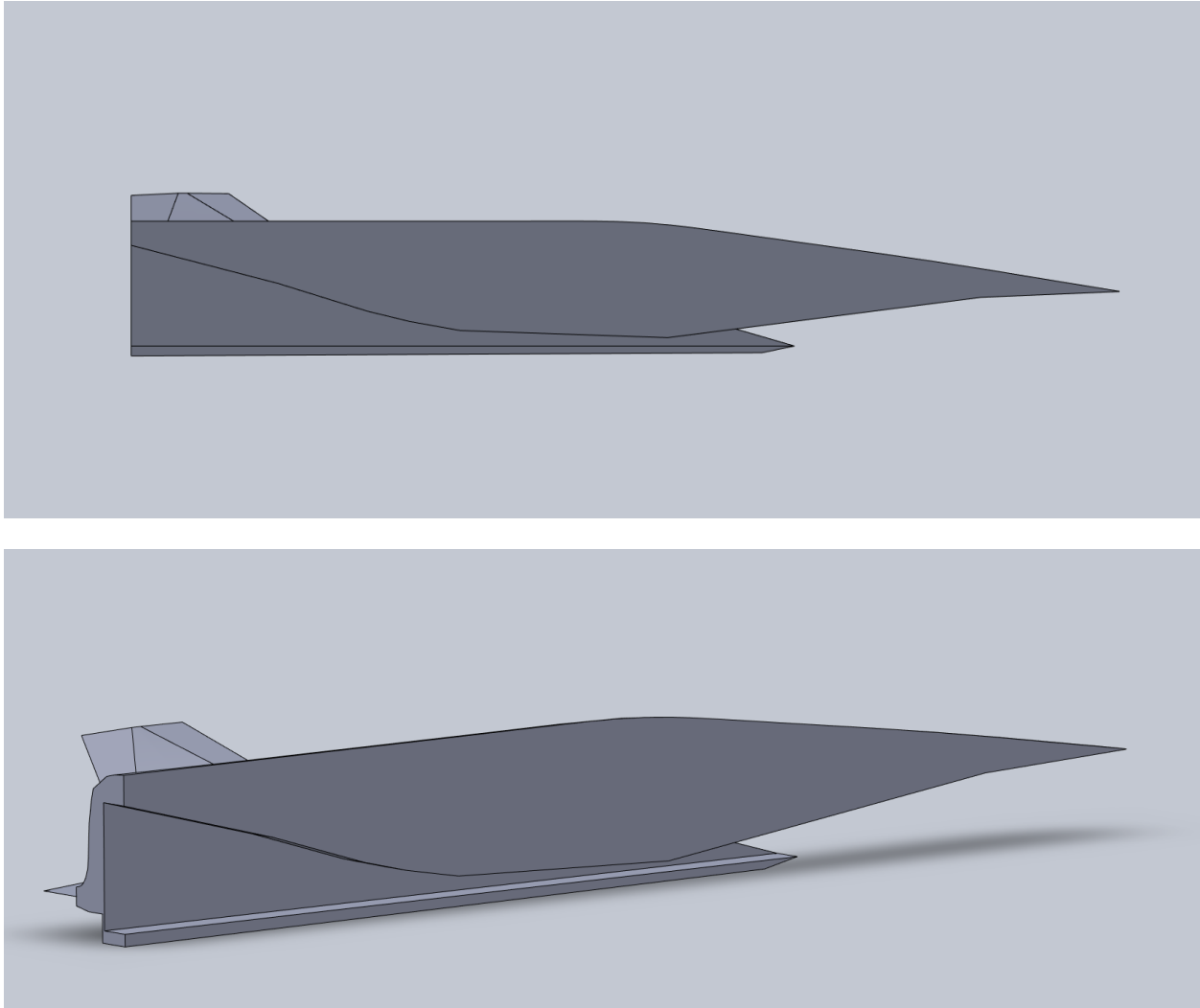
Figure 37: Sectional views (symmetry plane section) of the three-dimensional vehicle shown in Figure 36.

More views of the vehicle are presented in Figures 38 to 40. Taking into consideration all of the above, the resulting geometry is a hypersonic vehicle with a length slightly larger than 4 m and a maximum width of 0.86 m (including the horizontal fins). The engine below the vehicle has a length of approximately 2.7 m, while the intake opening is 0.23 m. As seen in Figure 37, the engine features a diverging exhaust nozzle; the design of the nozzle is critical for achieving optimal performance at the high temperatures and pressures encountered at hypersonic speeds. The engine is embedded within the vehicle's geometry, and the front lower part of the vehicle is used as a compression ramp, an essential feature for scramjet operation. In the same manner, the simulation conditions for this vehicle have been taken from the US Standard atmosphere table for an altitude of 90 km. This altitude, although high for scramjet-powered vehicles, was chosen to be the same with the previous simulations of the other two vehicles reported in the previous sections of this Report, for comparison purposes (additional simulations in lower altitudes will be performed in the following phases of the Project).

Figure 38: *Top and bottom views of the three-dimensional vehicle shown in Figure 36.*

The vehicle speed is Mach 9, which at that altitude represents a rarefied flow condition. Additional analysis was carried out to evaluate the shockwave interactions that would be present in such a high-speed environment. The selected flight trajectory and operational parameters were also assessed to verify that they align with the performance capabilities of such a vehicle. Fluid dynamics computational simulations using the DSMC method were conducted to validate the design and identify areas where further optimization could be achieved. In conclusion, this design represents a synthesis of advanced engineering principles, informed by prior successes in hypersonic flight, and refined through rigorous analysis and simulation. The result is a promising step towards expanding our understanding and capabilities in hypersonic vehicle design and technology, and it invites further research and development to realize its full potential.

Figure 39: Front and rear views of the three-dimensional vehicle shown in Figure 36.
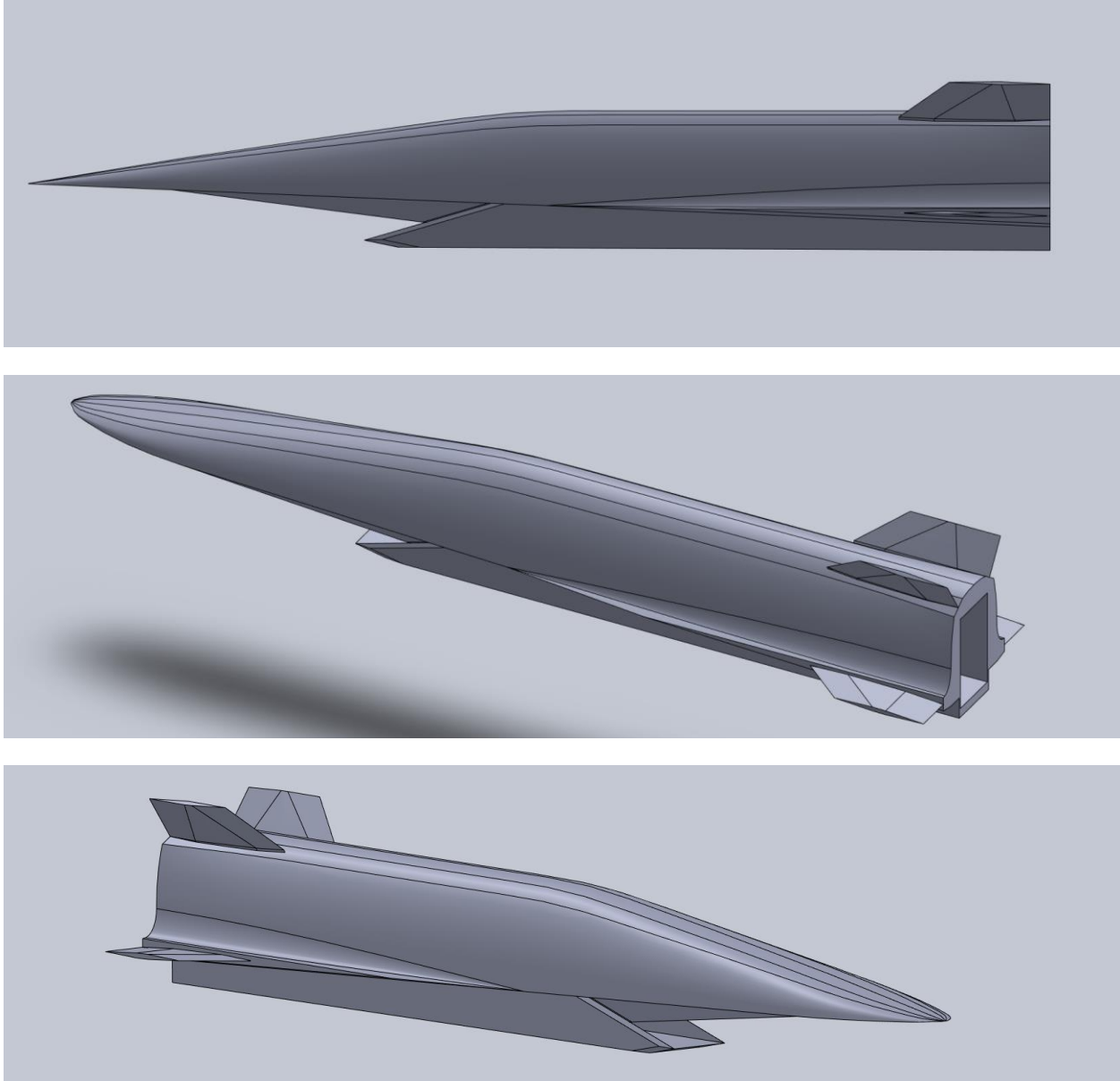
Figure 40: Alternative views of the three-dimensional vehicle shown in Figure 36.

The simulation parameters can be found in Table 3. The complexity of the hypersonic flow around this specific vehicle necessitated a meticulous grid refinement strategy. A high number of cells was essential to capture the nuances of the flow field, particularly around the shock areas, where rapid changes in flow properties occur. The refinement strategy ensured that the grid resolution was finer in regions with high gradients, such as at the shock waves and at the engine's internal area. Furthermore, as seen in Table 3, more than **five billion particles were used in this simulation**. The engine's internal region presents unique challenges, as the pressure and temperature can vary significantly. Additional refinement was necessary to capture the effects of shocks, expansion waves, and other complex flow behaviors. Finally, for this particular test case, **an impressive computational setup was employed, utilizing 23,040 CPUs for a total of 7.2 hours**. This

substantial computational commitment underscores the complexity of simulating hypersonic vehicles. In order to obtain a fully converged flow field, the flow was given a transient period of 50,000 time-steps in order to obtain steady state and then 50,000 samples were acquired in order to reduce statistical fluctuations.

Table 3: DSMC computational parameters for Mach 9 flow at 90 km altitude, for the scramjet-powered vehicle.

Number density, Nd_∞ (#/m³)	2.00×10^{20}
Timestep (s)	3.0×10^{-7}
Transient period	50,000
Sample period	50,000
Number of particles (#)	5.8×10^{9}
Number of cells	114,500,000
Wall-clock time (CPU hours)	165,888

Figures 41, and 42 contain views of the surface grid, which is required for the construction of the final 3D Cartesian grid, for the DSMC flow simulation. Figure 43 contains a view of the three-dimensional computational grid, which is used for the flow simulation with the DSMC code SPARTA.
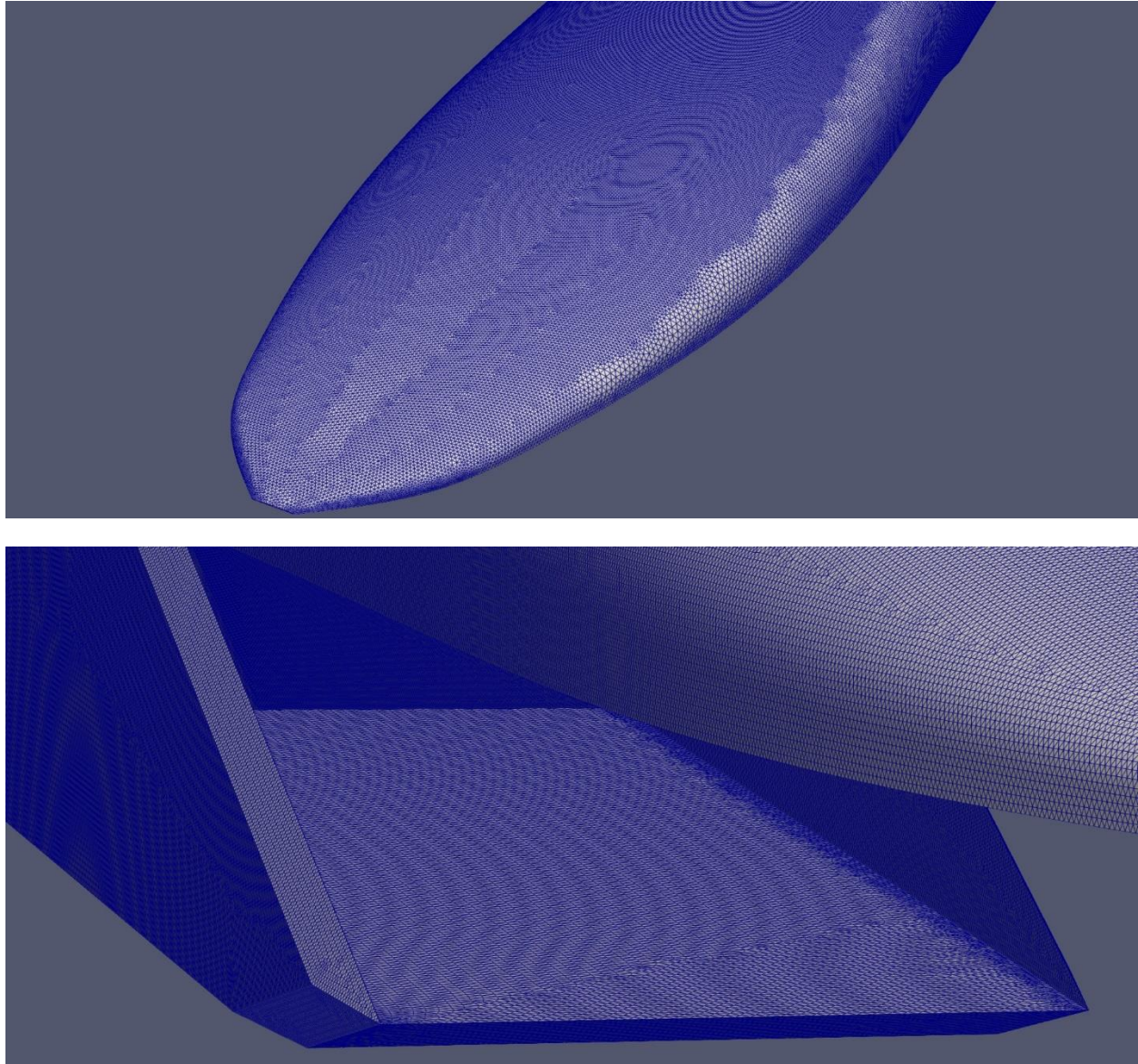
Figure 41: *Views of the initial surface grid of the vehicle (nose region and engine inlet).*
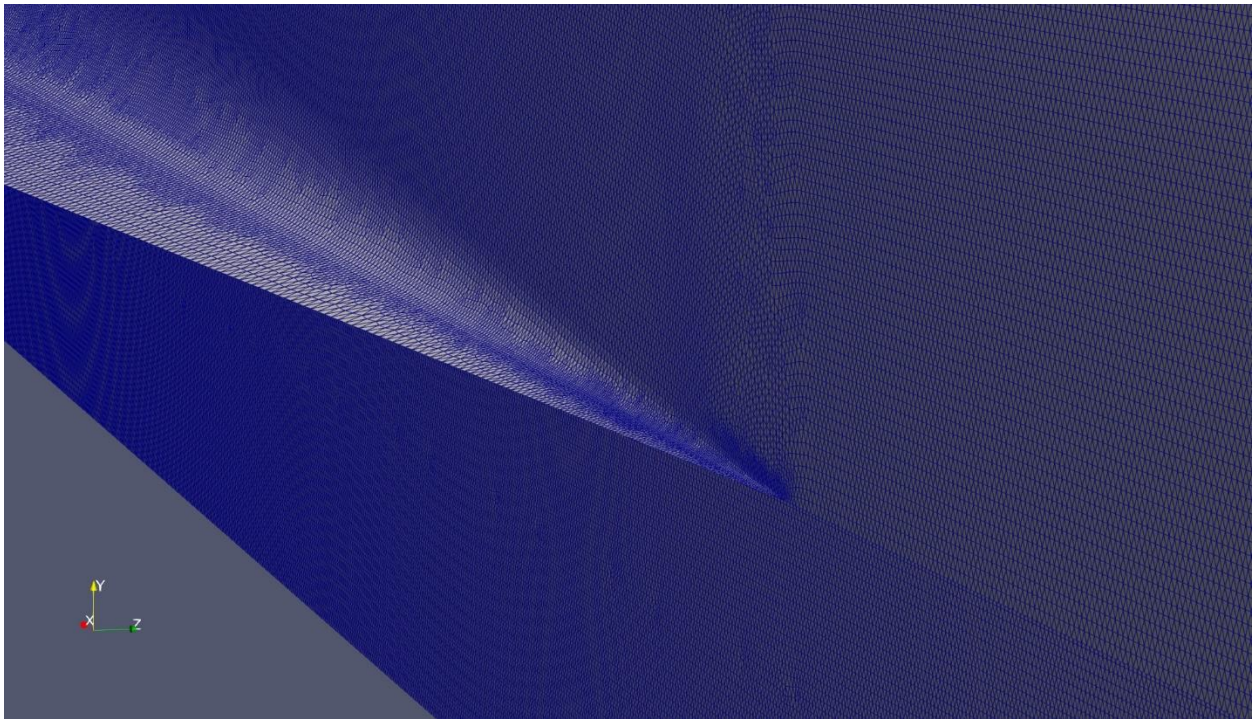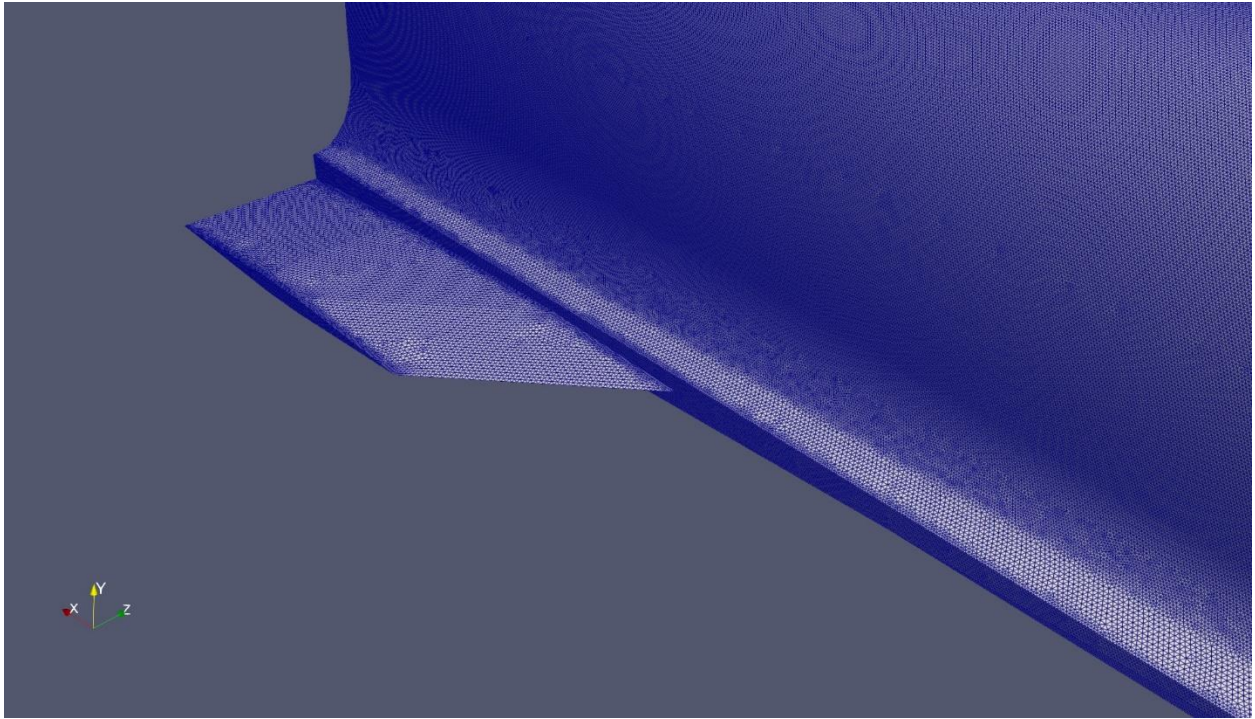
Figure 42: Views of the initial surface grid of the vehicle (horizontal fin and leading edge of the small wedge-like wing).

45
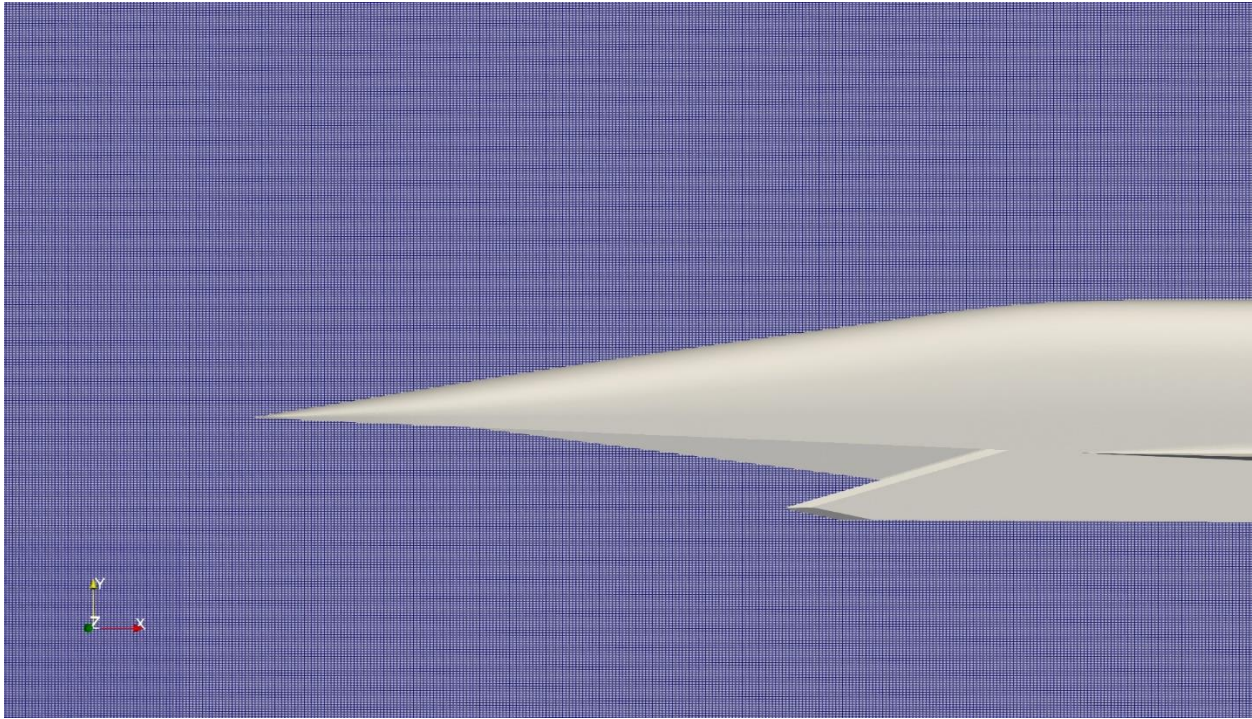
Figure 43: *Sectional view of the computational grid used for the DSMC simulation of the designed hypersonic vehicle.*

Figure 44 and 45 provide a striking visual representation of the intricate streamwise velocity (U in m/s) flow dynamics around the hypersonic vehicle equipped with a scramjet engine. A spectrum of color contours graphically depicts the streamwise velocity values, computed in the vehicle's direction of travel. The warmer hues reds and oranges indicate areas of higher velocity, while the cooler colors blues and greens point to relatively lower velocities in comparison with the vehicle's speed. Starting with the upstream direction, with respect to the nose of the hypersonic vehicle, it's immediately noticeable that the streamwise velocity contours show a high magnitude (in the order of 2500 m/s), due to the high speed of the vehicle (Mach 9 in this case). At the highly inclined lines, where an abrupt change in color is observed, oblique shocks are formed, where the flow decelerates and the pressure increases (however behind an oblique shock the flow remains supersonic – something that is a prerequisite in this case so as to maintain supersonic flow conditions through the scramjet engine). The oblique shock waves are better observed in pressure and density contours, in the following figures. The blue regions attached to the solid surfaces of the vehicle correspond to low velocity regions, due to the formation of boundary layers (relatively thick, in the rarefied conditions, at the high altitude of flight).

Moving downstream along the surface, interactions between the boundary layers and the shock waves become visible. These interactions influence heat transfer, pressure distribution, and, ultimately, the overall performance of the hypersonic vehicle. At Mach 9, these interactions are exacerbated and require precise aerodynamic design, to ensure that the vehicle's surface can withstand the aerothermal loads.
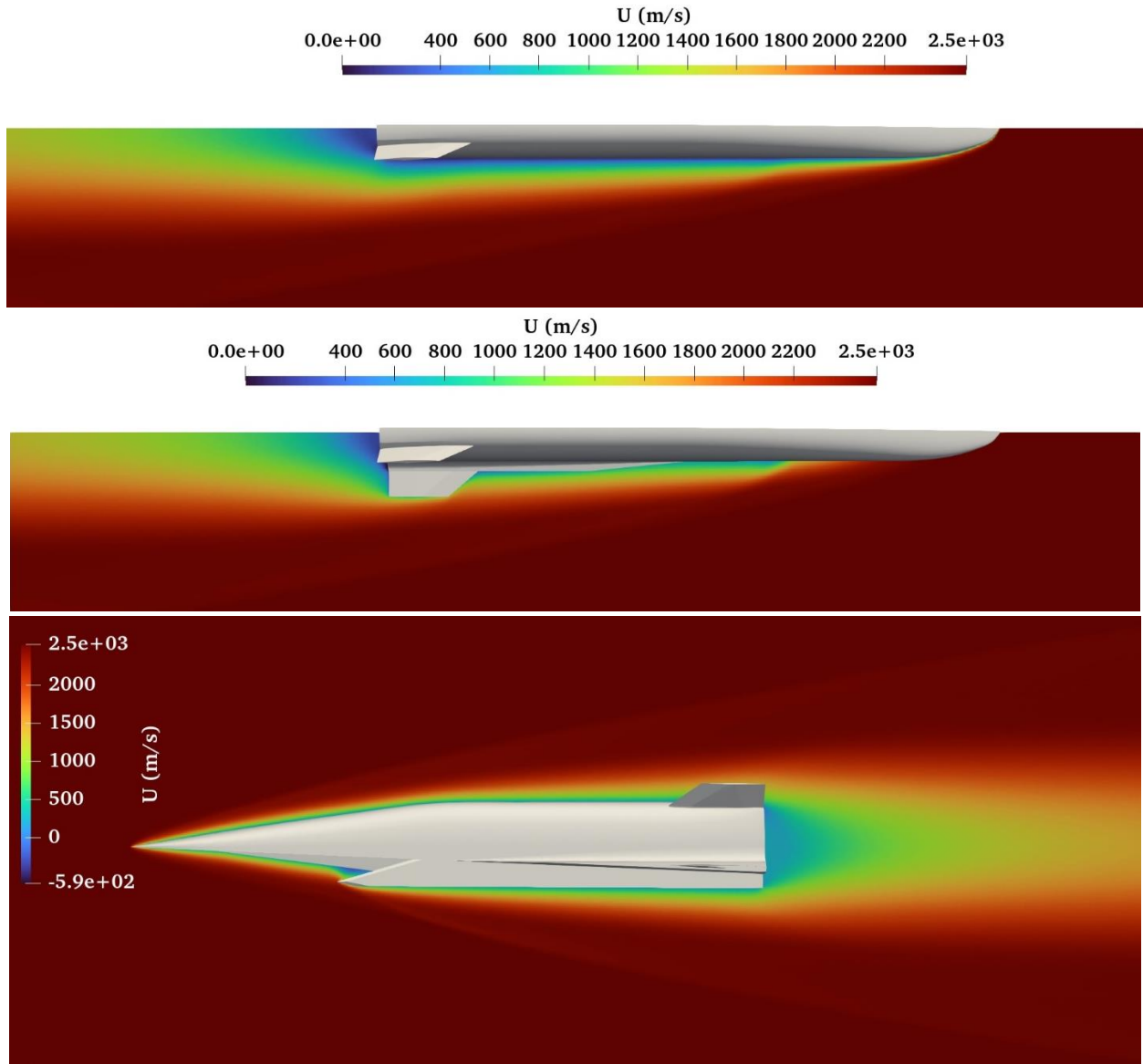
Figure 44: *Streamwise velocity contours. Top: at the nose level. Middle: at the level of the horizontal fin. Bottom: at the symmetry plane.*
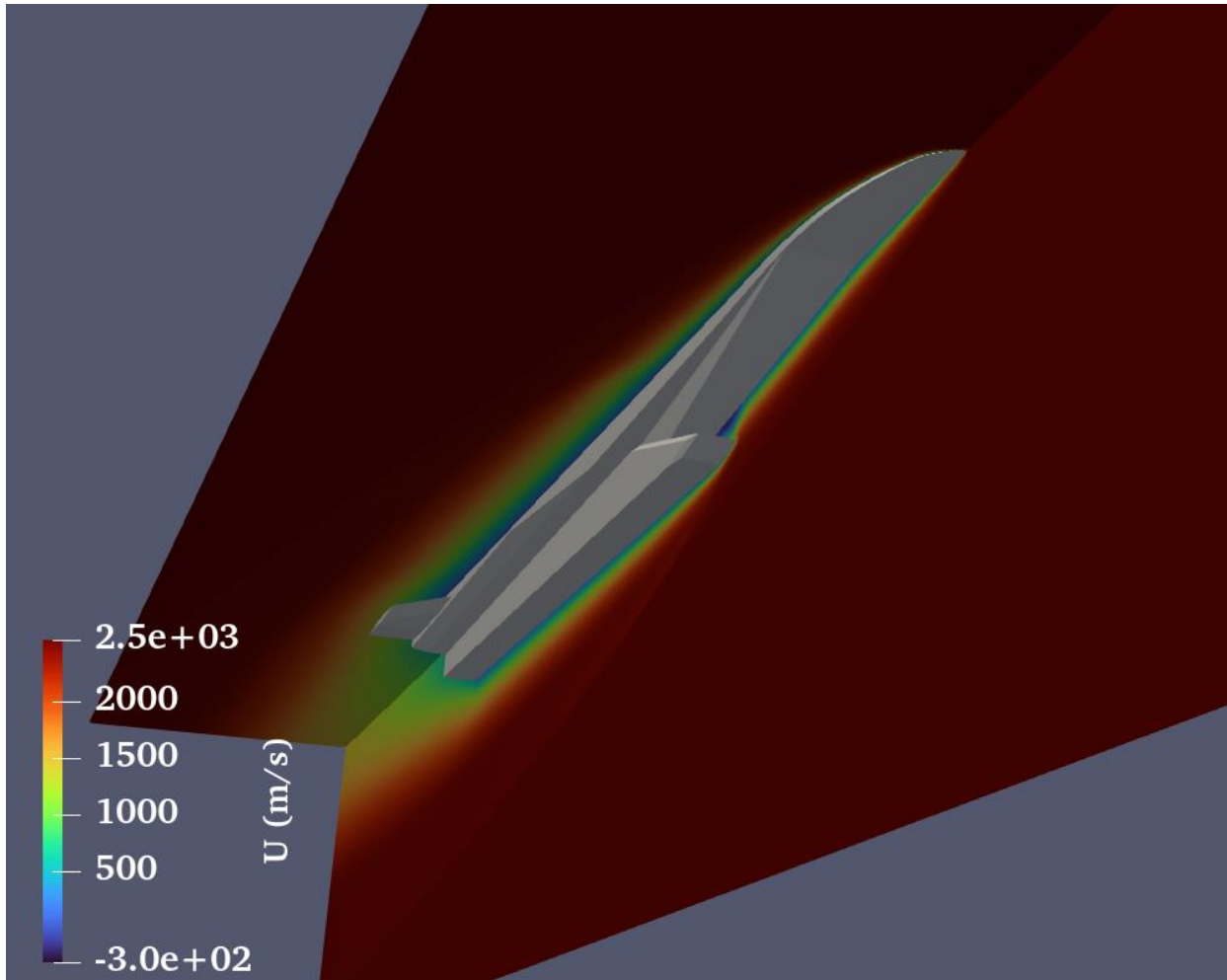
Figure 45: *Streamwise velocity contours at two normal planes.*

As we proceed along the contour plots, the area leading into the scramjet engine's inlet reveals intriguing characteristics. The streamwise velocity experiences a marked decrease, which is essential for the engine's air intake process. Given that scramjets rely on high-speed external flow to compress incoming air, the observed decrease in velocity is instrumental in facilitating the required air mass flow into the combustion chamber with a high pressure. This critical region in general requires a very careful design to assure that the flow characteristics match the engine's operational requirements, while usually a variable geometry of the intake is used, so as to optimize its performance for different flow conditions. The wake behind the vehicle is due to the absence of a real scramjet engine in the simulation. The simulation of the engine's effects requires technical details (exact geometry of the engine, heat rate production, etc.), which are not available and are beyond the scope of this work.

Figures 46 and 47 reveal the temperature contours around the vehicle. Starting from the nose section of the vehicle we see a substantial increase in temperature in front and close to the nose of the vehicle. As seen in the color scale the temperature reaches close to **2,300 K** in front of the nose. This sudden temperature increase occurs due to the fact that the incoming airflow moving at hypersonic speeds, suddenly slows down, leading to an abrupt rise in temperature. A similar observation stands for the intake edge. The colors behind the oblique shocks reveal a transition from cool to warm, while near the vehicle's surface the temperature increase is much more obvious, emphasizing the thermal loads that the materials of the vehicle must withstand. Following the main oblique shock under the nose of the vehicle, we observe another smaller oblique shock wave along the length of the vehicle arising from the engine inlet. These waves represent zones where the air undergoes further compression and heating. They're important for scramjet engine performance because they contribute to the pre-compression of the air before it enters the combustion chamber.
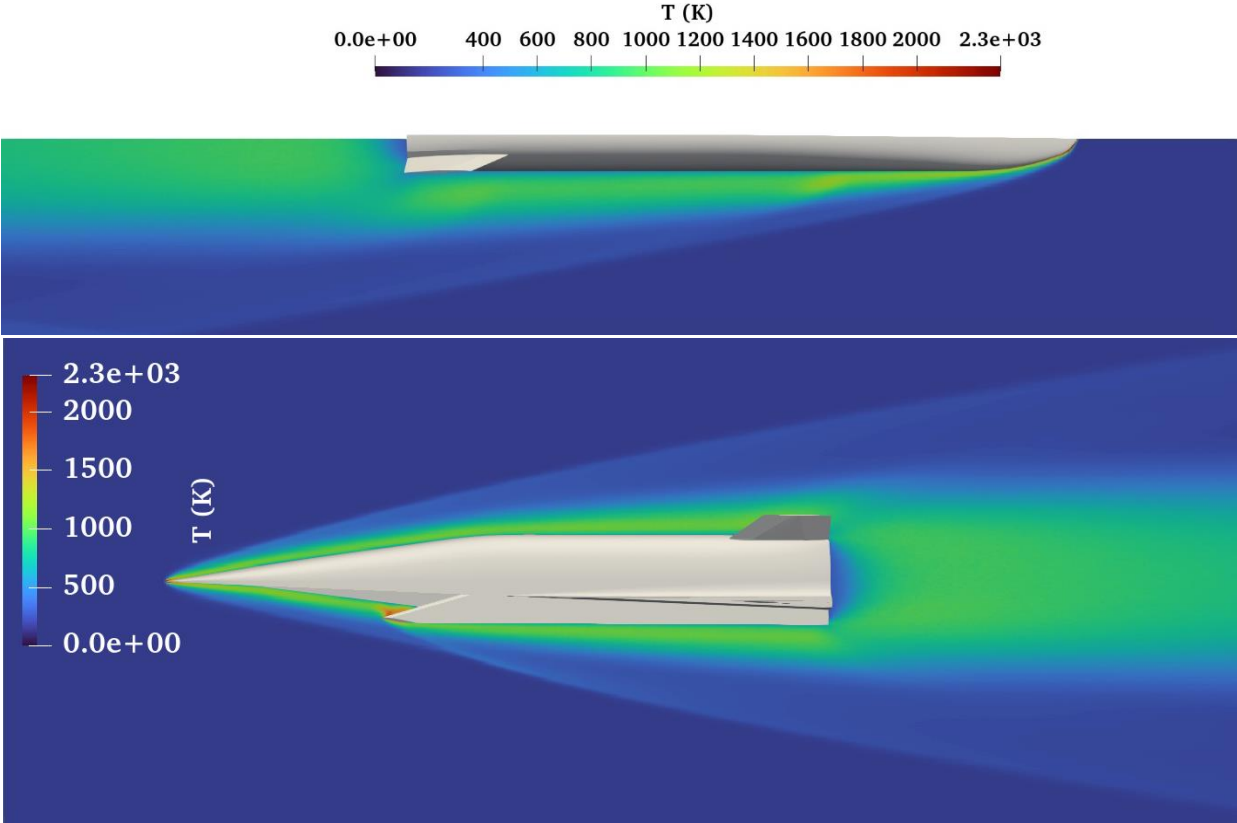
Figure 46: *Flow temperature contours. Top: at the nose level. Bottom: at the symmetry plane.*
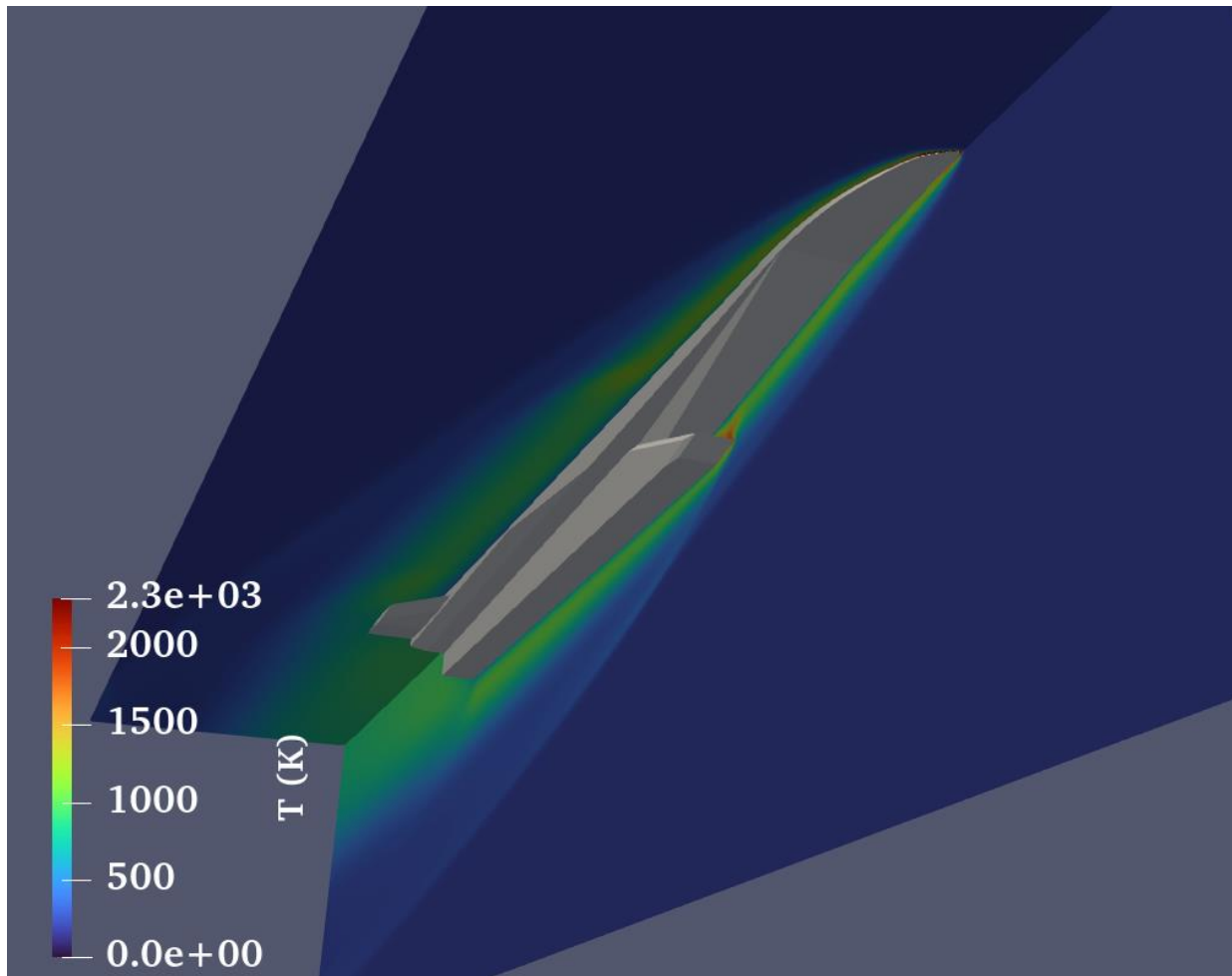
Figure 47: *Flow temperature contours at two normal planes.*

As the flow enters the scramjet engine's inlet, another localized increase in temperature is evident. This is due to the additional compression of air, as it's funneled into the engine, and it's critical because scramjets require high-pressure and high-temperature air for efficient combustion. The warmer hues within the inlet on the figure encapsulate this fundamental aspect of scramjet operation. The combustion chamber would, without a doubt, be the focal point of thermal activity. This is where the fuel is mixed with the compressed, heated air and ignited. The combustion process would significantly raise the air temperature, contributing to the high-velocity exhaust that propels the vehicle at hypersonic speeds. Due to the absence of critical information (exact geometry of the engine, exact heat release rates, etc.) no attempt to simulate the actual combustion was taken in this simulation, as long as the prime interest is in the external flow around the vehicle. Despite this fact as seen in Figure 47 air enters the combustion chamber at a temperature of around **2,000 K**.

Another intriguing feature of Figure 47 is the temperature distribution along the vehicle's surface. At Mach 9, air friction heats up the surface to temperatures that could compromise the structural integrity of the vehicle. More specifically from Figure 47 can be observed that air close to that vehicle's surface reaches a temperature between **1,000** and **1,500 K** (and even higher at the nose region and at the entrance to the engine). This, causes extreme thermal and heat loads to the

structural materials used on the vehicle. Understanding these thermal loads is vital for material selection and structural geometry optimization.

Figures 48 and 49 present the pressure contours around the vehicle. As mentioned before, the flow is compressed behind the nose of the vehicle due to the formation of oblique shocks. Oblique shocks are also formed at the sharp edge of the engine's intake. Observing this area at the engine's intake, we see that the pressure in that area is almost two orders of magnitude larger than the free stream one. The high-pressure in the scramjet inlet is paramount to the scramjet performance. However, the flow field computed inside the engine is only indicative, due to the absence of combustion and the inaccuracy of the geometry.
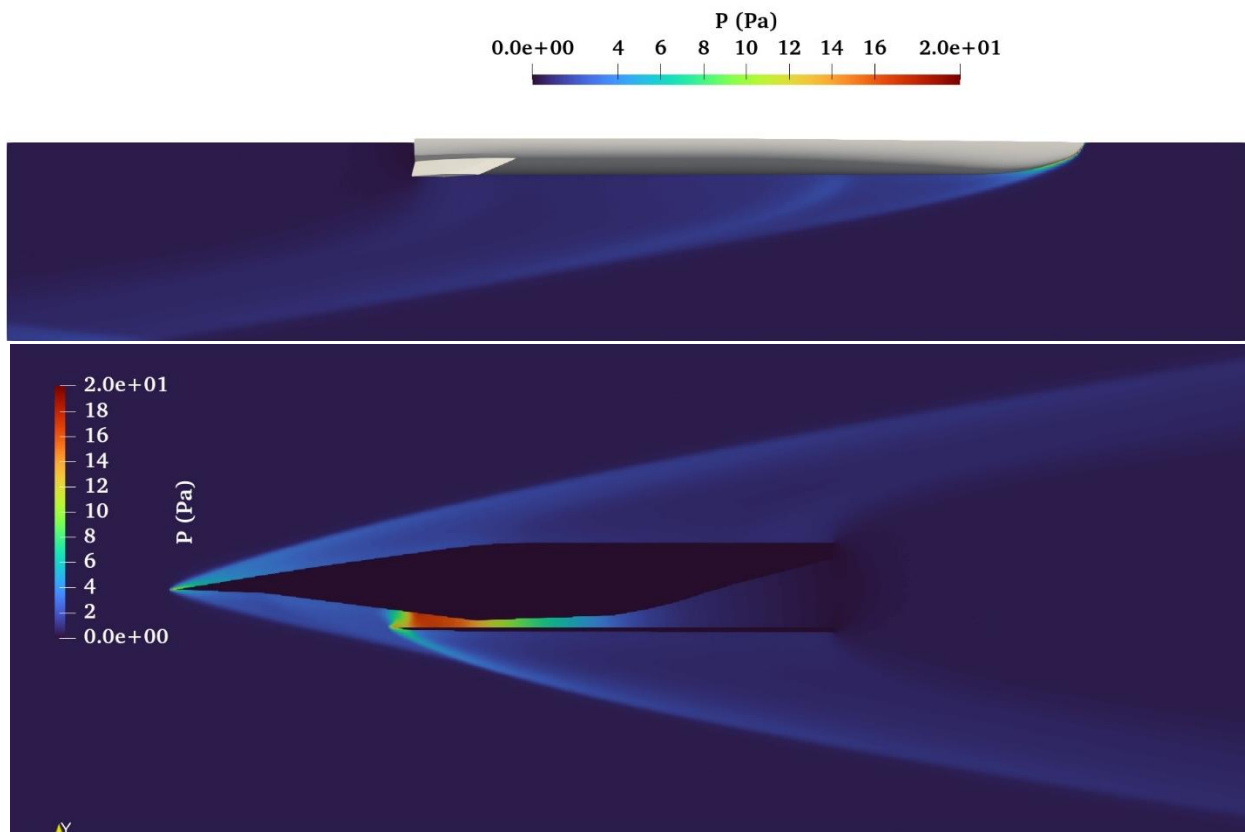

Figure 48: *Pressure contours. Top: at the nose level. Bottom: at the symmetry plane.*
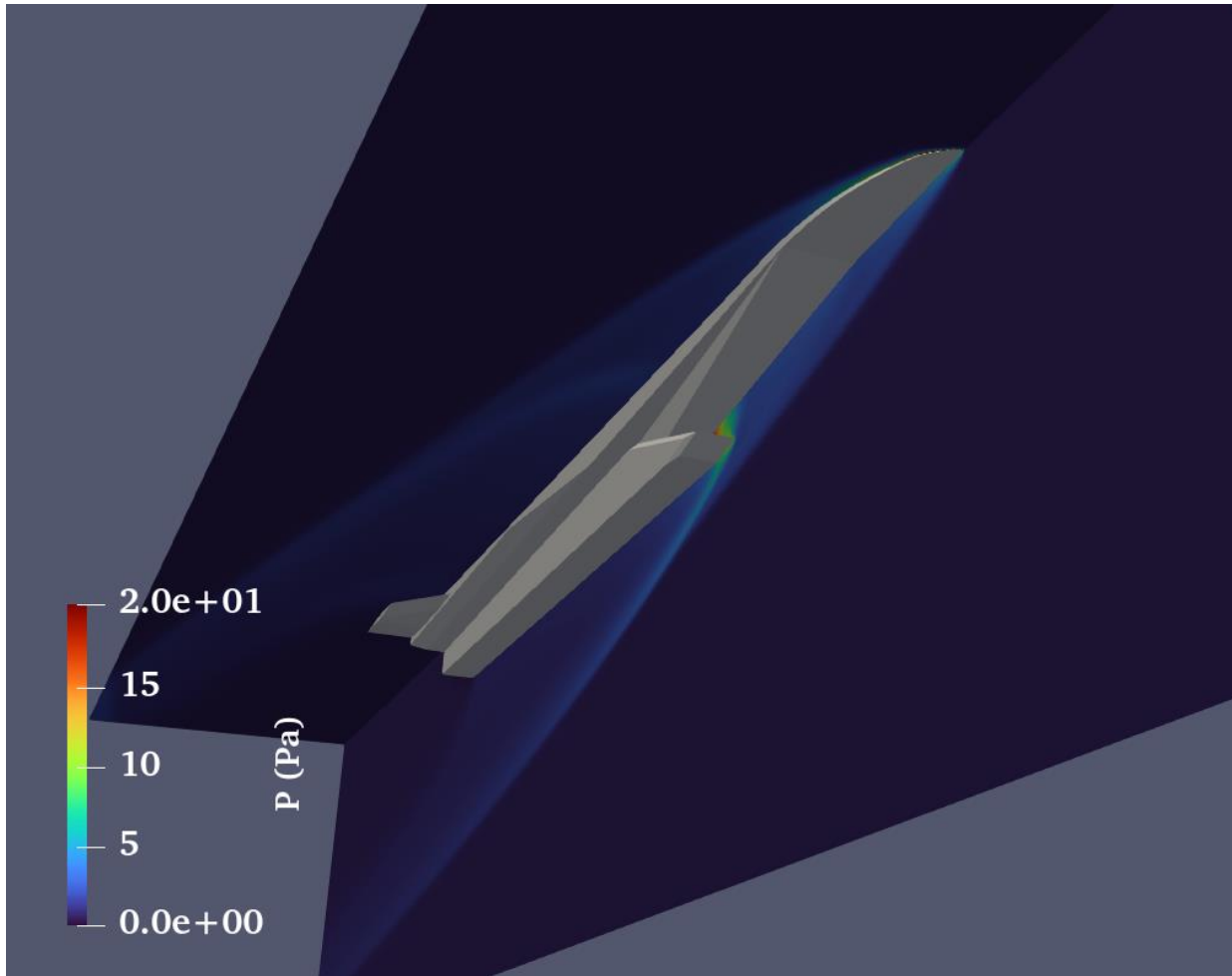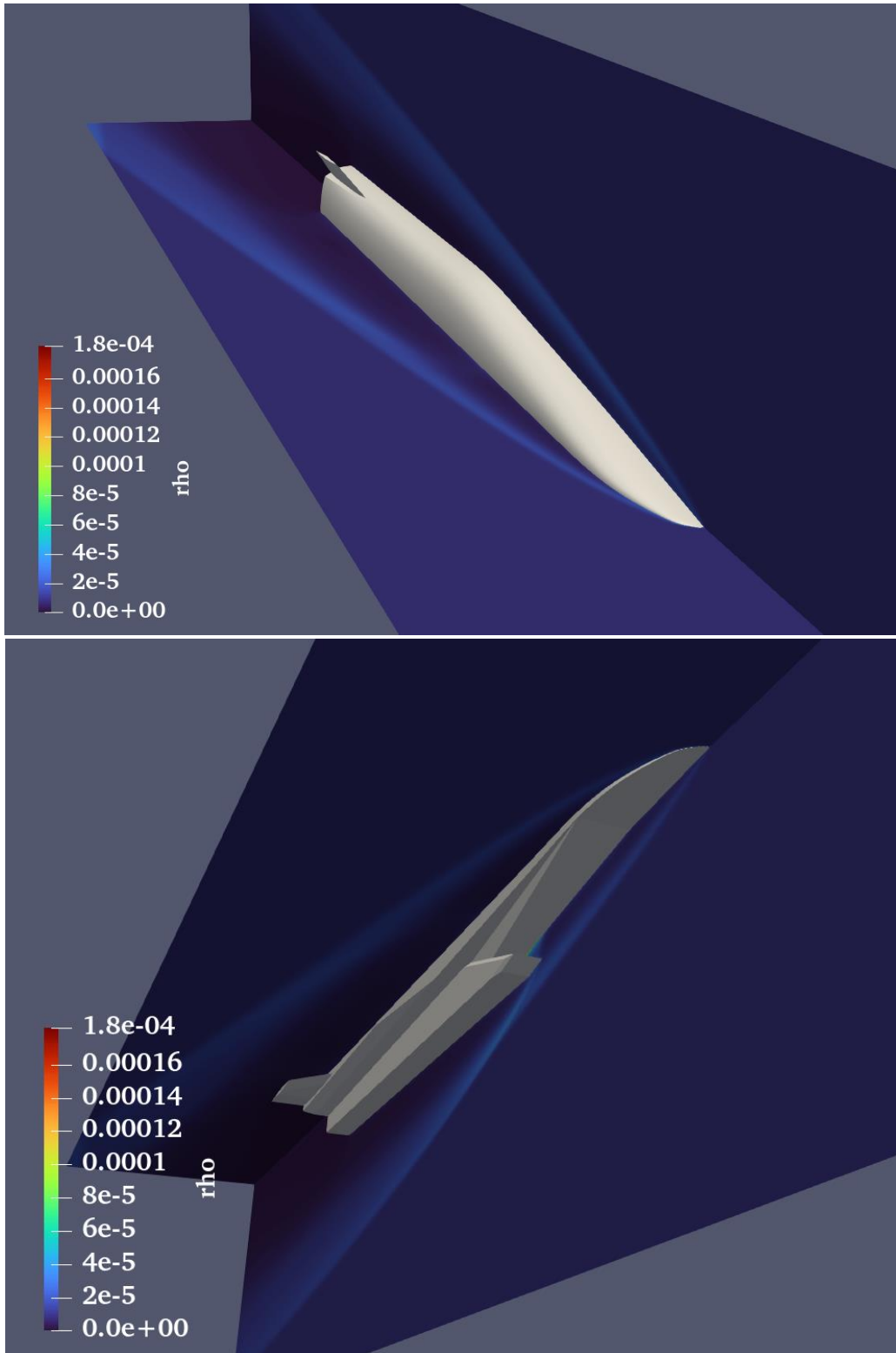
***Figure 49:** Pressure contours at two normal planes.*

Figures 50 and 51 contain the density field. In those figures, apart from the oblique shocks, we can also observe the flow density distribution inside the scramjet engine. Given the high Mach numbers involved, a sudden density gradient is evident right at the engine's entrance, typically following shock-induced compression. Before the flow reaches the combustor, there is a plateau where the density stabilizes. This plateau serves as the region where fuel injection would typically occur (although the actual geometry of this region is not known – neither the exact position of the combustion region). Here, the density contours might show relatively constant values, an ideal condition for efficient mixing and subsequent combustion. In a scramjet engine, the combustion chamber can be considered the "epicenter" of density variations. The burning of fuel not only drastically raises the temperature but also affects the density. As seen in Figure 50, the density inside the "combustor" reaches its peak. Understanding these peaks is crucial for optimizing the engine's combustion efficiency and ensuring structural integrity under high-pressure conditions. Post-combustion, the flow is expanded through the nozzle to convert high-pressure, high-temperature gas into kinetic energy, propelling the vehicle forward. Moreover, in the nozzle the density distribution depicts a rapid density decrease, correlating with the presence of expansion waves and the acceleration of flow again to hypersonic speeds. In this test case most areas of high density coincide with areas of high pressure and temperature, and consequently, higher mechanical and thermal

stresses on engine materials. Nevertheless, the flow simulation inside the engine is only indicative, due to the absence of crucial information.
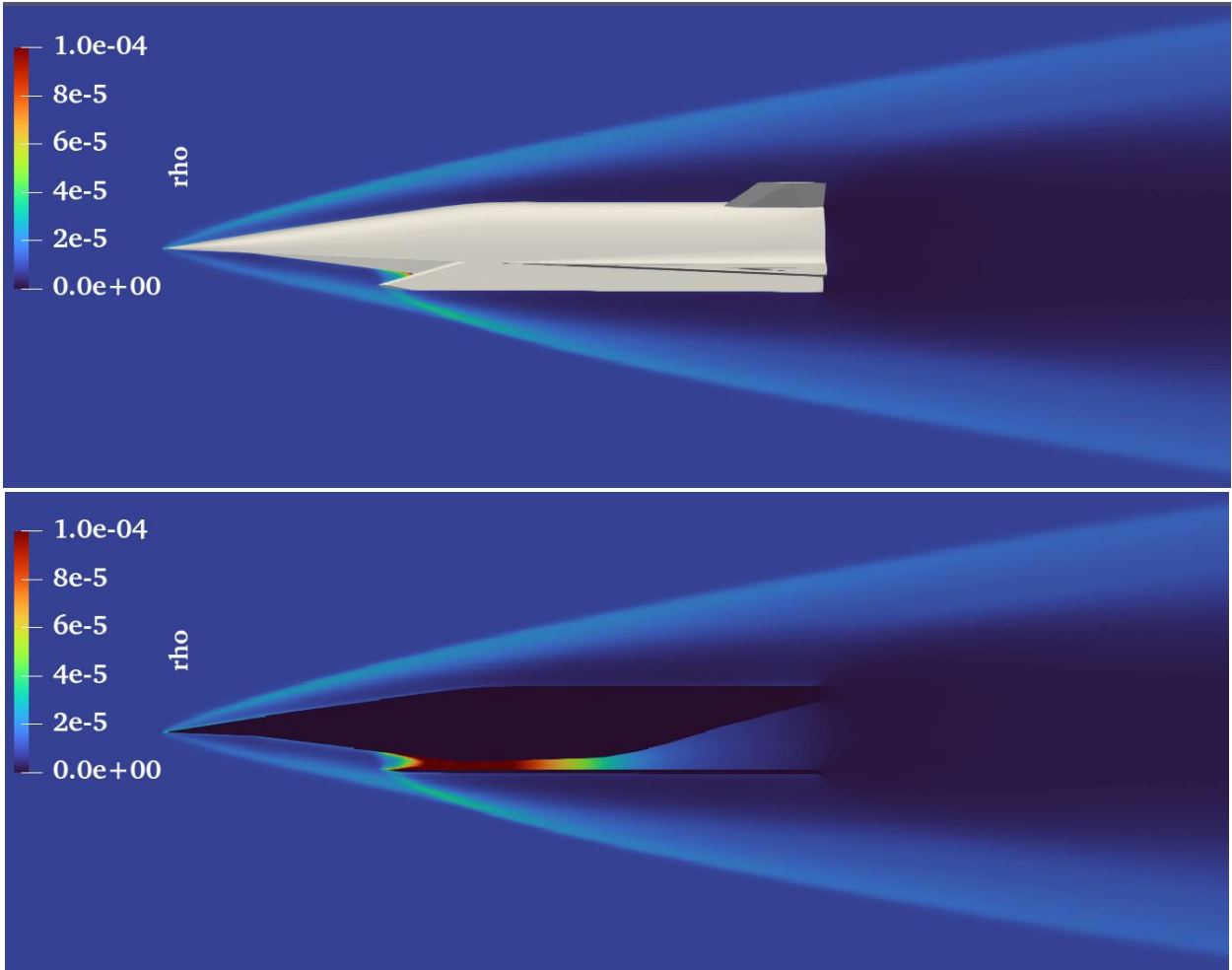

*Figure 50: Flow density contours at the symmetry plane with (top) and without the vehicle's geometry (bottom).*

Figure 51: *Flow density contours at two normal planes.*

The Mach number contours contained in Figures 52 and 53 provide a better insight of the flow field around the vehicle. Figures 52 and 53 also verify that the flow inside the engine remains at supersonic speed, which coincides with the flow requirements of a scramjet. As we move along the vehicle's body, we see a gradual decline in Mach numbers, due to the presence of the various oblique shocks and their interactions with the boundary layers. The Mach number contours at the scramjet engine inlet provide critical information on how effectively the vehicle captures and compresses the incoming air for combustion. In this particular test case the design seems to be effective, because the Mach contours reveal a well-contained, high-speed flow funneled smoothly into the engine. Observing the nozzle section of the engine, the Mach number contours should show an increase as the flow accelerates through the nozzle. This area is critical in the vehicle for converting the thermal energy back into kinetic energy, propelling the vehicle into hypersonic speeds. However, in this simulation, the actual Mach number of the flow inside and downstream the nozzle is not simulated, due to the absence of combustion (following the absence of the geometrical and operational details of the scramjet engine).
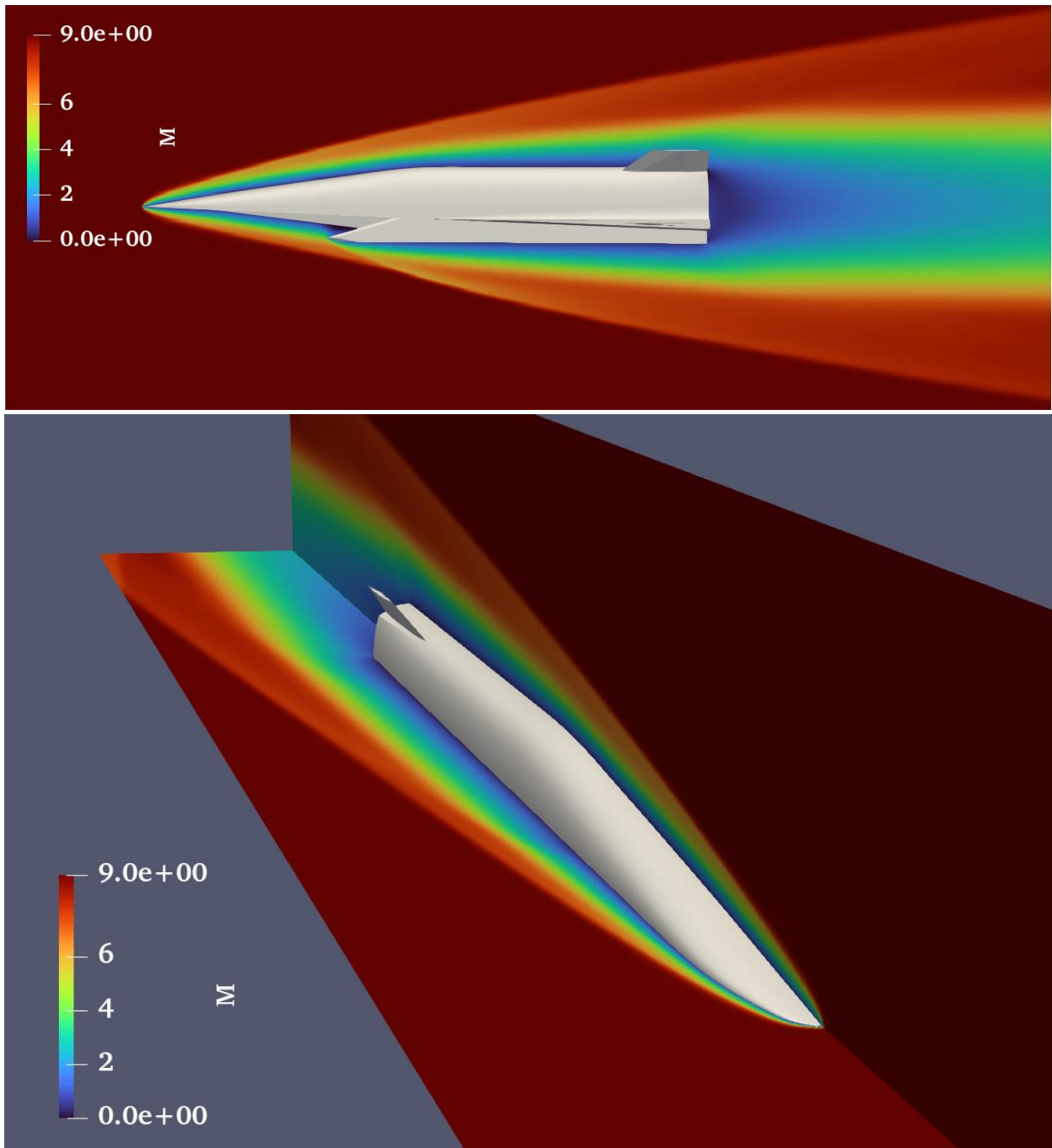
Figure 52: *Mach number contours. Top: at the symmetry plane. Bottom: at two normal planes.*
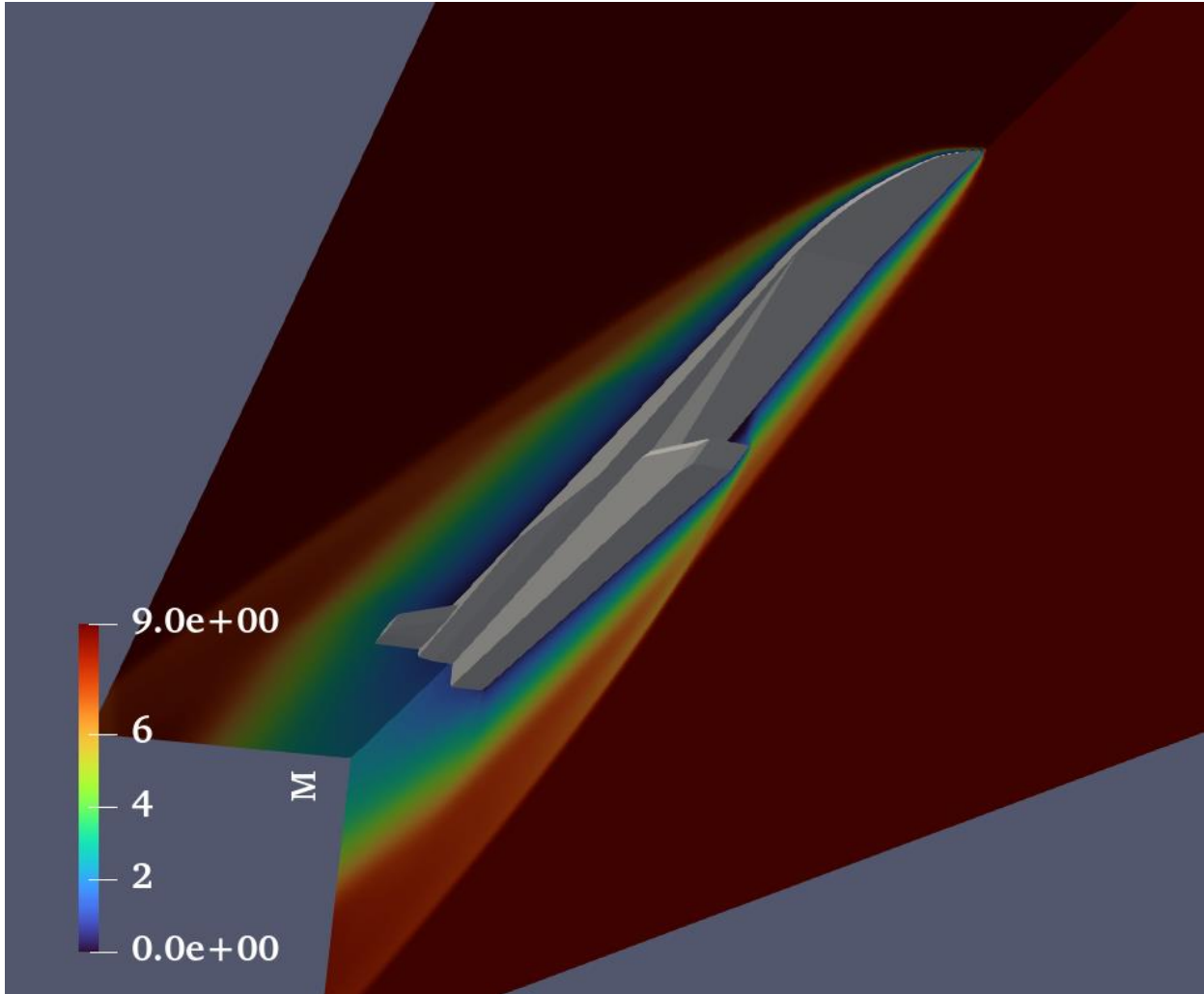
Figure 53: *Mach number contours at two normal planes.*

Figure 54 contains the contours of the Q-criterion. As mentioned before, the Q-criterion is calculated using equation (2) where Ω is the antisymmetric part of the velocity gradient (the vorticity tensor), and S is the symmetric part (the rate of strain). Consequently, positive values of Q-criterion indicate areas in the flowfield where the vorticity dominates the flow, while negative values are indicative of strain rate or viscous stress dominated areas. The Q-criterion serves as an essential diagnostic metric for the flow field around the waverider, visualizing the shock waves and the presence of vortical structures. The position of the oblique shocks is visualized in Figure 54 with the characteristic blue color, while the red color corresponds to vortical structures, starting mainly from geometrical edges.
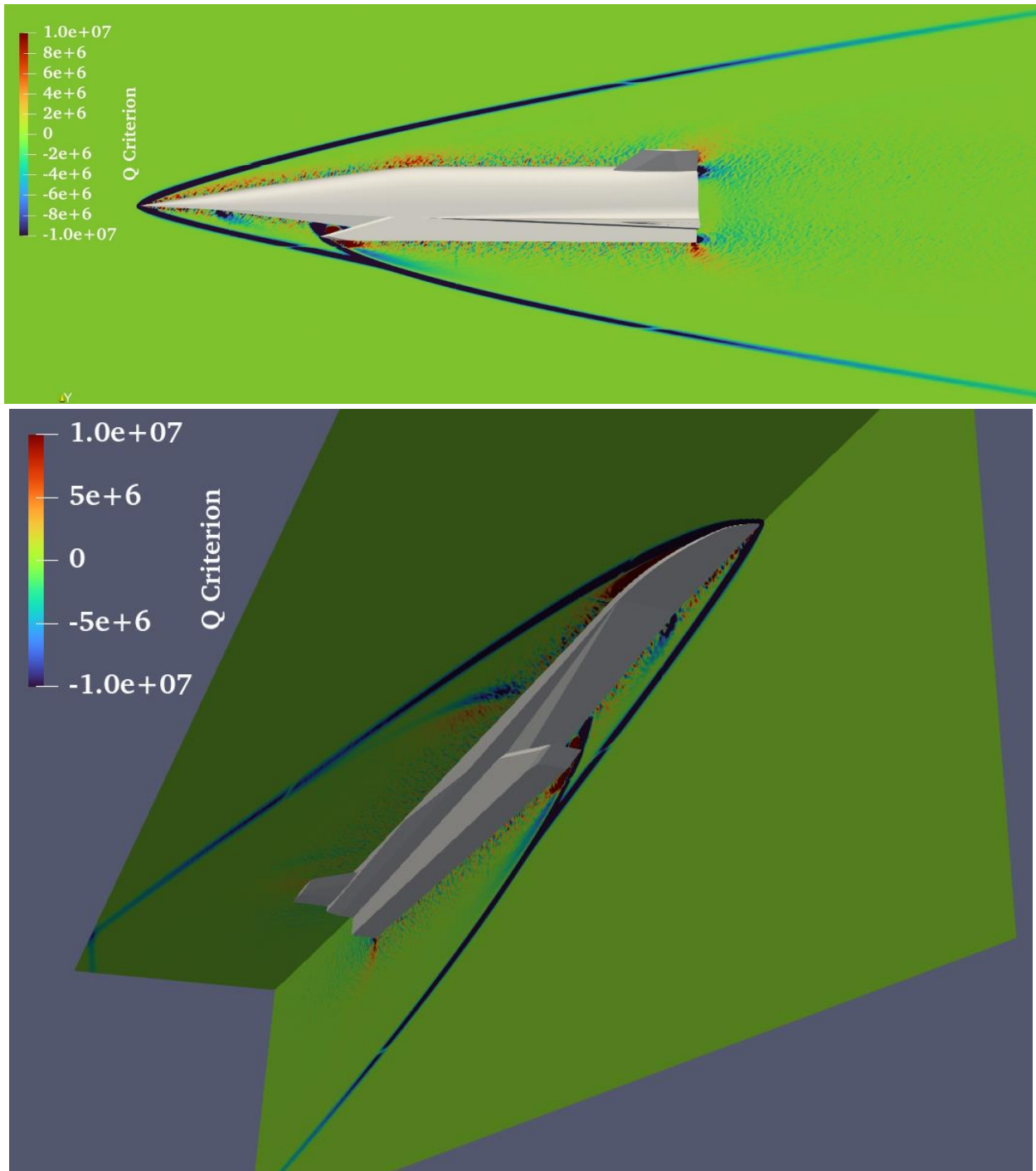
Figure 54: *Q-criterion contours.*

and contain Q-criterion contours at several parallel planes. The blue circular lines reveal the position of the oblique shock, while red regions reveal the position of vortices. It is noticable that the vortices generated at the ramp at the bottom of the vehicle are not entering the engine inlet, due to the effective design of the lower part of the vehicle.
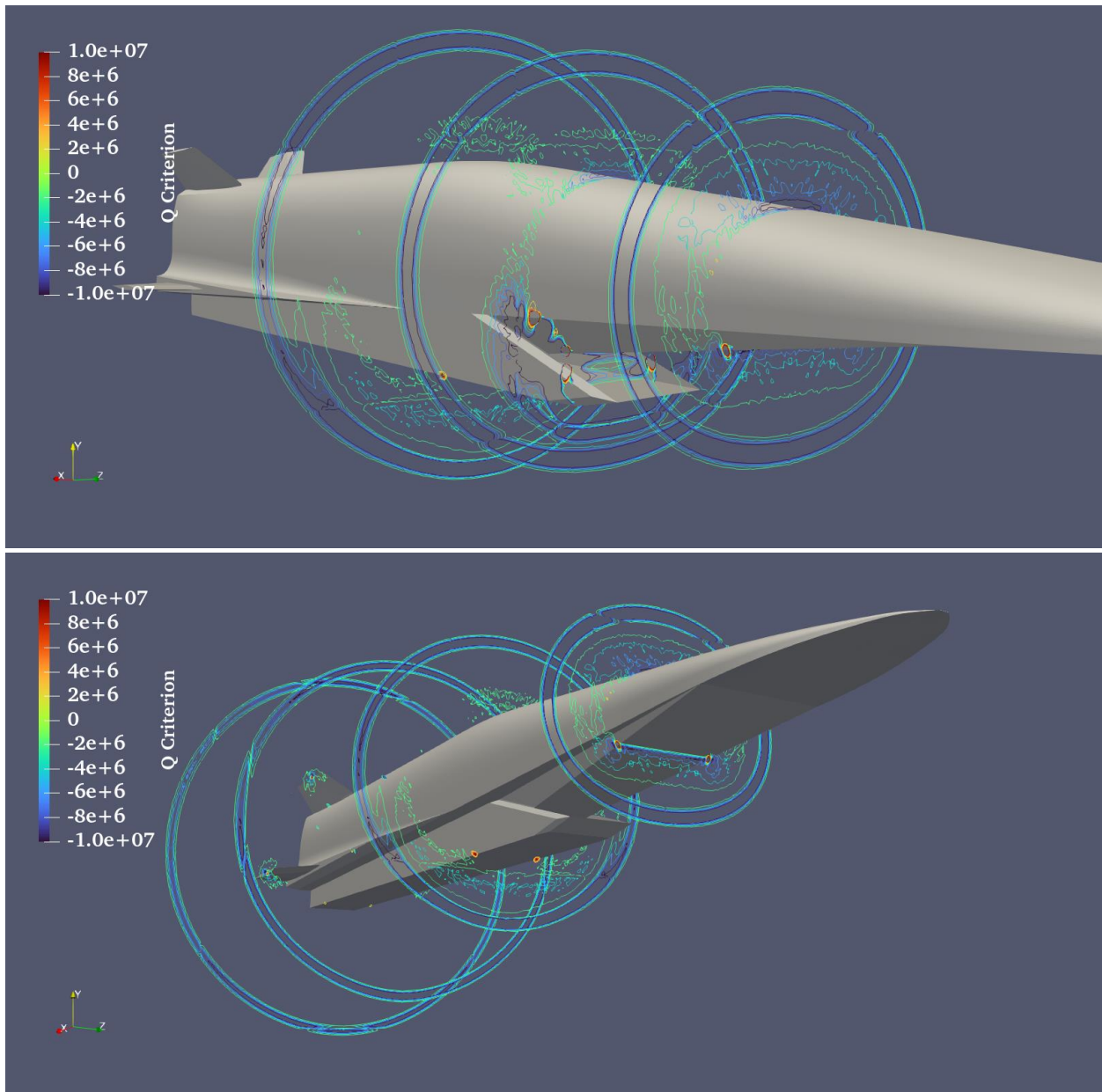
Figure 55: *Q-criterion contours at several parallel planes. The blue circular lines reveal the position of the oblique shock, while red regions reveal the position of vortices. The vortices generated at the ramp at the bottom of the vehicle are not entering the engine inlet, due to the effective design of the lower part of the vehicle.*
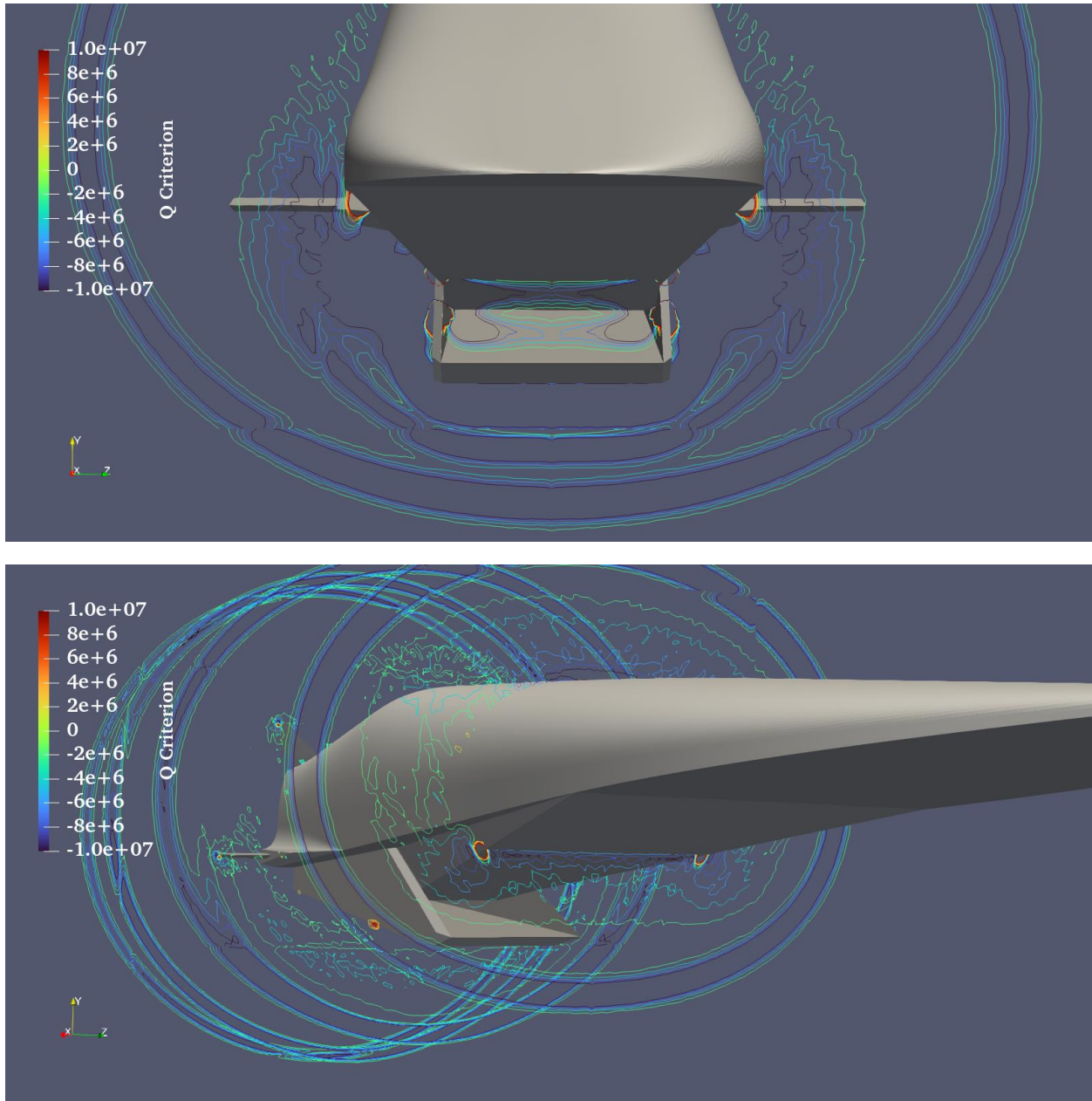
Figure 56: *Q-criterion contours at several parallel planes. The blue circular lines reveal the position of the oblique shock, while red regions reveal the position of vortices. The vortices generated at the ramp at the bottom of the vehicle are not entering the engine inlet, due to the effective design of the lower part of the vehicle.*

Figures 57 and 58 present Q-criterion 3D iso-surfaces around the vehicle. The characteristic green-blue conical structure is the oblique shock. A second oblique shock is formed from the leading edge of the engine's duct. Several vertical structures are emanating from the vehicle's leading edge (red and yellow colors). Another vortex structure is formed at the bottom of the inlet to the engine.
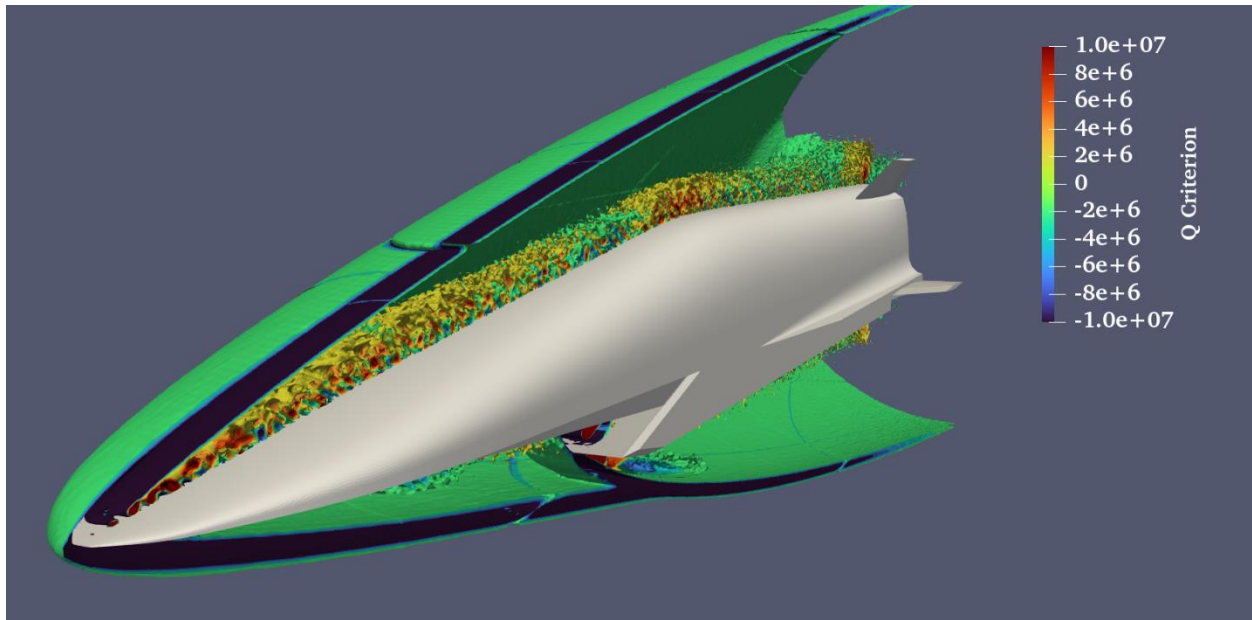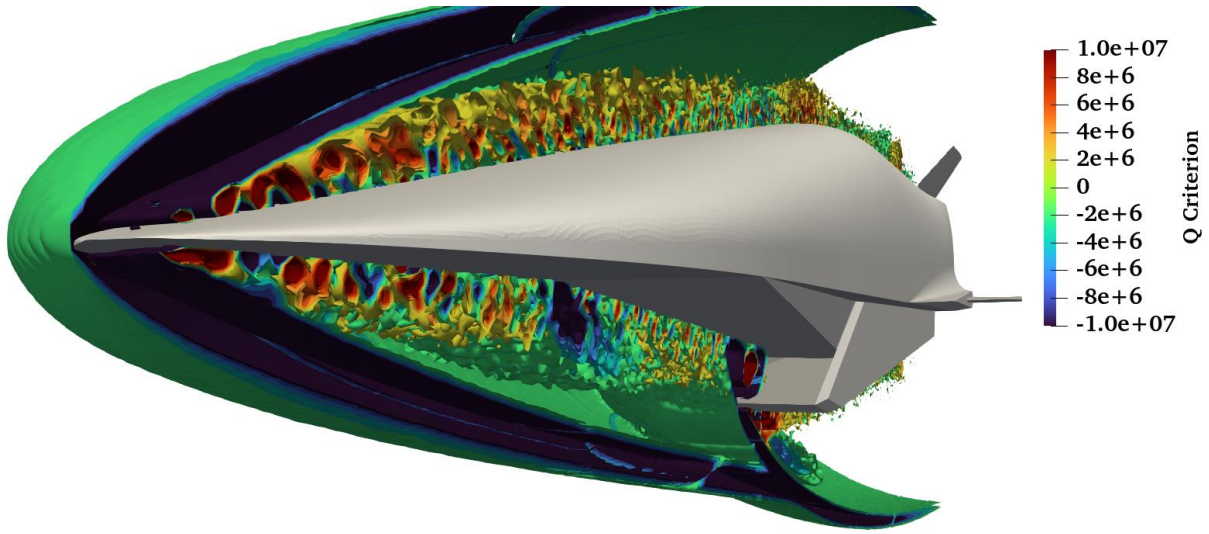
Figure 57: *Q-criterion 3D iso-surfaces around the vehicle. The characteristic green-blue conical structure is the oblique shock. A second oblique shock is formed from the leading edge of the engine's duct. Several vortical structures are emanating from the vehicle's leading edge (red and yellow colors). Another vortex structure is formed at the bottom of the inlet to the engine.*
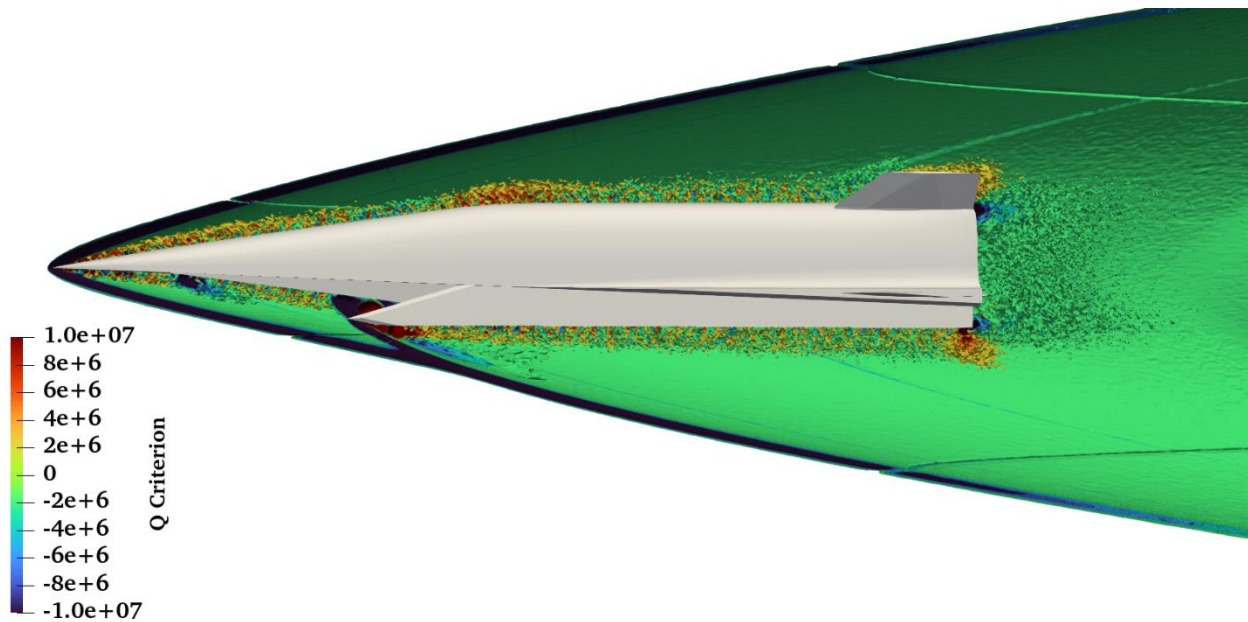
***Figure 58:** Q-criterion 3D iso-surfaces around the vehicle (side view). The characteristic green-blue conical structure is the oblique shock. A second oblique shock is formed from the leading edge of the engine's duct. Several vertical structures are emanating from the vehicle's leading edge (red and yellow colors). Another vortex structure is formed at the bottom of the inlet to the engine.*

Figure 59 contains the contours of the vorticity magnitude. Increased vorticity magnitude is observed at the leading edges of the vehicle and the engine, where high velocity and density gradients exist, due to the geometry characteristics and the existence of the oblique shocks attached to the vehicle' surface at the corresponding positions. This is compatible with the vorticity production demonstrated in the previous Figures, close to the leading edges of the vehicle and the engine inlet.

Summarizing all of the above, the exploration in the domain of hypersonic aerodynamics often necessitates the deep integration of theory and computational modeling. This is exemplified through our extensive simulations, covering a gamut of physical properties such as Mach number contours, pressure distributions, temperature gradients, velocity profiles, and density fluctuations. Each of these data-rich visualizations contributes to a holistic understanding of the intricate and dynamic flow field surrounding our vehicle, soaring at a staggering Mach 9.
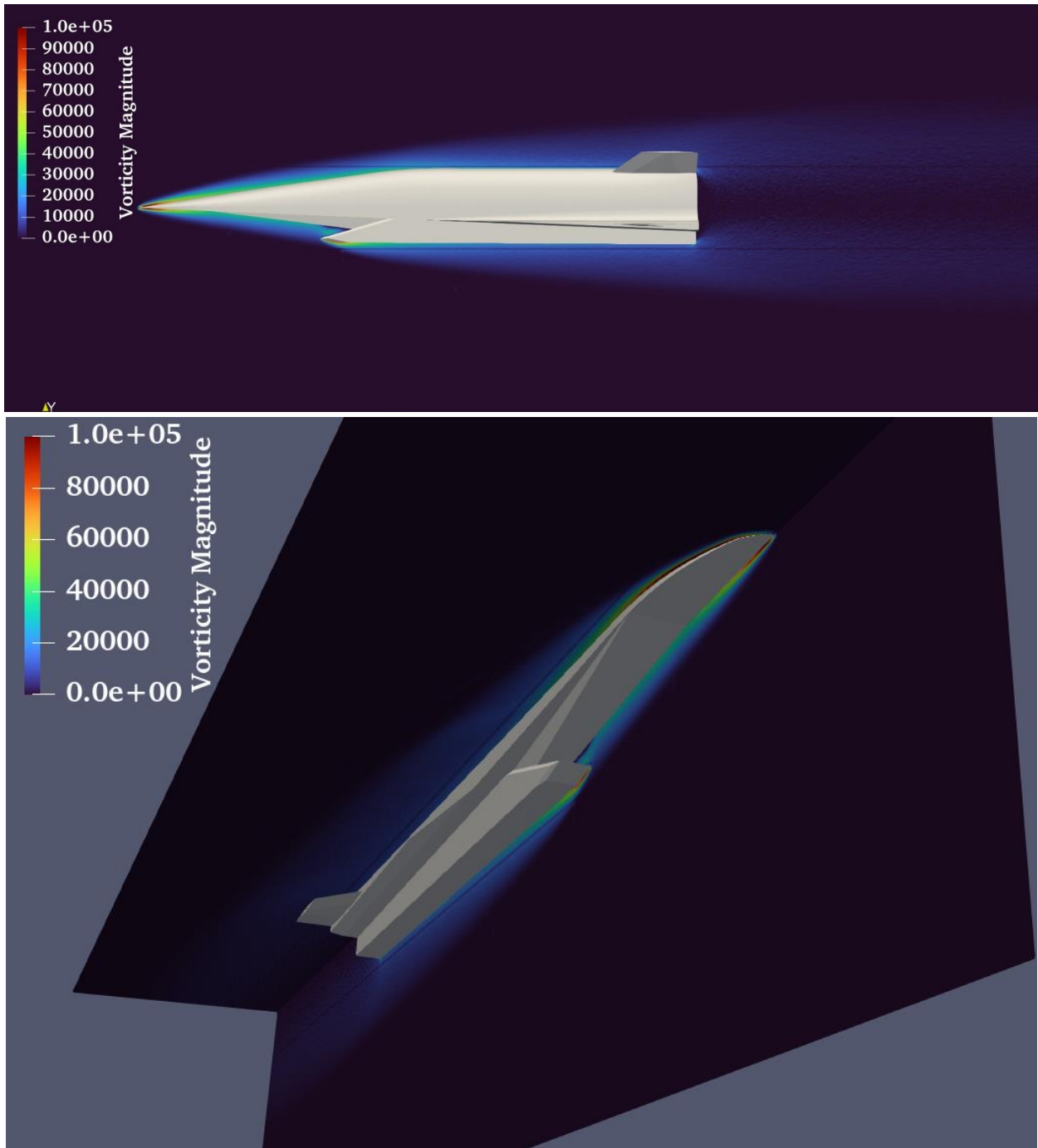
Figure 59: *Vorticity magnitude contours.*

The pressure contours revealed a wealth of information about the local and overall aerodynamic loading on the vehicle's structure. Oblique shock waves, formed at the leading edges of the hypersonic vehicle, indicate the complex shock-boundary layer interactions taking place. These shocks not only serve as a preliminary compressor for the incoming air but also delineate the regions where surface heating and pressure loads are most severe. Pressure distributions are not merely a surface phenomenon; they permeate the entire flow field, impacting the vehicle's drag characteristics

and, by extension, its fuel efficiency. Mach number contours complement the insights gained from pressure distributions. Regions of local flow acceleration and deceleration provide a refined understanding of how the vehicle experiences aerodynamic drag. These contour maps essentially narrate a story of energy transformation, showing how kinetic energy is partially converted into pressure energy and vice versa, especially around the shock structures and in the engine's intake and nozzle regions. The temperature and velocity contours collectively weave a cautionary tale about the thermal management challenges that are part and parcel of hypersonic flight regimes. High-temperature zones often correlate with areas experiencing high shear stress, requiring materials that can withstand both thermal and mechanical loading. These contours further illuminate the non-uniform temperature distribution in the vehicle's aerodynamic body and engine, information that is indispensable for effective thermal management. Though less frequently highlighted, density contours offer significant contributions to this multidimensional analysis. Density variations provide crucial information about the mass flow rates in different regions of the scramjet engine, indirectly affecting combustion efficiency.

These simulations gain their rigor and reliability from the DSMC method, a computational technique well-suited for simulating rarefied gas flows and complex molecular interactions, both of which are ubiquitous in hypersonic regimes. DSMC's stochastic, particle-based nature allows for a high-fidelity representation of the microscopic phenomena that ultimately govern macroscopic flow behavior. Given the level of detail achieved, DSMC serves as more than just a computational tool; it is a cornerstone that lends credibility to our entire investigation.

In conclusion, our ensemble of contour plots should be seen as interdependent pieces of a larger puzzle, each offering unique insights but achieving their true potential when viewed as a cohesive whole. The marriage of high-fidelity DSMC simulations with our multi-physical portrayal of hypersonic flow allows us to navigate the complexities of a domain notorious for its non-linearities and high gradients. With the roadmap clearly laid out and the computational and theoretical tools at our disposal continually evolving, we stand on the cusp of significant advancements in hypersonic technology. It is this cyclical and symbiotic relationship between computational innovation and engineering application that promises to fuel the next generation of breakthroughs in this fast-evolving field.

Looking ahead, there is considerable room for expansion and refinement of the work presented in this Report-2. The next steps will involve the exploitation of the current numerical results for both studied hypersonic vehicles, so as to highlight specific flow characteristics and phenomena and gain further insight to the hypersonic flight, especially in terms of their footprint (flow and thermal characteristics that can be utilized for early warning purposes). Moreover, the simulation of the flow for alternative flow conditions will be performed for both cases, in order to gain a broader view on their performance, flight characteristics and the relative flow phenomena (that might be used later in order to construct flight simulation models). Additionally, classical CFD simulation tools (which solve the Reynolds-Averaged Navier-Stokes equations – RANS), will be also utilized, to simulate the flow field around the scramjet-powered hypersonic vehicle in lower altitudes and provide supplementary insights to the related flow phenomena.

# 6. Evaluation of the waverider design at 45 km altitude and 0 deg. AoA.

In this section, the simulation of the flow around the waverider design at 45 km altitude and 0 degrees angle-of-attack (AoA) will be presented. Such a lower altitude is more representative of the actual flow conditions of such vehicles. However, at a lower altitude the air density is higher, and this poses a computational burden to the DSMC method; it requires much higher computational resources, which are beyond the ability of the working team. Therefore, for the simulation of the flow around the waverider vehicle at 45 km altitude, a special formulation of the Navier-Stokes equations has been used, as implemented in the open source CFD code SU2. The flow condition that have been simulated are included in Table 4.

Table 4: Flow conditions used for the simulation of the waverider (US Standard Atmosphere mode, Altitude 45km).

|	
Mach	*6.2*
Pressure, p_∞ [Pa]	*150*
Temperature, T_∞ [K]	*265.05*
Reynolds	*3,285,710*
Gas	*Air, 5-species*

An unstructured grid was constructed around the vehicle, inside a rectangular flow domain, as depicted in Figure 60. Higher grid density was used around the vehicle, while prismatic inflation layers were added at the surface of the vehicle, to account for the steep velocity and temperature gradients, taking place inside the corresponding boundary layers, attached to the solid boundary (Figure 61). A very dense surface grid was constructed on the solid surface of the vehicle, to allow for a detailed description of the geometry and the accurate simulation of the related flow phenomena. The unstructured (hybrid) computational grid consists of **54,484,085 elements** and **15,732,524 nodes**.

Although the solution of the Navier-Stokes equations requires less computational resources, compared to the DSMC method, it is not without serious difficulties. The solution of the corresponding extended Navier–Stokes equations (to accommodate reacting flows in thermochemical non-equilibrium conditions at high Mach number flows) is very challenging; these equations represent a complex system of interconnected nonlinear partial differential equations (PDEs), and their iterative solution may present many convergence problems. Therefore, several trials may be required to achieve a converged solution.
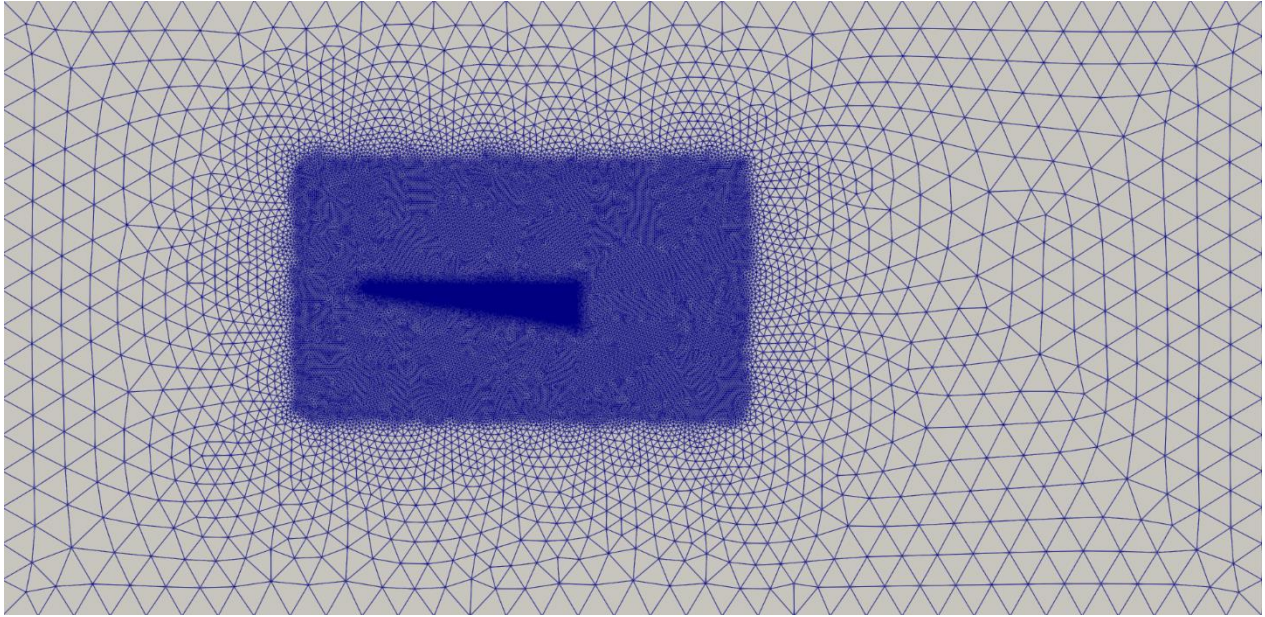
Figure 60: Computational grid overview, utilized for the CFD simulation of the waverider geometry.
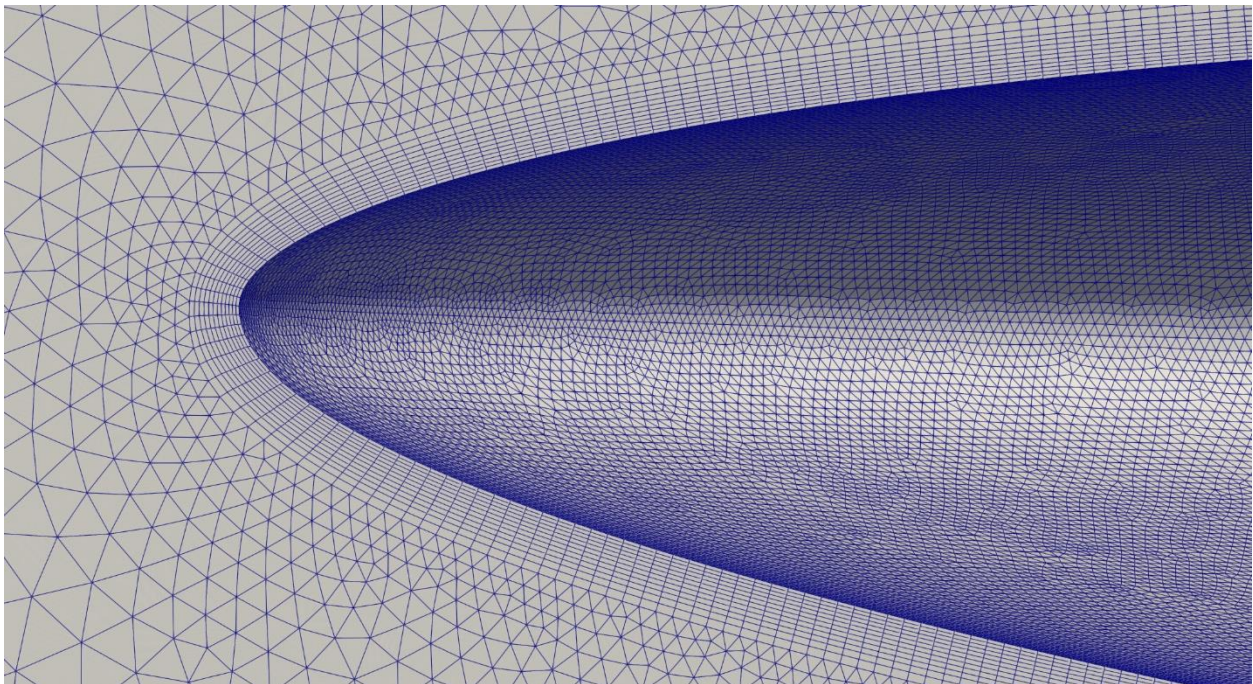

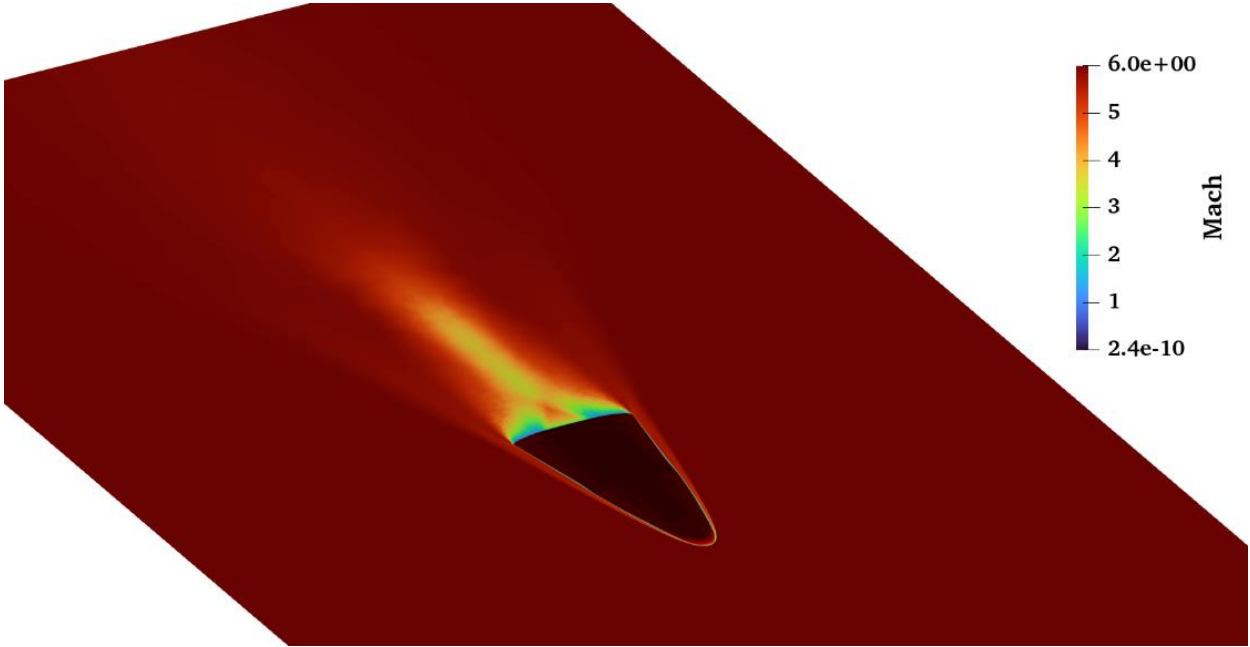*Figure 61: Computational grid zoom-in (utilized for the CFD simulation of the waverider geometry).*

The following results correspond to 0 angle-of-attack. Figure 62 presents the Mach number contours at the symmetry plane of the waverider vehicle. The shock formations around the vehicle and the very intensive wake behind the vehicle are evident. The Mach number contours at a plane parallel to

the vehicle are presented in Figure 63. The detached oblique shock around the leading edge of the vehicle can be observed, as well as the wake behind the vehicle.

Figure 64 contains the velocity magnitude at the symmetry plane, while Figure 65 contains the same contours, but close to the nose of the vehicle, to clearly demonstrate the formation and the position of the corresponding shock. Attached to the solid surface, a relatively thin velocity boundary layer is formed, as it is visualized by the blue-yellow colors of the corresponding contours.
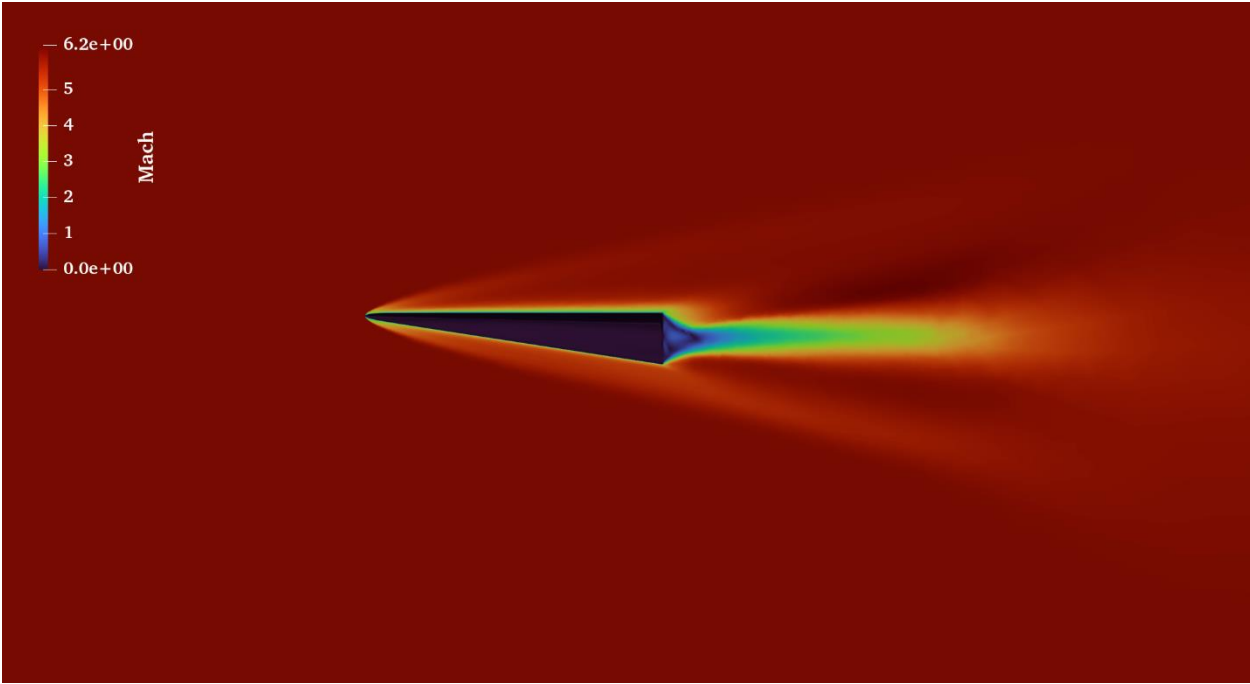
Figure 62: *Mach number at the symmetry plane (0.0 AoA).*
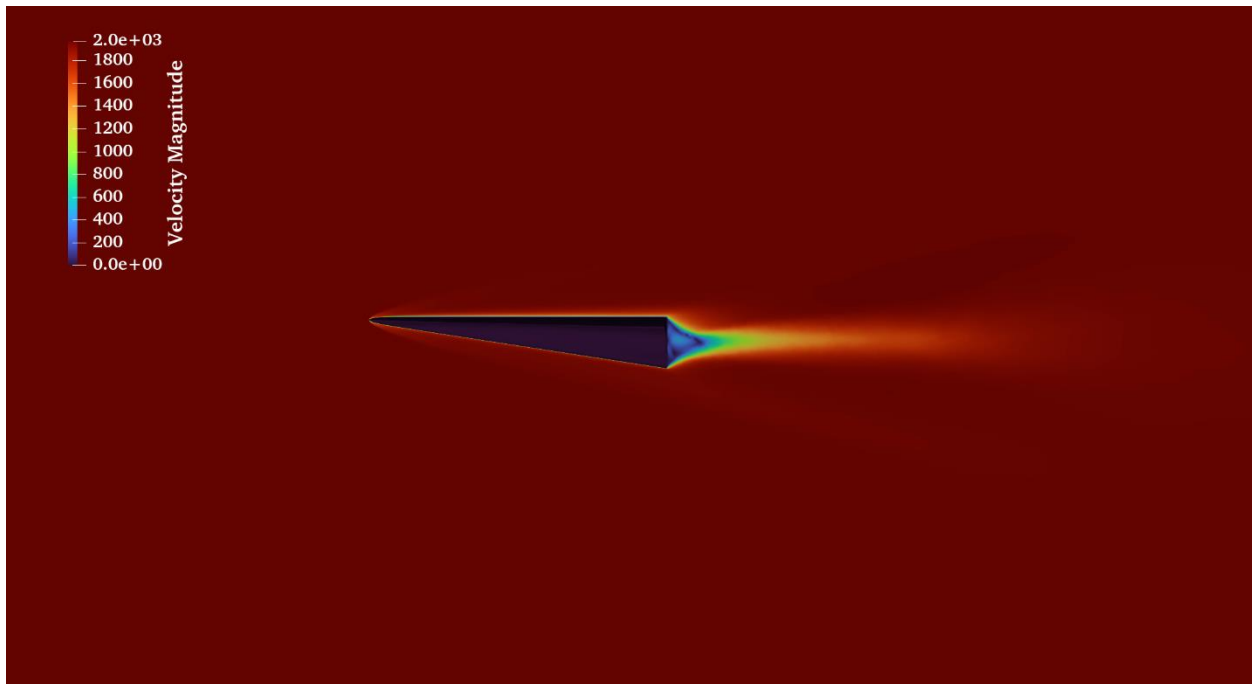
Figure 64: Velocity magnitude at the symmetry plane (0.0 AoA).
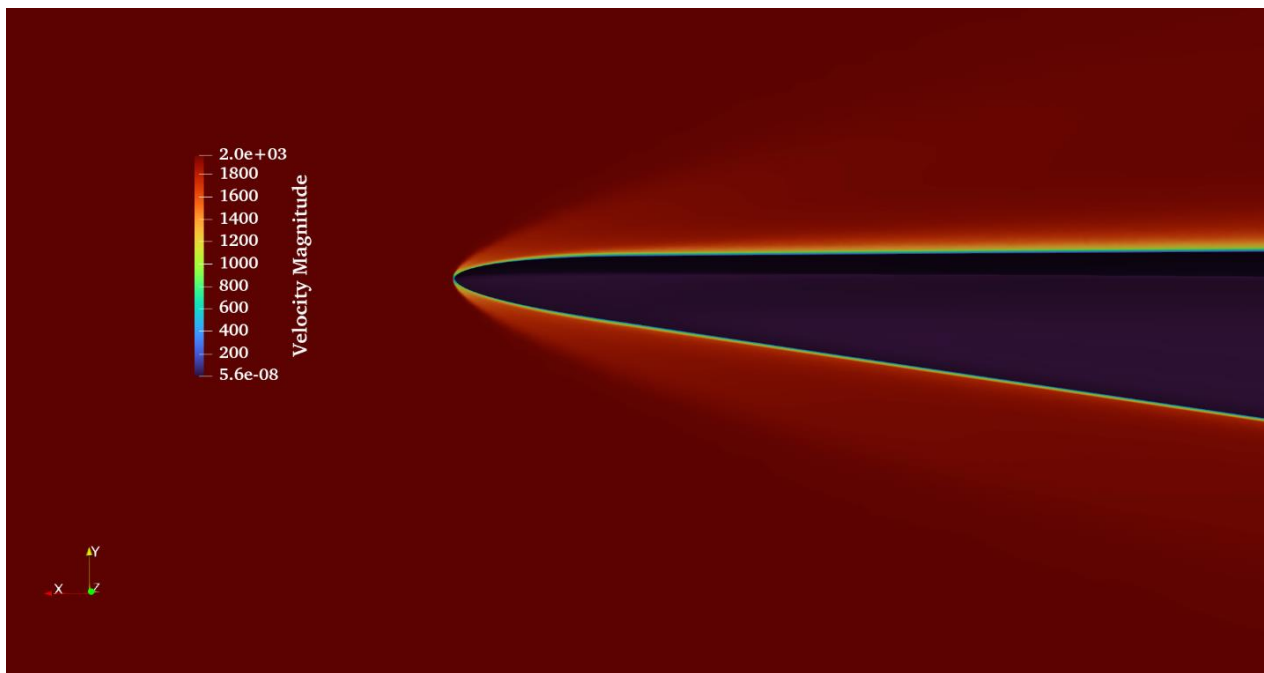
Figure 65: Overview of velocity magnitude around the nose region (0.0 AoA).

Figure 66 contains the contours of Q-criterion at the symmetry plane of the waverider vehicle. Positive values correspond to vertical structures, while negative values correspond to shock-waves. Figure 67 contains the contours of Q-criterion at various planes normal to the symmetry plane of the

vehicle, while Figure 68 contains the corresponding Q-criterion contours at the transverse plane 1.6 meters downstream the nose of the vehicle. A detached conical shock wave is evident around the vehicle, while attached shocks are observed at the leading edges and at the bottom of the vehicle's fuselage.

Figure 69 contains the contours of static pressure at various planes normal to the symmetry plane of the vehicle. A high-pressure region is observed at the lower surface of the vehicle, with a higher pressure observed at the upper surface. However, the pressure difference between the lower and upper surfaces of the vehicle is not high, due to the zero angle-of-attack of the vehicle. This will subsequently result in low lift-to-drag ratio equal to ≈ 0.99, demonstrating that a higher angle-of-attack is required for this lower altitude to support the gliding of the vehicle. This was expected due to the fact that the vehicle has been designed for an altitude of 90 km.

Figure 70 depicts the contours of vorticity component along x-axis, at a plane at the back of the vehicle. It can be observed that the vorticity production is much larger at the leading edges of the vehicle and at the lower surface of the fuselage, where attached shock waves are formed.

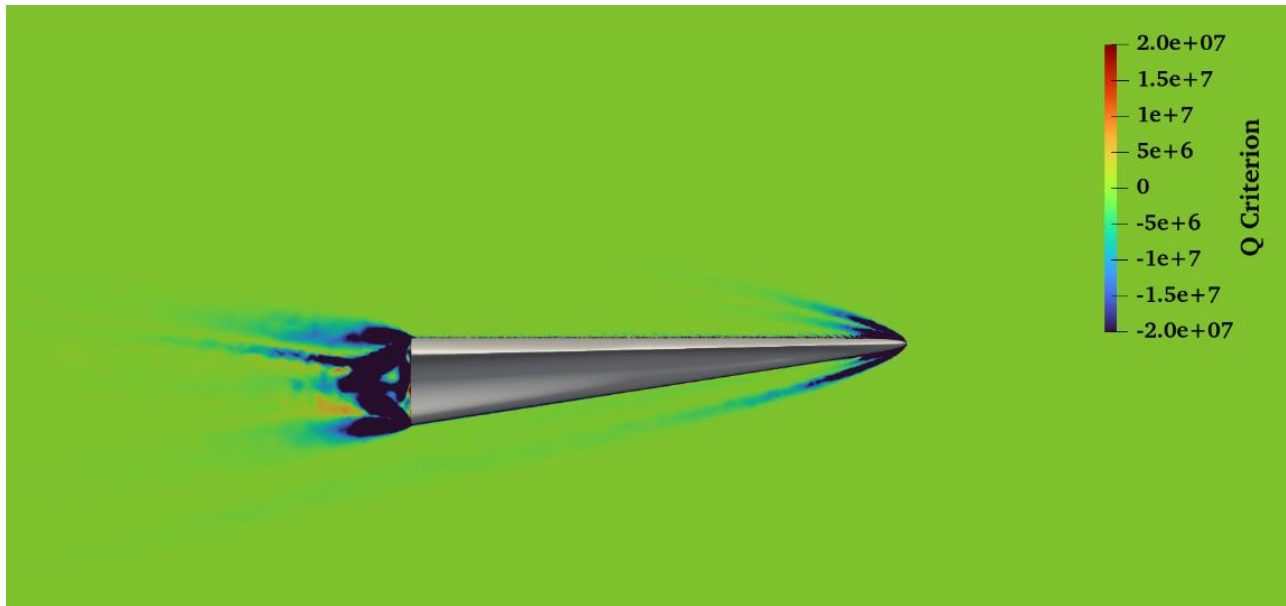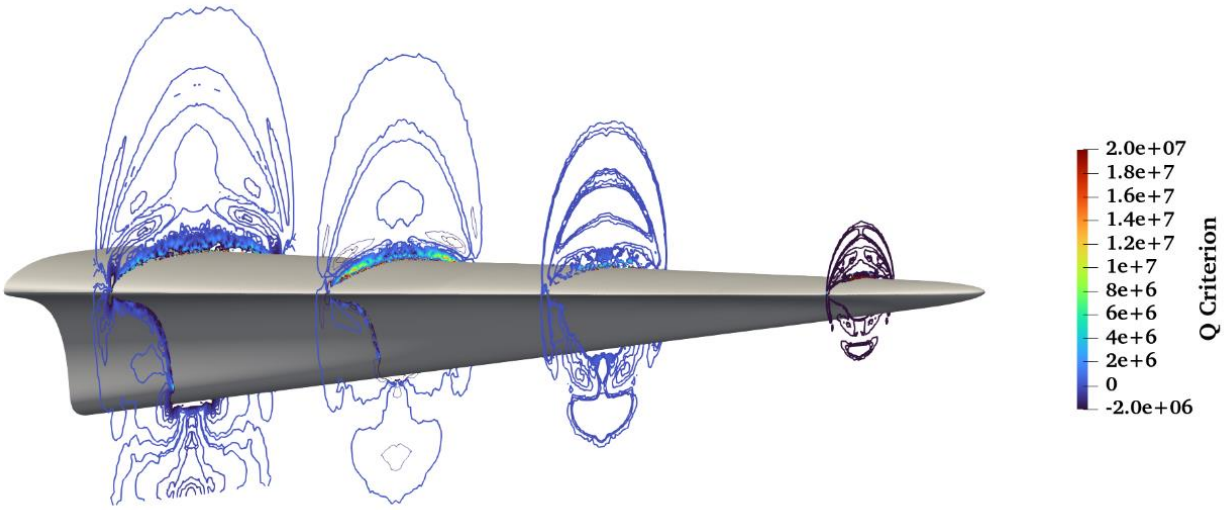***Figure 66:*** *Q-criterion at the symmetry plane (0.0 AoA).*

Figure 67: *Q-criterion contours around the vehicle (0.0 AoA).*
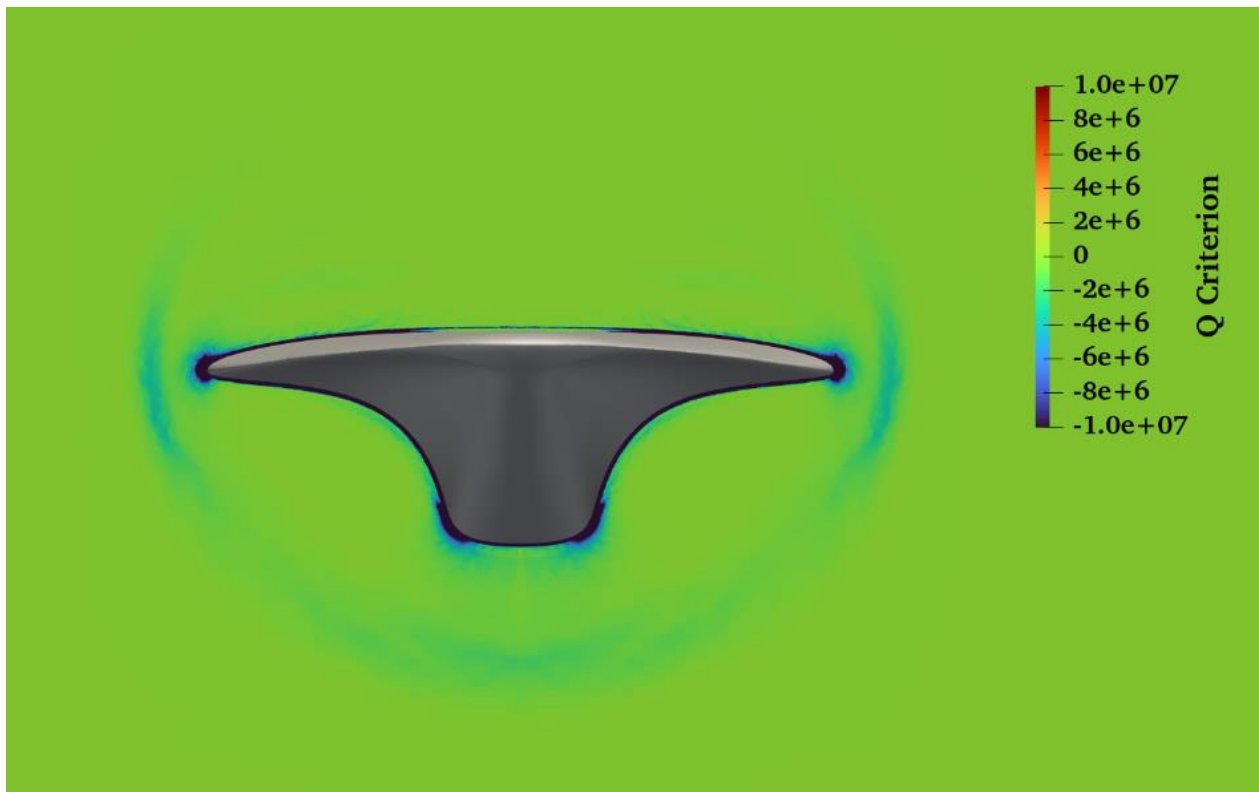
Figure 68: *Q-criterion at 1.6 meters downstream the nose of the vehicle (0.0 AoA).*
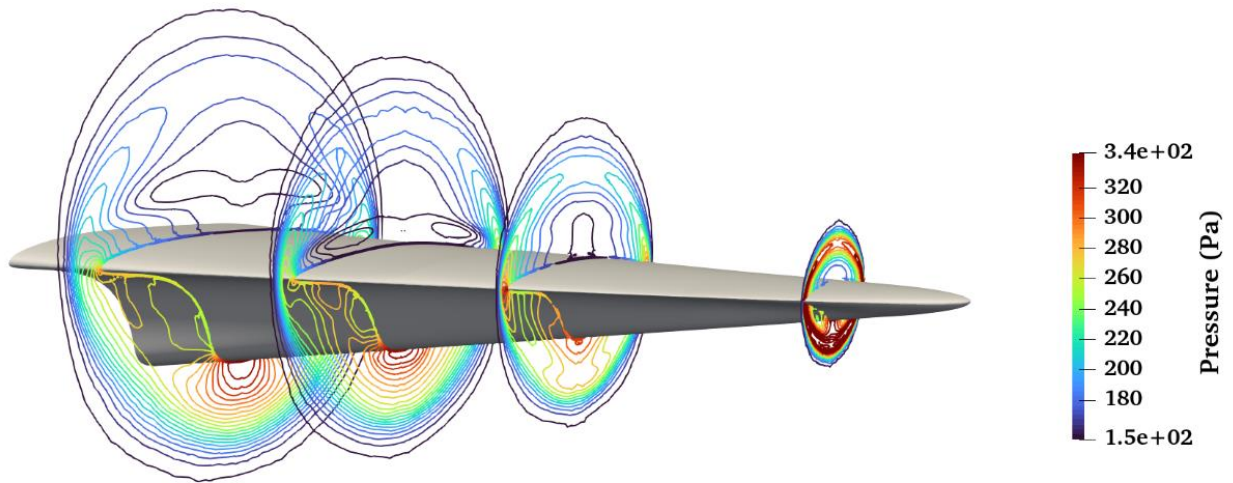
Figure 69: *Pressure contours around the vehicle (0.0 AoA).*
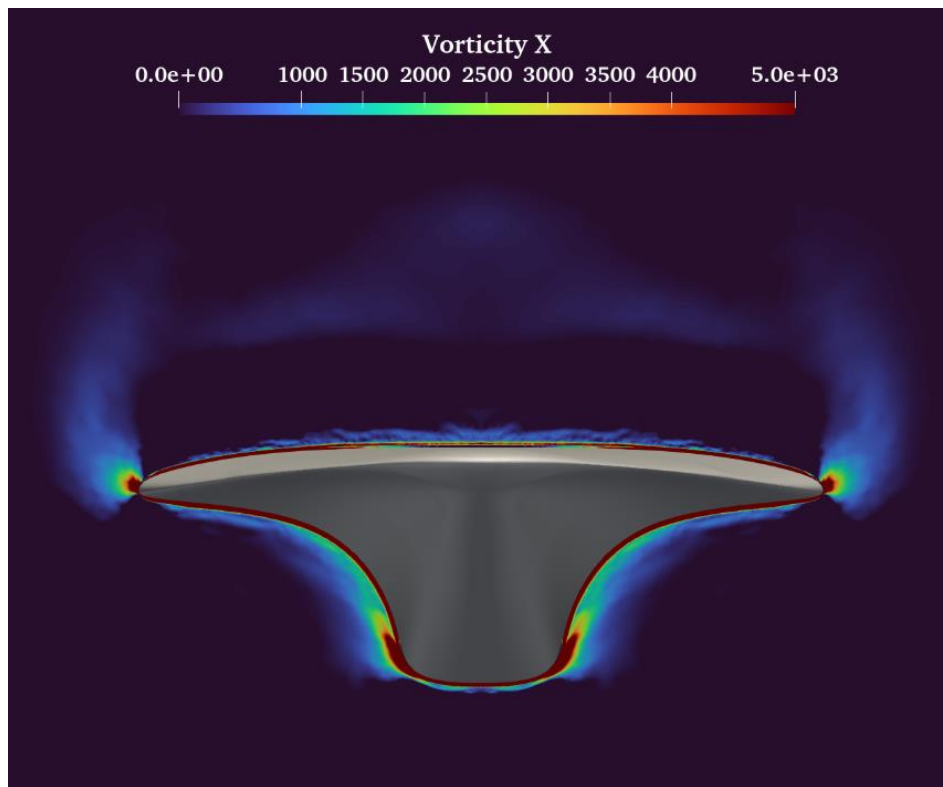
Figure 70: *Vorticity along x-axis at a plane at the back of the vehicle (0.0 AoA).*

Figure 71 contains the contours of Temperature at the symmetry plane of the vehicle. High temperature is evident at the leading edge of the vehicle, as it can be expected, but also inside the wake behind the vehicle. This observation is very interesting, as the wake behind the vehicle

enhances the temperature footprint of the waverider in hypersonic flights. This observation will be also supported in the results of the following Figures.

Figure 72 contains the contours of Temperature at four different planes around the vehicle; the surface of the vehicle is colored by heat flux. The heat flux is higher along the leading edges of the vehicle (as expected), which poses serious problems to the materials and to the heat management system of the vehicle. Figure 73 contains a thermal image of the temperature around the vehicle at a plane at the back of the vehicle; the vehicle's surface is colored by heat flux. Figure 74 contains a thermal image of the temperature at a plane parallel to the vehicle; the vehicle's surface is also colored by heat flux.

Figures 75 and 76 present the heat flux contours at the lower and upper surfaces of the vehicle; the scale was reduced for better visualization of the heat flux, which shows a maximum value equal to 250,000 W/m^2 (color scale adjusted for better visualization). This maximum value of heat flux is observed at the nose of the vehicle (as expected), where the kinetic energy is converted to thermal energy, due to the rapid deceleration of the flow.
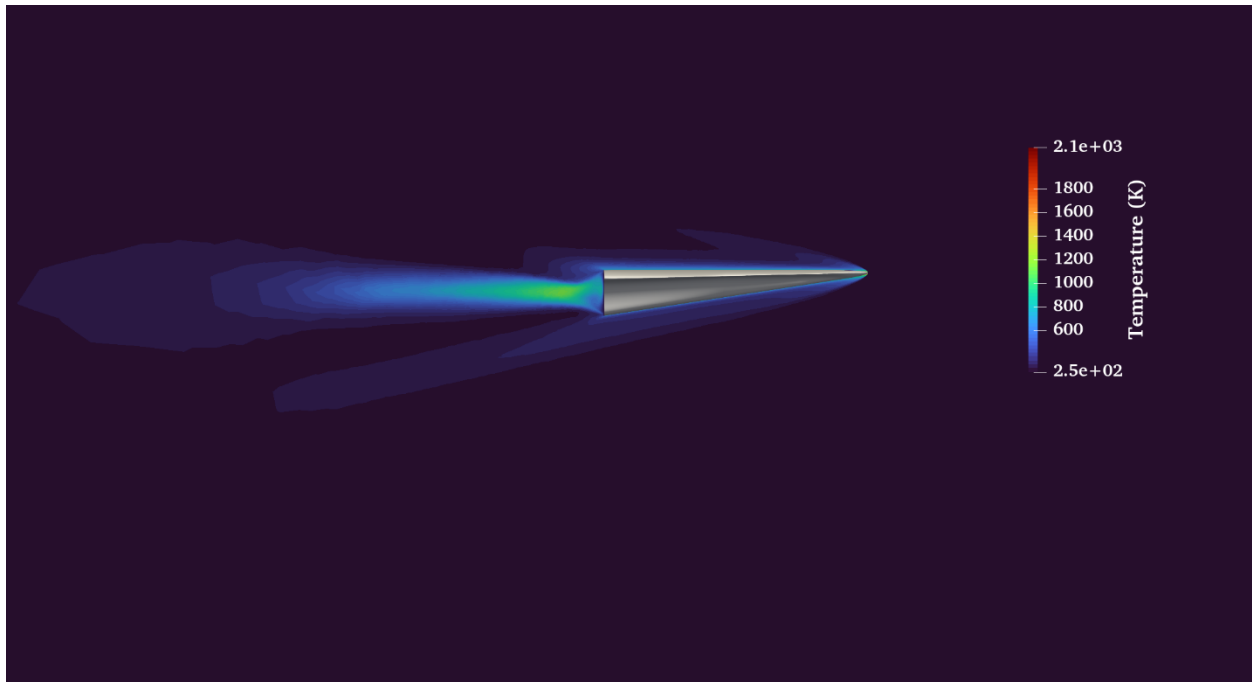
Figure 71: Temperature at the symmetry plane (0.0 AoA).
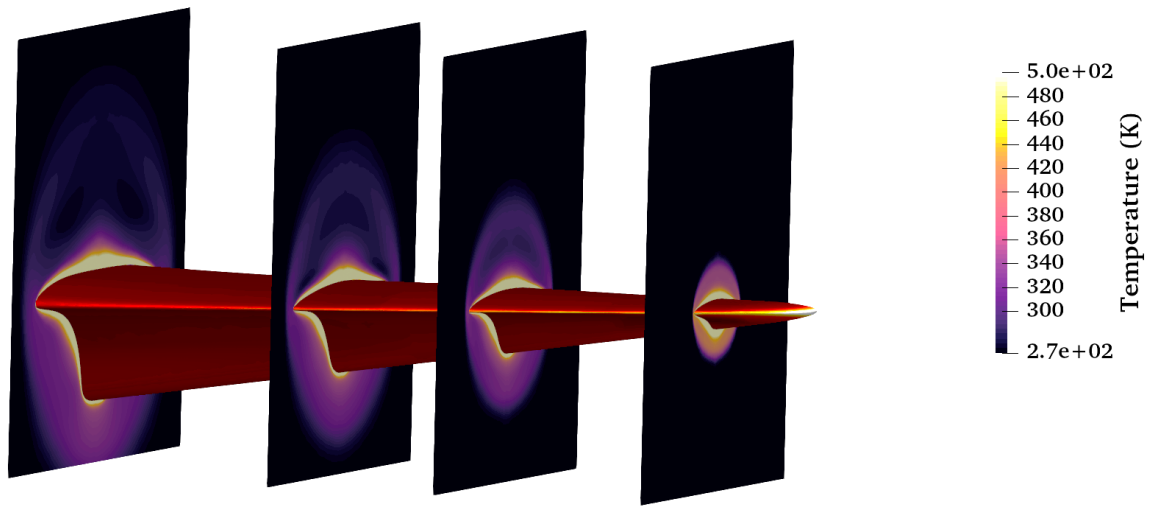
Figure 72: Temperature at four different planes around the vehicle. Surface colored by heat flux (0.0 AoA).
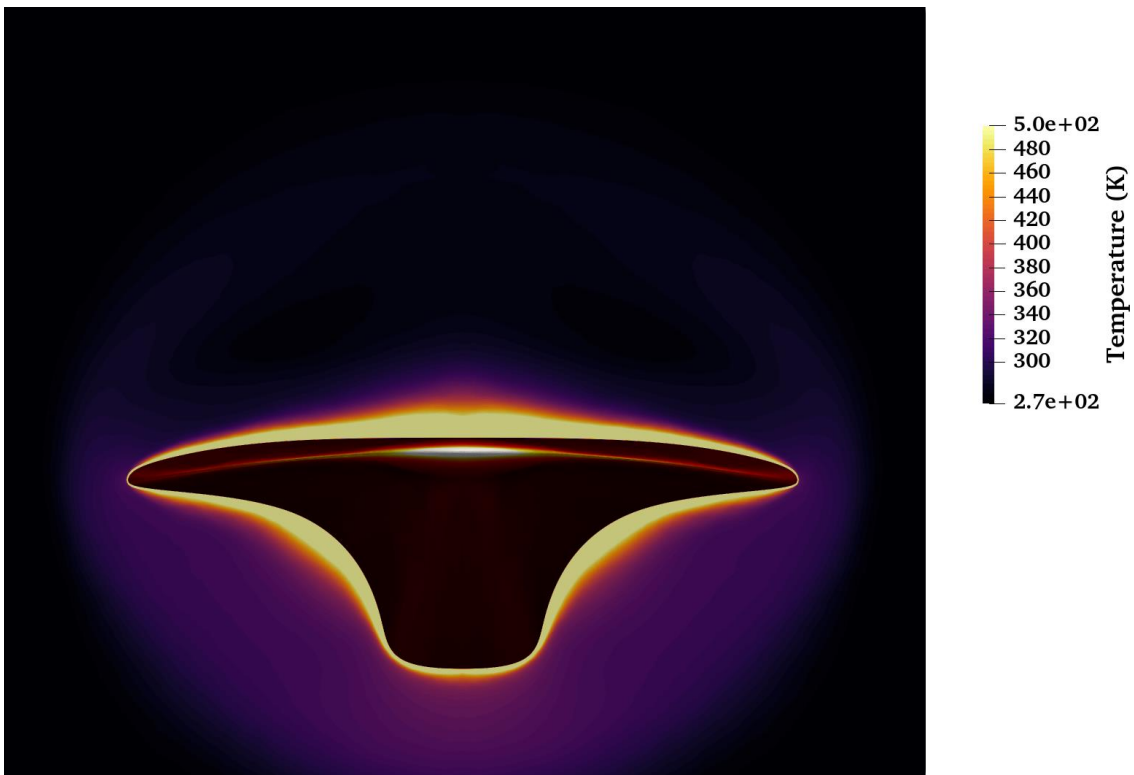
Figure 73: Thermal image of the temperature around the vehicle at a plane at the back of the vehicle. Surface colored by heat flux (0.0 AoA).
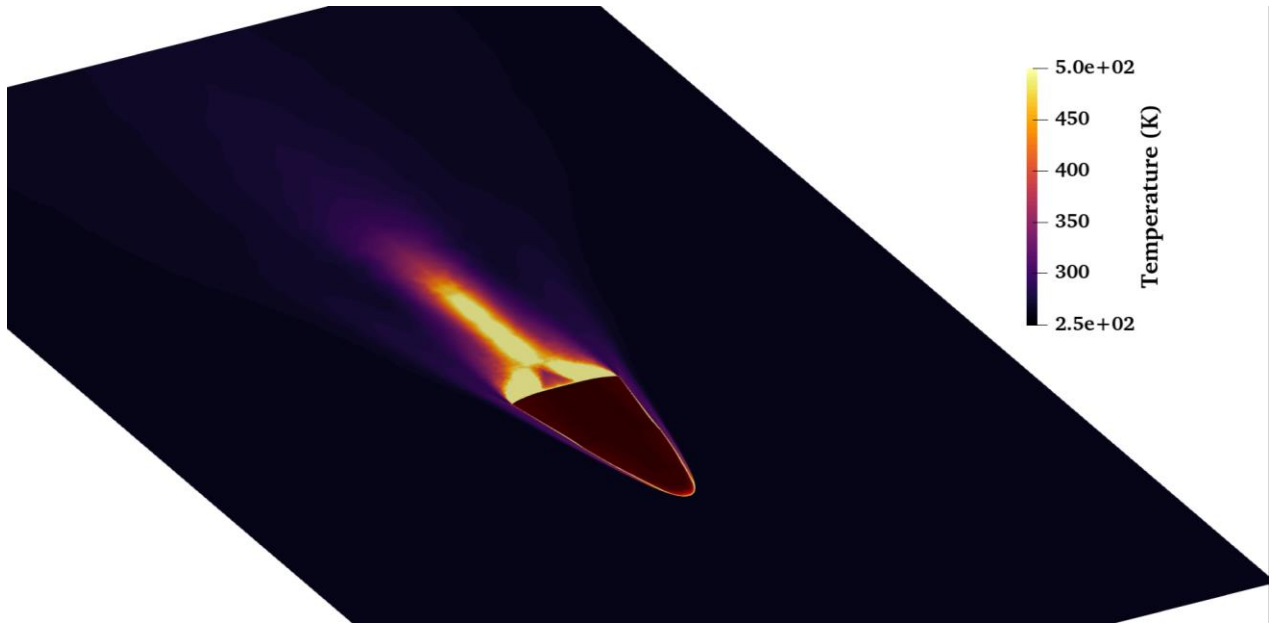
Figure 74: Thermal image of temperature at a plane parallel to the vehicle. Surface colored by heat flux (0.0 AoA).

Figure 75: Heat flux at the bottom surface of the vehicle (0.0 AoA) (Scale reduced for better visualization. Maximum value 250,000 W/m²).
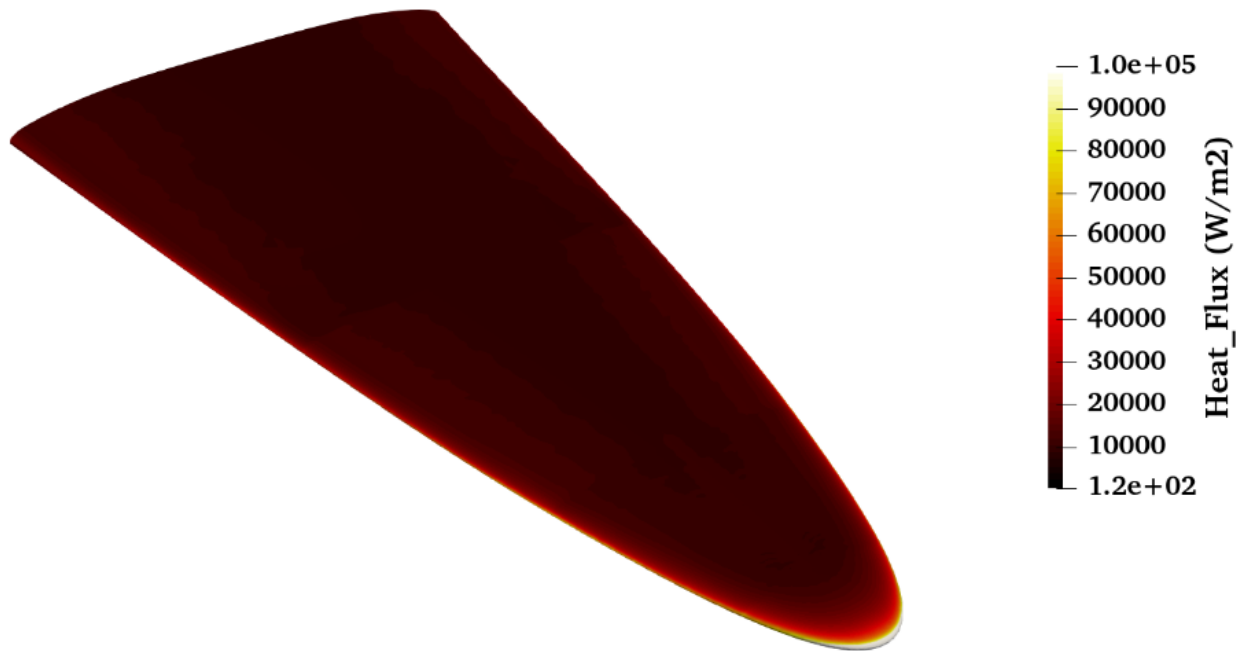
Figure 76: *Heat flux at the upper surface of the vehicle (Scale reduced for better visualization (0.0 AoA). Maximum value 250,000 W/m²).*

Figures 77 to 80 present three-dimensional renderings of the thermal trace of the vehicle, form different views. As it was previously commented, the thermal footprint of the vehicle also includes its high-temperature wake, apart from the fact that no engine is present. This is a very interesting remark, because it has an impact on the observability of the vehicle, as it increases its thermal footprint. Due to the very high computational cost of volumetric renderings, to produce the aforementioned images a grid of 300 by 300 by 300 voxels was used to sample the computational grid and then render the image volumetrically.
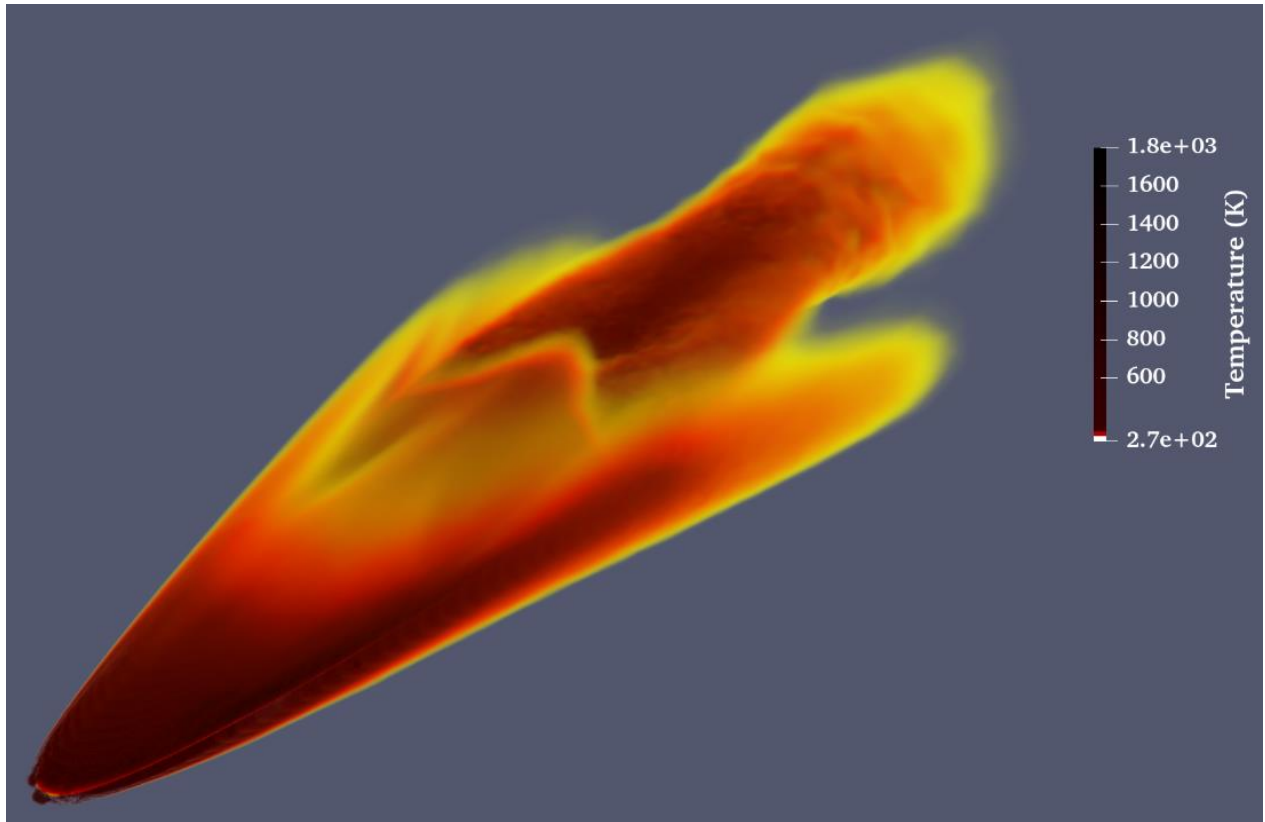
Figure 77: *Volumetric three-dimensional rendering of the thermal trace of the vehicle (0.0 AoA). (Perspective view).*
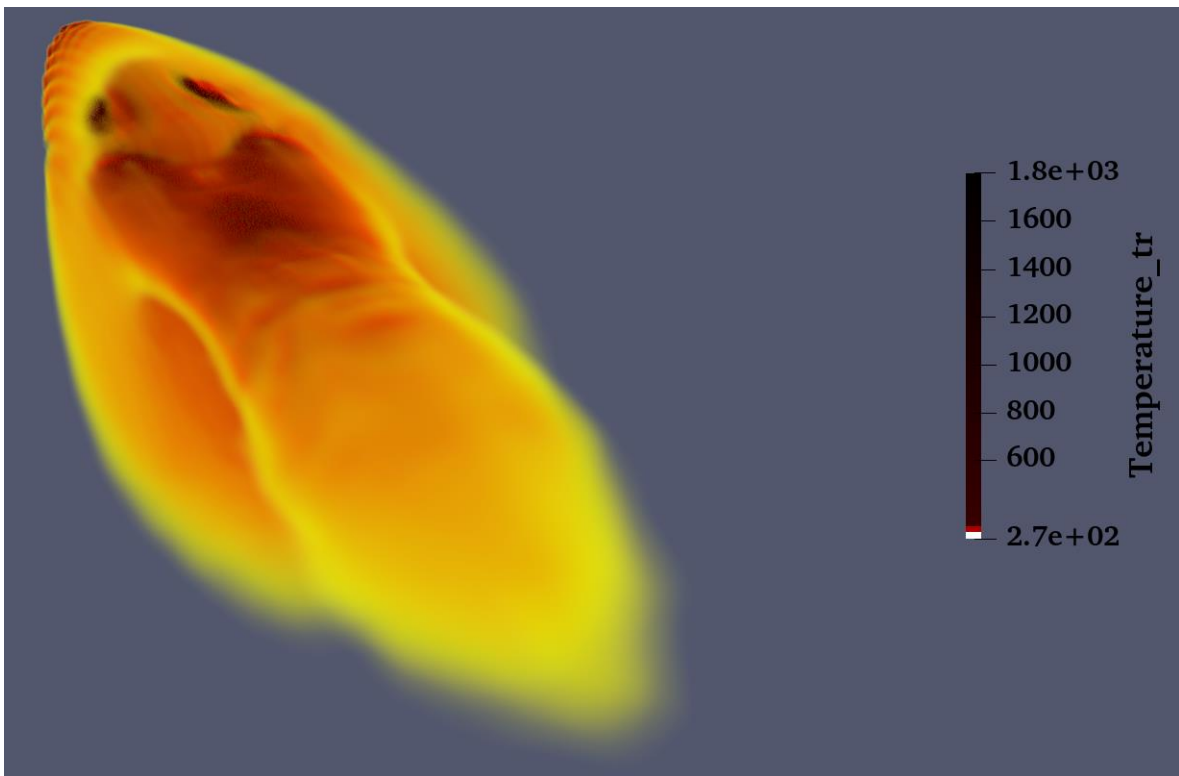
Figure 78: Volumetric three-dimensional rendering of the thermal trace of the vehicle (0.0 AoA). (Rear view).
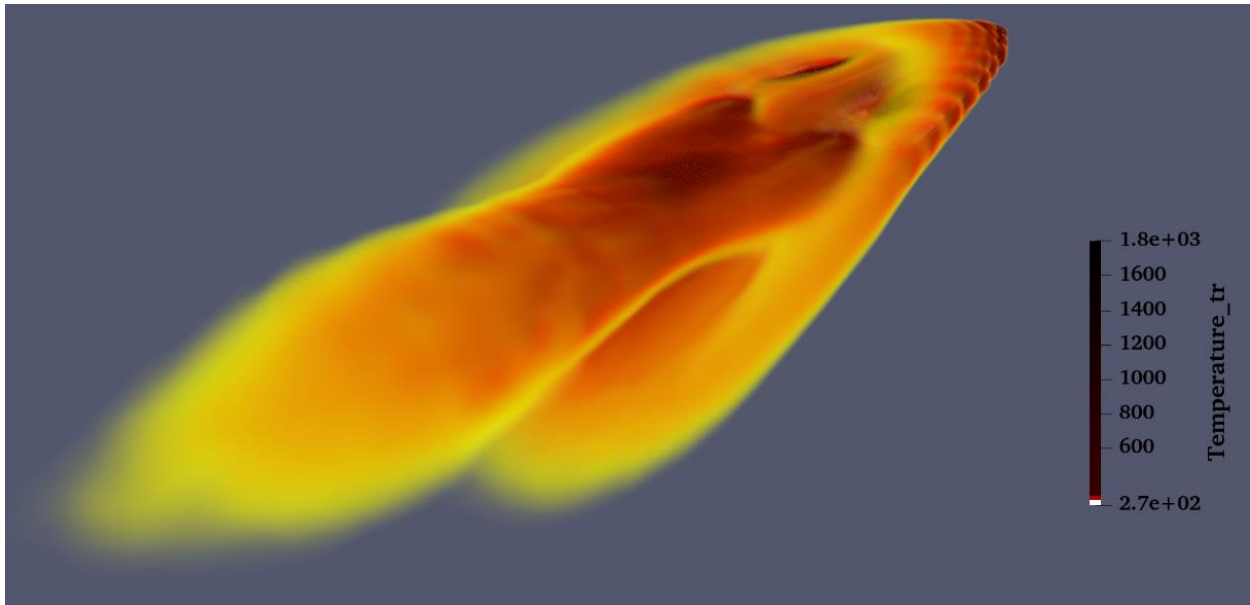
Figure 79: Volumetric three-dimensional rendering of the thermal trace of the vehicle (0.0 AoA). (Rear view).
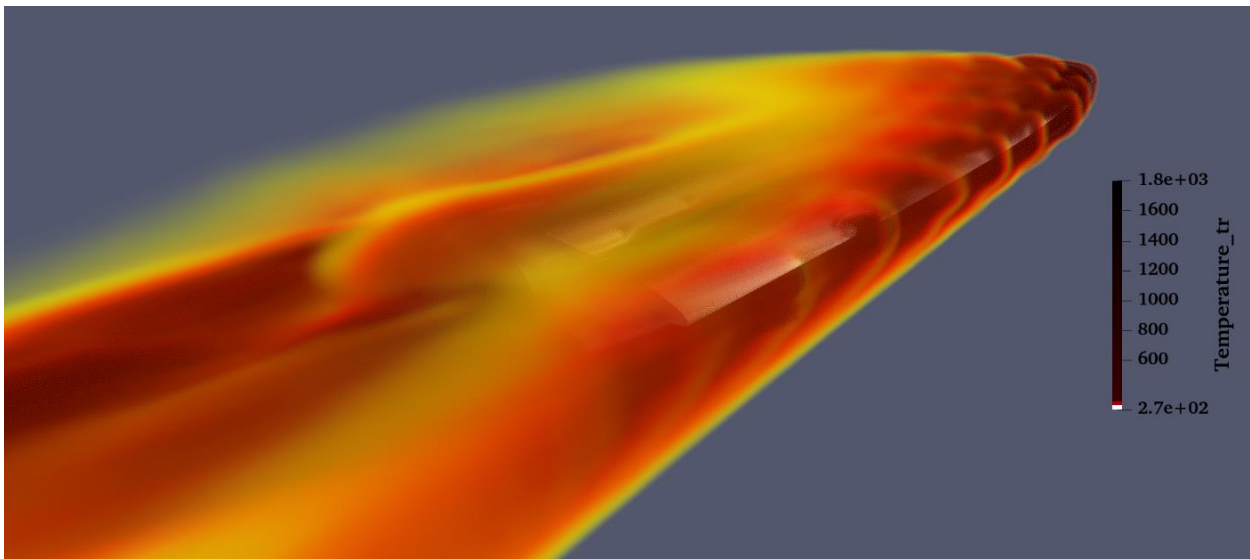
Figure 80: Volumetric three-dimensional rendering of the thermal trace of the vehicle (0.0 AoA). (Rear view).

7. Evaluation of the waverider design at 30 km altitude and 2 deg. AoA.

In the realm of hypersonic flight, the performance and aerodynamic efficiency of vehicles are paramount, particularly for applications pertinent to defense and reconnaissance. This analysis delves into an additional simulation conducted on the previously designed and simulated waverider, a vehicle designed for sustained flight in the hypersonic regime. The vehicle was further simulated, now in off-design conditions and it's performance was accessed. More specifically, the vehicle was simulated at an even lower (compared to previous simulations) altitude of 30 km, Mach 6, and an angle-of-attack (AoA) of 2 degrees. The insights derived from this additional simulation are tailored to provide a comprehensive understanding of the vehicle's aerodynamic behavior under off-design conditions, focusing on its shockwave attachment and lift-to-drag (L/D) ratio, which holds significant implications for strategic operations. We have to highlight here that the flight simulation at lower hights (higher air densities) of such high Mach number flows impose serious challenges to the corresponding flow solvers.

As it was previously discussed, the hypersonic flight regime, defined as speeds above Mach 5, presents unique difficulties and opportunities. At such high velocities the interaction between the vehicle and the surrounding atmosphere generates strong shockwaves. The waverider design exploits these shockwaves to enhance lift, leveraging the pressure differential across its surface. By design, a waverider's shape is derived from the shockwaves it generates, aiming to achieve optimal lift-to-drag ratios and minimize thermal loads by maintaining attached shockwaves even in off-design flight conditions. For this simulation the corresponding conditions are tabulated in Table 5. The flow simulation under the corresponding coditions proved to be very difficult, with serious convergence problems. In order to achieve convergence the simulation was initiated with a first-order spatial discetization scheme (for enhanced convergence stability at the initial steps) and then was continued using a second-order spatial discetization scheme (to increase its accuracy). For the calculation of the convective fluxes the Advection Upstream Splitting Method (AUSM) scheme was used, whereas the gradients were calculated using the weighted least squares method. The slope limiter utilized is Venkatakrishnan's, with a coefficient of 0.1, while the turbulence model used was the Negative Spalart-Almaras one-equation model (SA-neg) [48].

Table 5: *Simulation conditions.*

Pressure (Pa)	Mach Number	Density (kg/m^3)	Viscosity (N-s/m^2)	Temperature (K)	Reynolds Number
1171.87	6.0	0.0180119	0.0000148835	226.65	3,756,680

The simulation conducted at 30 km altitude, Mach 6, while a 2-degrees AoA is pivotal for assessing the waverider's aerodynamic performance outside its optimal design parameters. This altitude and speed are critical for understanding high-altitude reconnaissance and rapid response scenarios, where the thin atmosphere presents less resistance but also less lift. The chosen AoA represents a slight deviation from the neutral attitude, providing insights into the vehicle's stability and control during flight. Figure 81 and Figure 82 show the Mach number at the symmetry plane and at a plane 20cm upsteram the vehicle's back vertical surface. Figure 82 demonstrates also the shock structure around the vehicle.
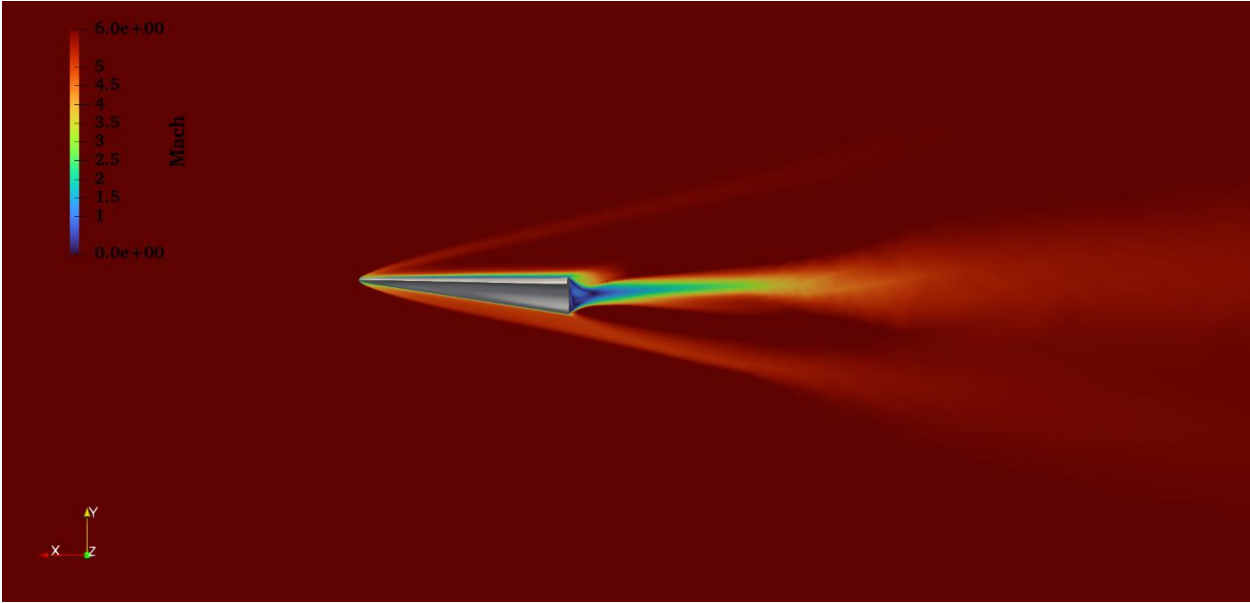
Figure 81: *Mach number contours at the symmetry plane.*
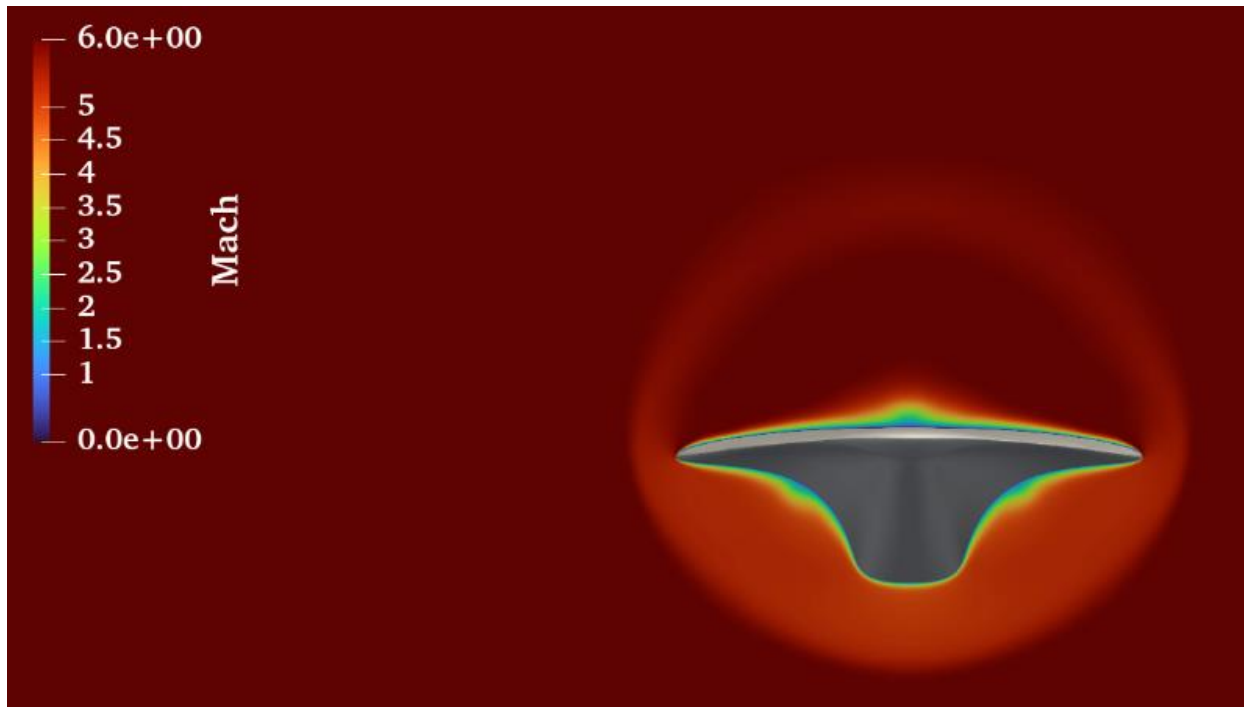
Figure 82: *Mach number contours at a plane 20cm upstream the back surface of the vehicle.*

Figure 83 depicts the turbulent viscosity distribution at the back of the vehicle while Figures 84 and 85 show pressure contours around the vehicle. Figure 84 depicts the pressure at the symmetry plane of the vehicle, while Figure 85 the pressure contours around the vehicle at a plane 20cm upstream the back face of the vehicle. As seen in Figure 85, the maximum pressure below the vehicle is more than 30,000 Pa while the maximum pressure at the plane of symmetry is about 67,000 Pa which is about 57 times higher than the freestream pressure. Figure 86 shows the Q-criterion around the vehicle. The complicated shock system structure can be clearly observed. Although the vehicle is simulated in off-design conditions it can be observed that the shock is still attached to the vehicle's leading edges.
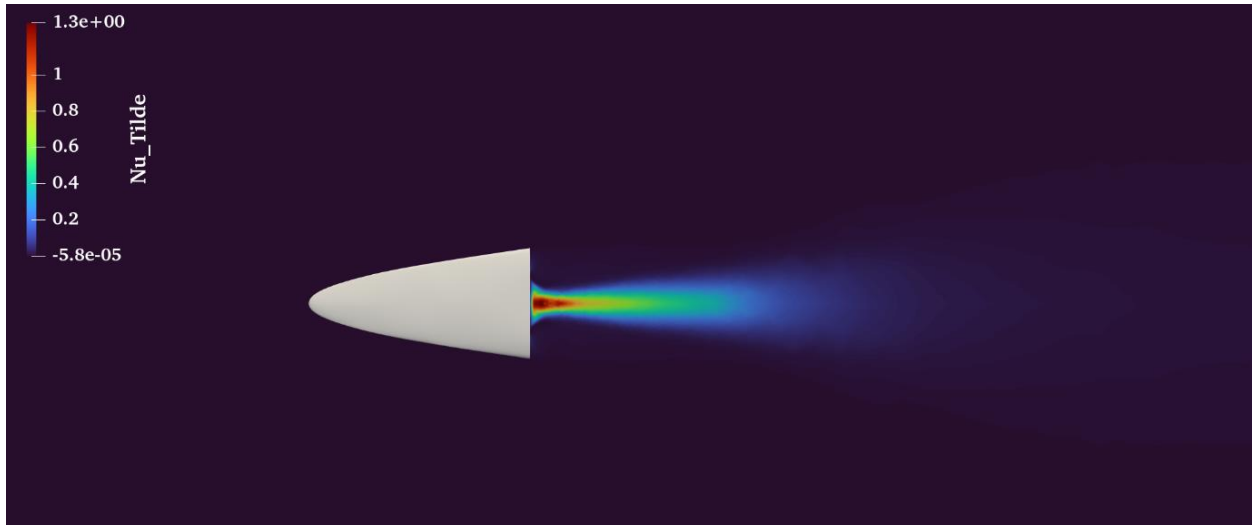
Figure 83: Turbulent viscosity downstream the vehicle.
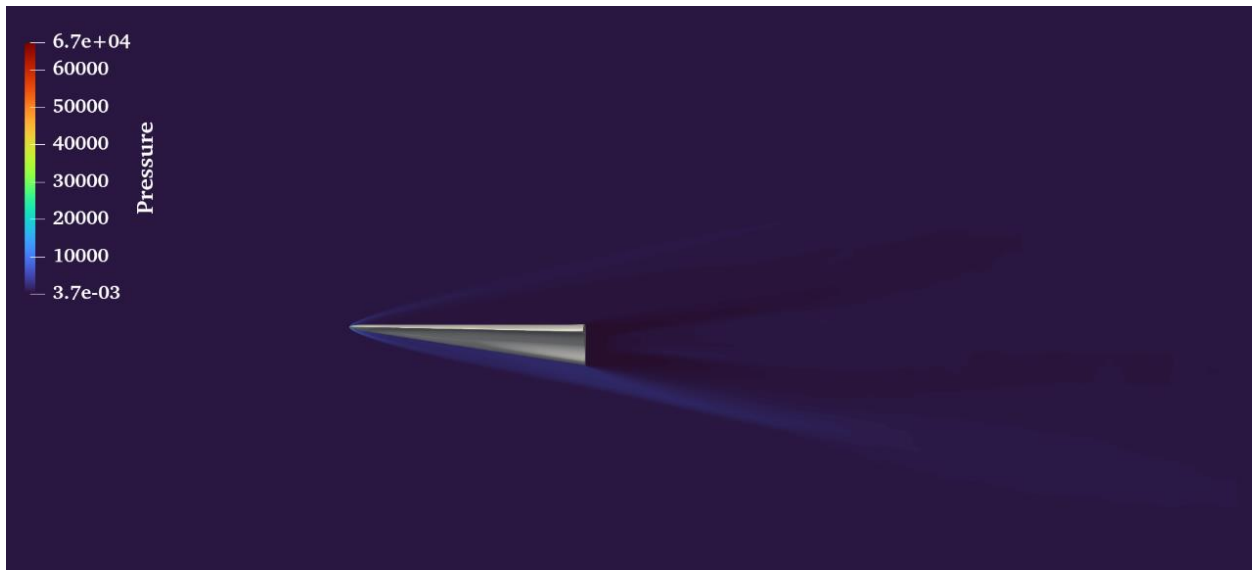
Figure 84: Pressure contours at the symmetry plane of the vehicle.
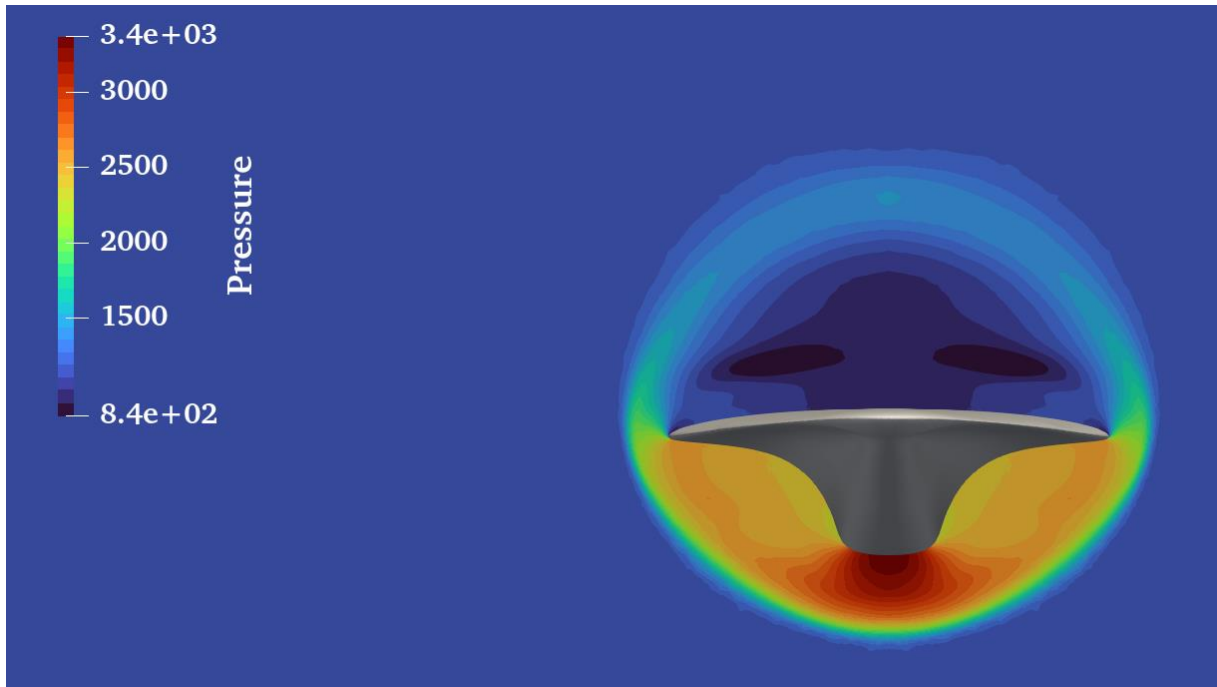
Figure 85: *Pressure contours at a plane 20cm upstream the back surface of the vehicle.*
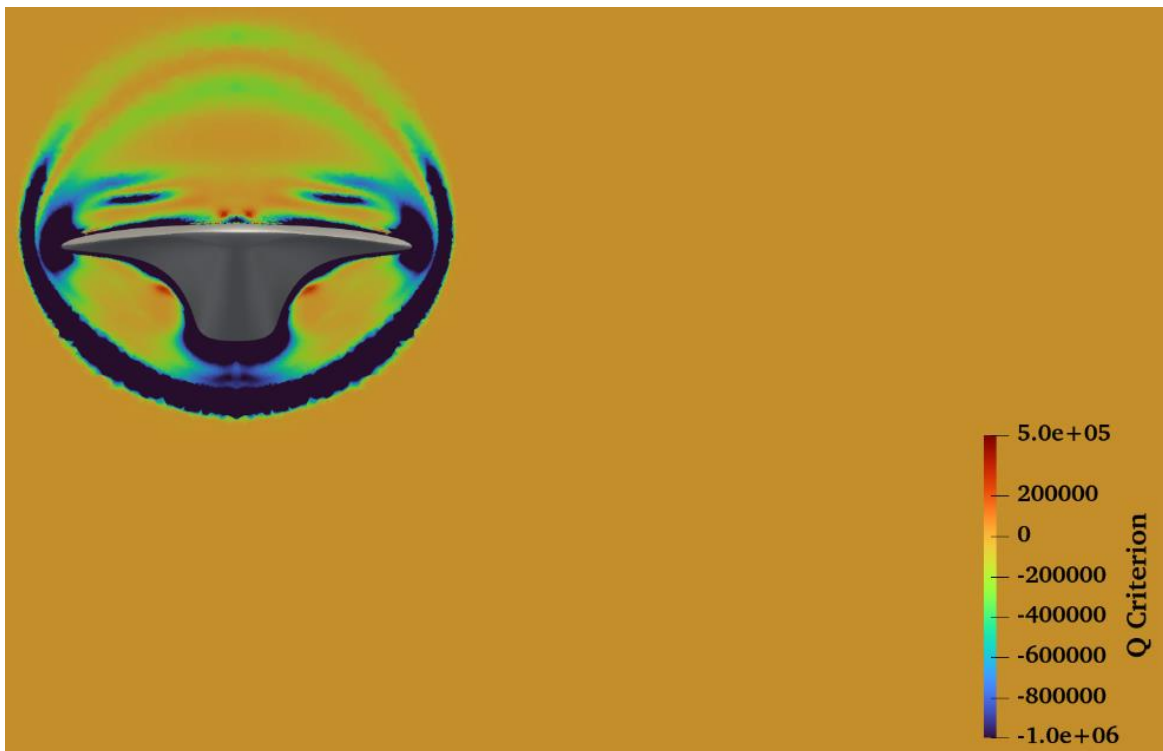
Figure 86: *Q-criterion contours at a plane 20cm upstream the back surface of the vehicle.*

Figures 87, 88 and 89 show the pressure contours at the upper and lower surface of the vehicle and the heat flux on the vehicle's surface, respectively. As evidenced in Figures 87 and 88 the pressure on

the upper surface is much lower than the pressure at the lower surface, indicating that the vehicle can generate lift and, thus, glide. Figure 89 demonstrates the maximum value of heat flux around the vehicle's nose. The colormap of the picture has been tweaked for clarity. The maximum heat flux value is **255.376** kW/m² . The maximum temperature occurs close to the vehicle's nose, while it's value is **1910.82 K**. The temperature at the back of the vehicle is also high, as demonstrated in Figure 90. Figure 91 depicts the temperature at the back of the vehicle, where two vortices co-exist (as seen in Figure 93). As it can be observed, the minimum temperature is about **1200 K**.

Figure 87: *Pressure contours on the vehicle's surface.*
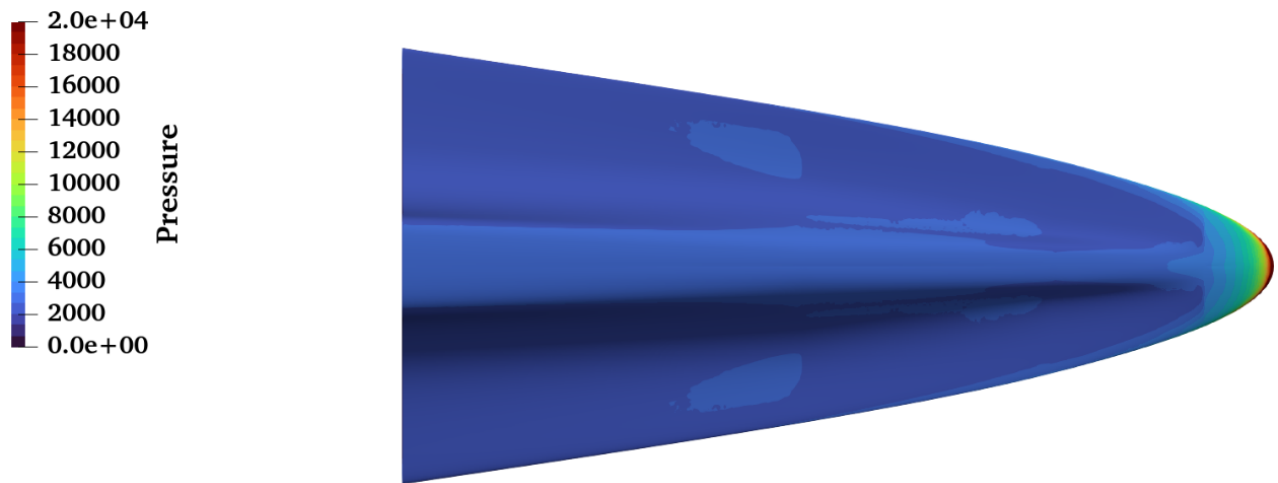
Figure 88: *Pressure contours on the vehicle's lower surface.*
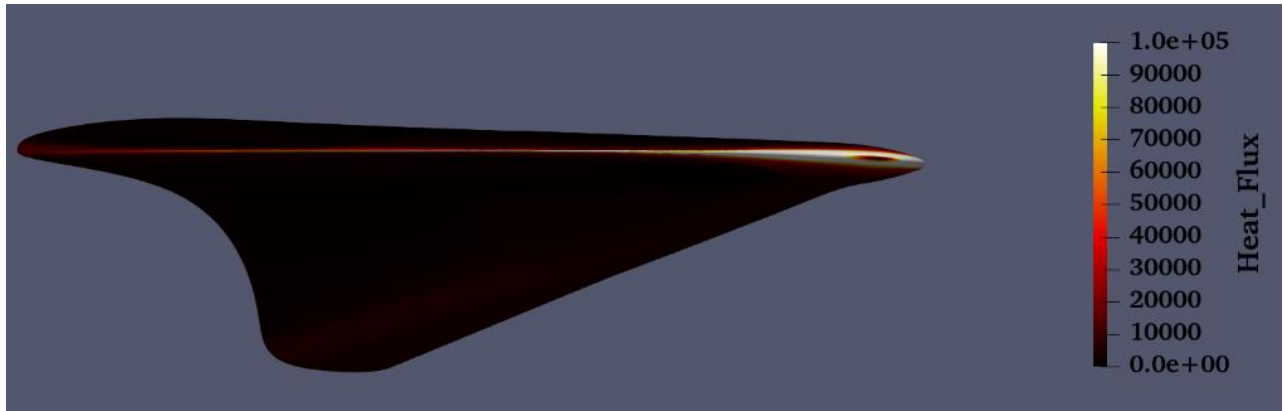
Figure 89: Surface heat flux distribution.
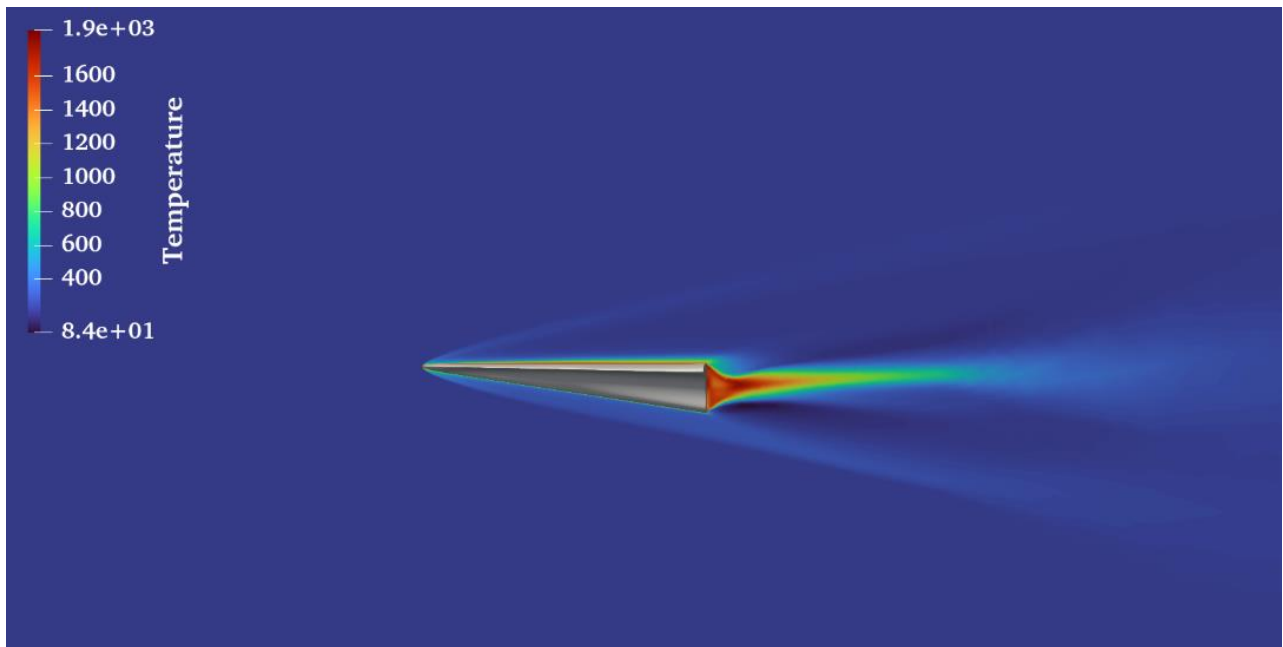
Figure 90: Temperature distribution at the symmetry plane.
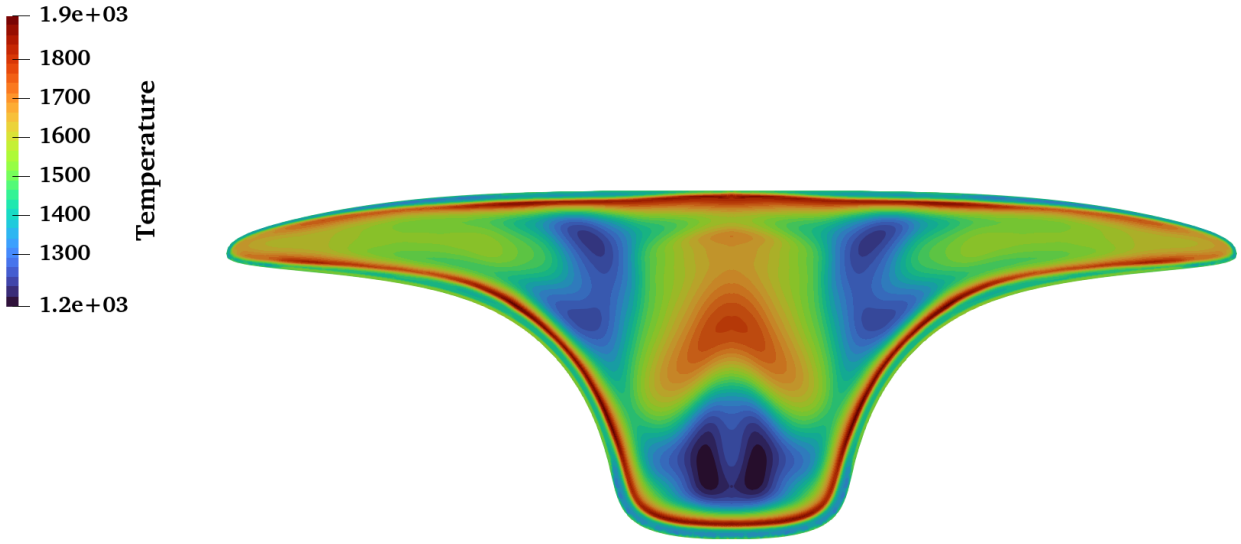
Figure 91: Temperature distribution at the back face of the vehicle.
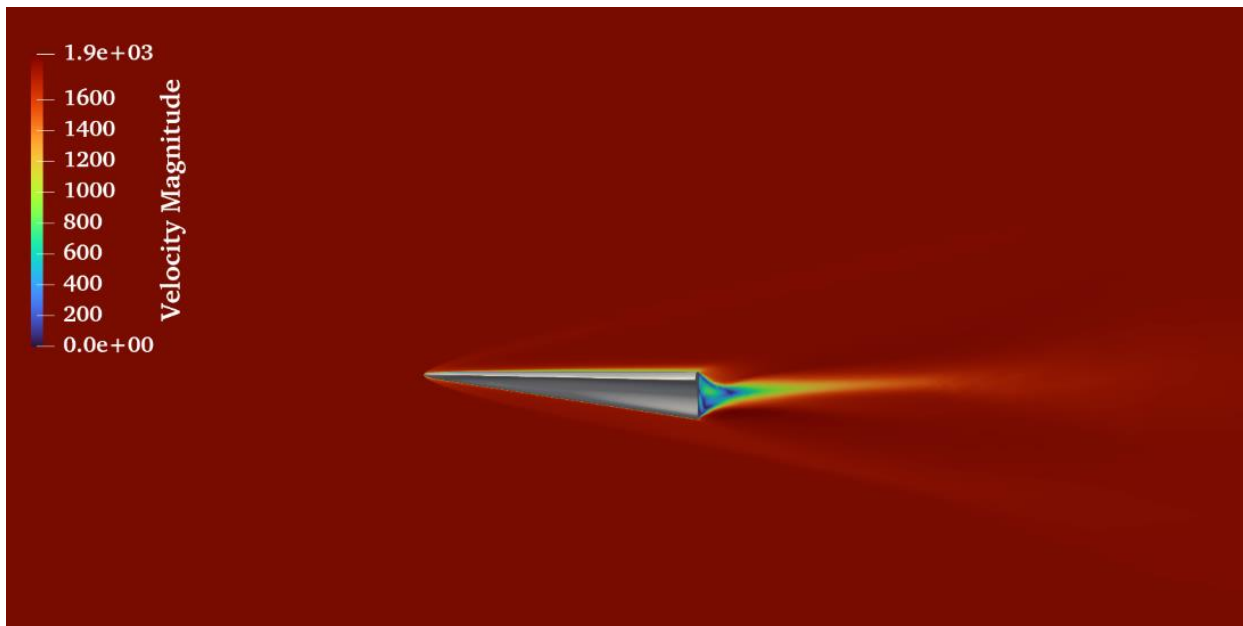
Figure 92: Velocity distribution at the symmetry plane.
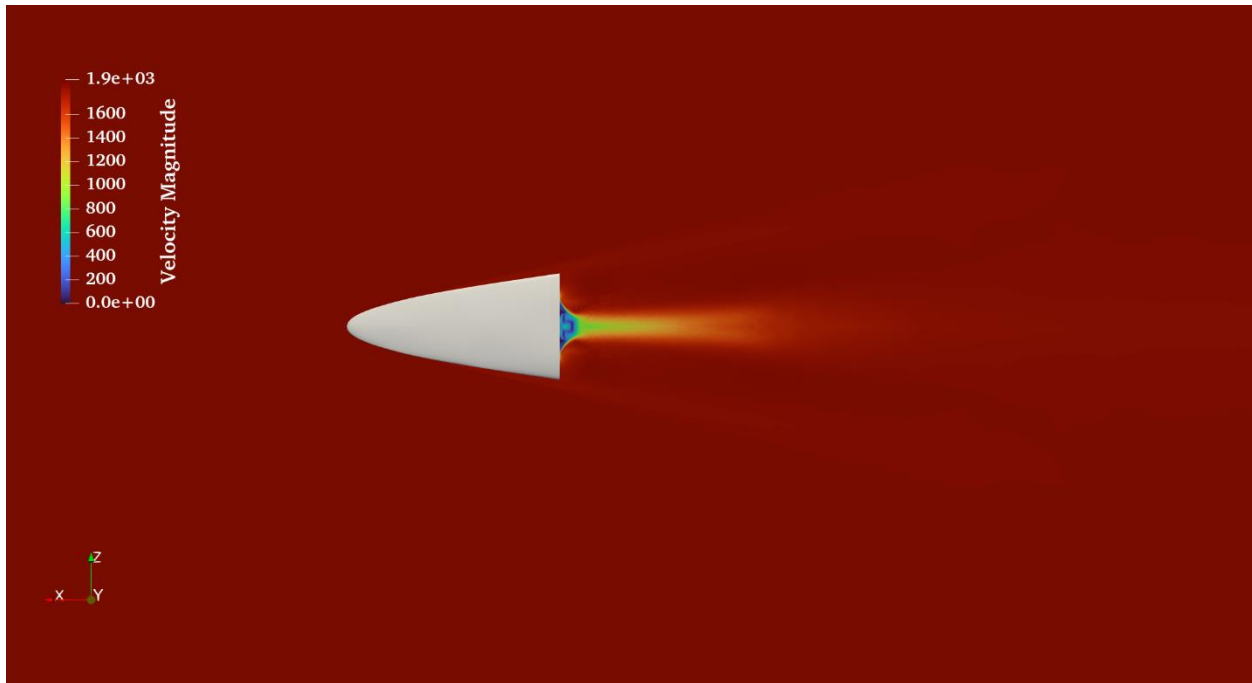
Figure 93: *Velocity distribution at a horizontal plane.*
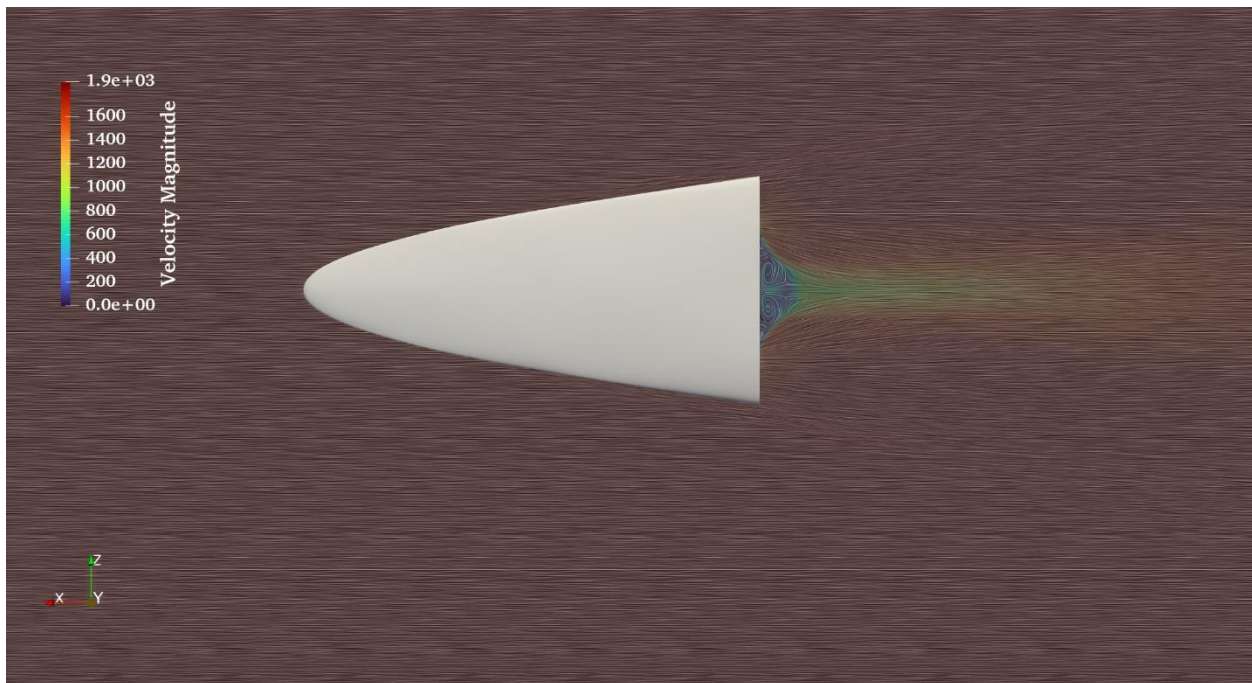
Figure 94: *Vortex formations downstream the vehicle.*

A key observation from the simulation is the attached shockwave to the waverider's leading edges, even in off-design conditions. This phenomenon is crucial for several reasons. Firstly, it indicates that the vehicle can maintain efficient shockwave-boundary layer interaction, essential for sustaining lift

and minimizing drag at hypersonic speeds. Secondly, the maintenance of attached shockwaves reduces the likelihood of shockwave-induced separation, which can lead to significant increase in drag and potential loss of vehicle's control. This characteristic indicates the robustness of the current waverider design, ensuring reliable performance across a range of operational conditions. The L/D ratio, computed equal to **1.463**, is a critical metric in evaluating the aerodynamic efficiency of a vehicle. In the context of hypersonic flight, this value is indicative of the waverider's capability to glide and maneuver with a relatively high degree of efficiency.

The findings from this simulation have significant operational implications, especially in the domains of surveillance, reconnaissance, and rapid-response capabilities. The ability of the waverider to maintain attached shockwaves and demonstrate aerodynamic efficiency at high altitudes and hypersonic speeds enhances its potential. Moreover, the robust performance of the waverider in off-design conditions suggests that it can be reliably deployed in a variety of atmospheric conditions and flight profiles, enhancing operational flexibility. The L/D ratio of 1.463, in particular, indicates a platform capable of gliding, allowing for the execution of maneuvers or stealthy insertion into contested areas, without relying heavily on propulsion, thus reducing thermal signatures and enhancing survivability.

The simulation of a waverider at 30 km altitude, Mach 6, and a 2-degrees angle of attack provides insights into its aerodynamic performance and operational potential. The attached shockwave phenomenon and the resultant L/D ratio of 1.463 underscore the vehicle's efficiency and robustness in the hypersonic regime.

8. The problem of sensing

8.1 Problem definition

In this section, the problem of sensing hypersonic vehicles will be discussed; open-source information will be used. Three different missions are required by the corrresponding systems [49]:

- Missile Warning
- Missile Tracking
- Missile Defense (Fire control-quality Tracking)

The first mission corresponds to the early detection of missile launches, with some ability of tracking their trajectories in early stages of flight. Currently, for USA, this mission is undertaken by SBIRS Space Based Infrared System) [50] and DSP (Defense Support Program) [51] satellites.

The second mission involves tracking missile trajectories during their complete flight, even after main motor burnout. This mission is currently undertaken in the USA by the SBIRS satellite constelation and surface-based radars.

The third mission, being the most demanding and crussial one, involves tracking trajectories with enhanced data quality to directly support their interception by surface-based, airborne or space-based interception systems. Contrary to the previous two missions, this one requires narrow field-of-view sensors. This mission is currently mainly based on surface radars, which have an obvious limmitation: the hypersonic vehicles, with their low-altitude, unpredictable flight path can fly under the horizon of surface-based radars, and can be detected only at their final stages of their flight, with insufficient reaction time due to their high speed; Earth's curvature is the main problem for surface-based sensors. Therefore, **elevated sensors** are mandatory for such a mission.

8.2 Alternative satellite orbits

A satellite with the corresponding sensors (of any kind) can be positioned in different orbits, each one of them providing different advantages and/or disadvantages for the corresponding mission.

Low Earth Orbit (LEO), corresponding to altitudes between 400 km and 2,000 km from Earth's surface. Due to the low launch cost for a LEO satellite, it is highly popular for commercial applications and currently 80% of satellites are using this orbit. The proximity to Earth's surface and to the flight altitude of hypersonic vehicles enhances the resolution of the corespodning optical sensors, requiring smaller appertures, which have a positive impact to the statellite mass, its cost, as well as the launch cost. On the other hand, the proximity between the sensor an the target, epecially when the target has a hypersonic speed, and the high relative speed between the satellite at a low orbit and the surface, can produce motion blurring and motion streaking to the pictures, even for very small sensor integration times. As a result, sensors with elevated sensing and processing characteristics are required for LEO, compared to higher orbits. Additionally, their low positioning with respect to Earth's surface decreases their surface coverage (for a predefined angle of view), compared to higher

altitudes. Taking into account that each Earth's region should be continuously sensed by at least two satellites, this smaller coverage asks for a much larger nuber of satellites in LEO, compared to higher orbits. An additional dissadvantage of LEO satellites is their vulnerability and exposure to various anti-satellite weapons, and space debris. Another problem of LEO satellites is their small lifespan, due to the drag of the (rarefied) atmosphere, which decelerates them and necessitates additional propulsion. Satellites at lower orbits have dramatically smaller lifespans, compared to those at higher orbits.

Medium Earth Orbit (MEO), corresponding to altitudes between 2,000 and 35,999 km from Earth's surface. Only 3% of satellites are placed in this orbit. The satellites that support the Global Positioning System (GPS) and the European Galileo navigation system are both positioned in MEO, the first in 20,180 km and the second in 23,222 km above Earth's surface. The reason is that this altitude provides much larger coverage areas for each satellite and slower relative motion between the surface and the satellite. The satellites in MEO suffer high radiation levels (Van Allen Radiation Belts – Figure 95) [52], due to the characteristic shape of the geomagnetic field, so specific altitudes and inclinations are used to minimize the corresponding radiation effects. The radiation causes degradation to electronic circuits, processors and sensors, demanding special high-cost materials and manufacturing procedures, and special error-correcting software. The selection of a MEO provides a significant resilience to a satellite, due to its much higher altitude compared to LEO, which substancially decreases the vulnerability from anti-satellite weapons.

Geosynchronous Orbit (GEO), corresponding to an altitude about 36,000 km above Earth's surface at the equator's plane. At this orbit a satellite rotates with the same angular velocity as Earth and it has no relative velocity with respect to Earth's surface, being stationary with respect to the surface. The SBIRS satelites are positioned in GEO orbit, as it provides a wide surface coverage with a small number of satellites, without any relative motion between the satellite and the surface. Additionally, the vulnerability from anti-satellite weapons is minimal.

Highly Elliptical Orbits (HEO). Such orbits are used to cover Earth's high latitude regions near the poles. In their apogee (their longest distance form the surface) they have their lowest velocity and they can stay for a longer time over the specific region. They are perfectly combined with GEO satellites, to cover both low and high latitude regions with a small number of systems. Specifically, the SBIRS [53] constellation combines 6 GEO and 2 HEO satellites. Systems in GEO and HEO are very sophisticated and costly, compared to those at lower orbits; however, much fewer satellites are needed to cover the Earth's surface.
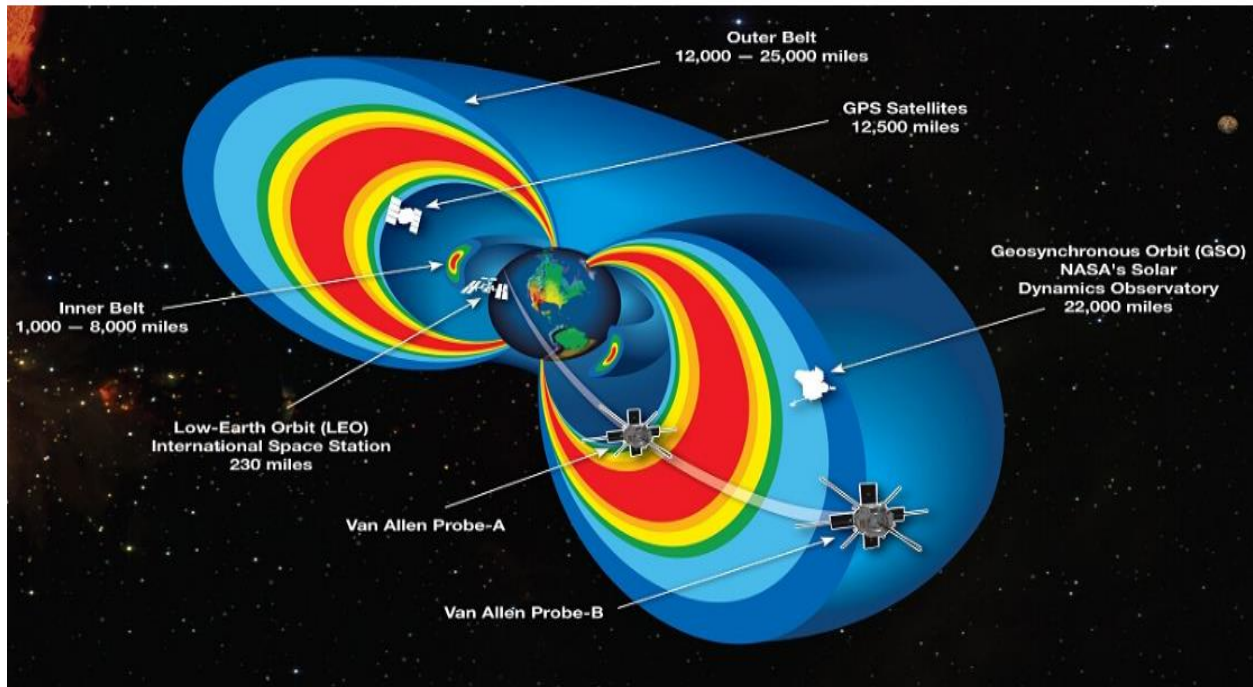
Figure 95: *The Van Allen Radiation Belts (credit: NASA).*

From the previous analysis can be realized that a single-orbit system is not the optimal one and hybrid systems with satellites in different orbits can provide the right blend for optimized performance and cost, higher robustness and lower vulnerability.

8.3 Infrared signature

Infrared signature is the appearance of objects to infrared sensors. An infrared signature depends on many factors, including the shape and size of the object, temperature and emissivity, reflection of external sources (earthshine, sunshine, skyshine) from the object's surface, the background against which it is viewed, and the waveband of the detecting sensor [54]. As a result, the prediction/simulation of infrared signature of an object against its background is a very complicated procedure.

The problem of sensing hypersonic vehicles (especially waveriders, or balistic missile reentry vehicles) is very chalenging due to their low temperature (compared to booster plumes of rockets) and the variation of surface temperature with the phase of their flight. A very characteristic representation of this fact is depicted in the following Figure 96. Moreover, the sensors should distinguish the thermal footprint of the vehicle against background Earth's temperature, through various and unpredictable weather conditions, against the light of stars and satellites in the cold background of space, and under the strong light of the Sun. Taking also into account the small temperature difference between the vehicle and Earth's surface, the relative motion of the satellite

and the surface, and the high speed of the observed vehicle, it is more than obvious that state-of-the art hardware and software is required.
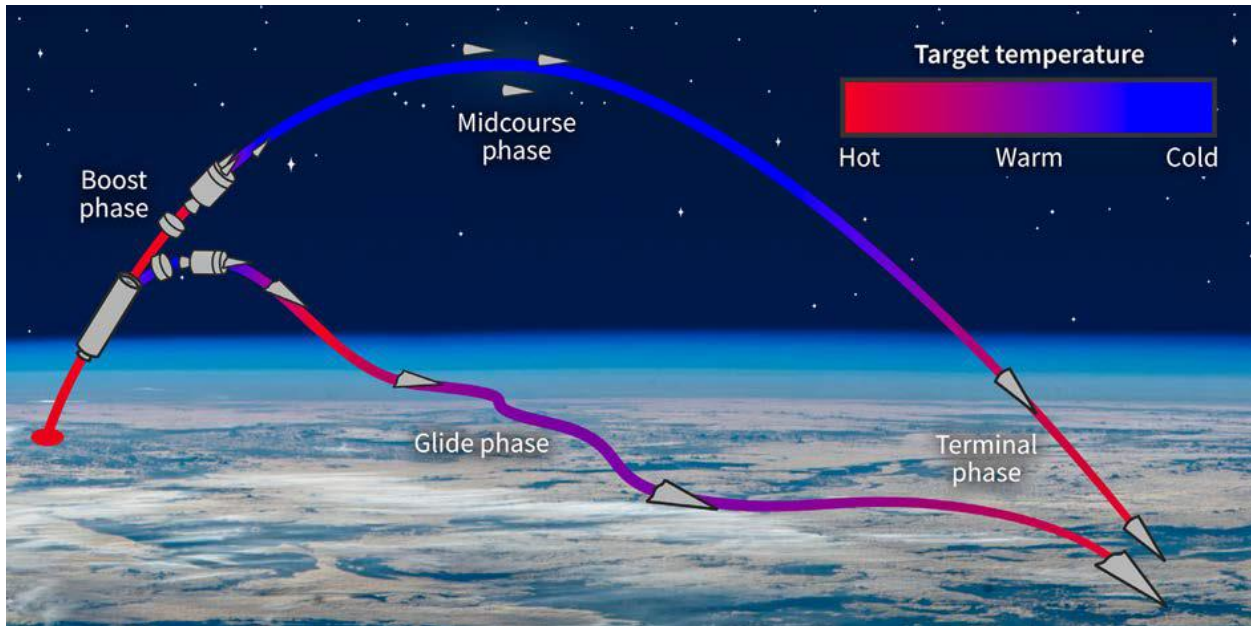
Figure 96: *Variation of vehicle's temperature with the phase of its flight (Credit: CSIS – Center for Strategic & International Studies – Missile Defense Project).*

In order to assess the radiance footprint of a hypersonic vehicle, **dedicated software** is required [55]. Such software can be used to model the optical signature of a vehicle for an arbitary orientation and in a specific waveband. In the following Figure 97, such a simulation result for the Space Shuttle is presented; the applied software utilized material dependent optical properties, accounting for spectral and angular variation, as well as sensor spectral response behavior of the vehicle surface material.
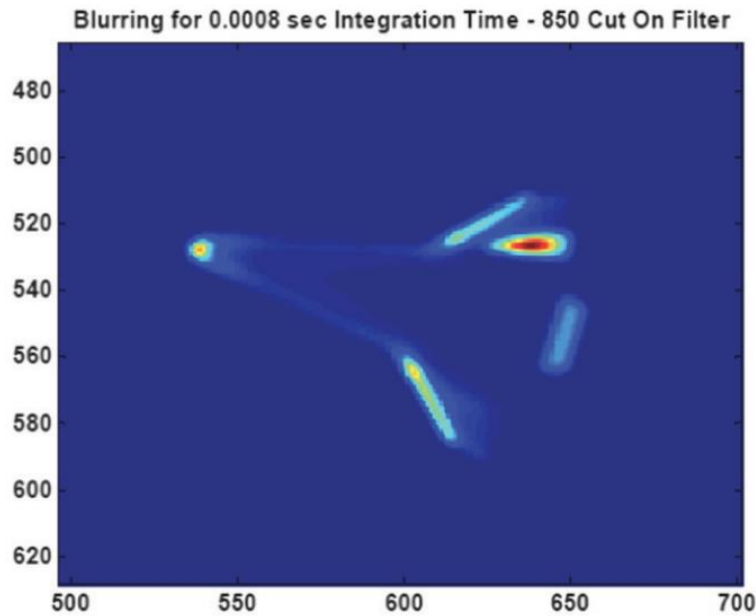
Figure 97: *Predicted Space Shuttle radiance
(https://ntrs.nasa.gov/api/citations/20130011566/downloads/20130011566.pdf).*

The supersonic exhaust plume of a rocket motor can radiate very strong thermal emissions, as the maximum temperature of the plume can reach up to 3000 K. For such high temperatures, despite the fact that the flow and temperature characteristics are complicatd, several methods (based on Computational Fluid Dynamics) exist to simulate the corresponding flow field and subsequently compute a radiance footprint [56]. Moreover, faster methods have been recently proposed, for such applications [57, 58]. A review of different methodologies and codes for the prediction of infrared signature of aerospace vehicles can be found in the work of Mahulikar et al. [59].

NIR.ATAM (NATO InfraRed Air T.Arget Model) is a software that predicts IR radiation of an aircraft in its natural surroundings (including hypersonic vehicles). The software takes into account the IR radiation emitted by aerodynamically and internally heated surfaces, hot engine parts and combustion gas and particles in the exhaust plume. The reflected radiation of the sky and terrain background and the sun on the aircraft surface is also calculated. The atmospheric transmission and emission between target and observer and the radiation of a homogenous background in the scene is determined [60, 61].

One of the most advanced and multi-disciplinary software, used for the design, modeling and simulation of space-based systems is **ANSYS STK** (Systems Tool Kit); it provides a physics-based modeling environment for analyzing platforms and payloads in a realistic mission context [62]. Various specialized add-ons to the basic software are available. For example, STK Premium Space adds advanced modeling of space-based platform and payload systems to STK Pro, including advanced orbit design and maneuver planning for satellite and spacecraft missions. STK Premium adds analytical tools to improve the understanding of system performance. Concerning the sensing of hypersonic vehicles, the software can be used for [63]:

- Trajectory planning: Design spacecraft trajectories from LEO to deep space, including advanced maneuver planning. Define orientations to optimize quality-image capture and downlink opportunities. Build large satellite constellations.
- Electro-optical and infrared sensor systems: Model the detection, tracking, and imaging performance of electro-optical and infrared sensors to support concept development, design, field testing, and operations. Simulate accurate sample data for the development of image analysis and evaluation techniques, algorithms, and tools.
- Multidomain concept of operations: Plan space, air, and terrestrial assets in a single mission environment.
- Space systems design: Model across the engineering life cycle, from concept development to validation of operational mission requirements, using high fidelity orbit and subsystem modeling capabilities.

STK Premium (Air) provides advanced flight performance modeling, mission planning, and simulation of complex aircraft systems [64]. Analyses and simulation capabilities include:

- Defensive system evaluation: Analyze detection system capabilities across multiple domains against realistic threat flight profiles, thermal signatures, and radar detectability.
- Hypersonic modeling: Use ramjet and scramjet engine models and 6DOF dynamics to model hypersonic and extra-atmospheric trajectories.
- Electro-optical and infrared sensor systems. Model the detection, tracking, and imaging performance of electro-optical and infrared sensors to support concept development, design, field testing, and operations. Simulate accurate sample data for the development of image analysis and evaluation techniques, algorithms, and tools.

From the previous analysis it can be easily deduced that the sensing of hypersonic vehciles is a very complicated and highly demanding problem. Even the simulation of their sensing characteristics requires specialized analysis and simulation software. Software platforms like the ANSYS STK, with their wide analysis and simulation capabilities of complicatd systems and missions, demonstrate the interdisciplinary nature and the specialized resources that are required for such endeavours. Nevertheless, the temperature and surface heat transfer characteristics of a hypersonic vehicle at different altitudes and different flow conditions is a required input to such software. Therefore, the presented simulation results can be further utilized to compute the infrared signatures of the designed vehicles, provided that such simulation software will be available.

9. Conclusions

The main objectives of this work were the following:

- to review some of the available design methodologies, which have been proposed for the design of waverider hypersonic vehicles,
- to apply such a methodology for the geometric design of a typical waverider hypersonic vehicle, under specific flight conditions at high altitude,
- to simulate the hypersonic flow around this vehicle, so as to evaluate the design itself and to provide an insight to the related flow phenomena (for an altitude of 90 km, using the open-source SPARTA DSMC simulation software),
- to design and simulate a preliminary two-dimensional geometry of a scramjet-powered hypersonic vehicle, in order to have a first insight to the flow phenomena (especially the shock waves and their interaction with the scramjet intake),
- to design a typical scramjet-powered hypersonic three-dimensional vehicle (based on the geometry of the successful X-51A vehicle),
- to simulate the aforementioned vehicle and derive flow properties and flow phenomena, for specific flow conditions at an altitude of 90 km (using the open-source SPARTA DSMC simulation software),
- to simulate the designed waverider vehicle at lower altitudes of 45 km and 30 km, at 0 and 2 degrees AoA respectively, (using SU2, an open-source, non-equilibrium Navier-Stokes solver) and derive flow properties and flow phenomena for the corresponding flow conditions,
- to take a first look to the sensing problem of a hypersonic vehicle.

As mentioned before, two different simulation tools, both developed for rarefied flow regimes, have been utilized during this work. The first is the open-source Direct Simulation Monte Carlo (DSMC) solver SPARTA, while the second one is the non-equilibrium Navier-Stokes solver SU2. The two solvers are based on completely different methodologies; the first one simulates particle collisions, while the second one iteratively solves the discretized form of the Navier-Stokes Partial Differential Equations (PDEs). The SPARTA DSMC solver requires extensive computational resources (a huge number of processors and simulation time), while the SU2 solver requires much less computational resources. However, SU2 depends on the convergence of the solution procedure, which is difficult for non-equilibrium flow conditions and high-Mach flows, and frequently requires fine-tuning of the boundary and initial conditions. Nevertheless, both solvers require a substantial experience, in order to provide accurate results, and they cannot be used by non-experienced users. Additionally, convergence problems have been observed for the Navier-Stokes solver, and special treatments have been required to achieve converged solutions.

Three different hypersonic vehicle designs have been produced, during this work. The first design is a typical three-dimensional waverider geometry (without propulsion). The second design is a two-dimensional scramjet-powered hypersonic vehicle, which was used to provide a first insight to the flow dynamics around such vehicles. The third design is a typical three-dimensional scramjet-powered hypersonic vehicle, with its geometry based on the successful X-51A vehicle. The first two

geometries have been simulated using only the DSMC solver SPARTA. The third vehicle geometry has been simulated in three different altitudes, using DSMC solver for the high altitude (90 km) and SU2 solver for the lower altitudes (45 km, 30km).

The following observation can be addressed from the performed simulations and the corresponding results:

The flow simulations (using both solvers) can provide a valuable insight to the complicated flow phenomena, taking place at hypersonic flight conditions, especially the formation of multiple shock waves, and their interaction with the boundary layers, formed on the solid surfaces of the corresponding vehicles. Complicated vertical structures are evident in all geometries and all flight conditions, being a source of unsteadiness and intense flow instabilities. This observation partially explains the difficulties of controlled hypersonic flight, and the numerous accidents and failures during the development and testing of such vehicles. The deep understanding of the flow details and the onset of instabilities, are of profound importance for the correct design of such vehicles.

The DSMC solver can provide more detailed and accurate information, especially in highly rarefied flow conditions, compared to a Navier-Stokes solver. However, its computational cost is comparatively very high, and increases rapidly with the increase in air density (for lower altitudes).

The thermal footprint of the simulated vehicles is relatively large, for two reasons (the engine presence is not taken into account): the first reason is the high temperatures and heat rates at the surface of the vehicles, especially at their leading edges and (more intense) at their nose region. The corresponding temperatures increase as the flight altitude decreases, due to the higher density of air. The second reason is the existence of a high-temperature wake behind the vehicles, which substantially increases their thermal footprint, rendering them potentially more easily observable. This observation, for the waverider design, is valid for all the flight altitudes that have been simulated in this work.

It is interesting that the simulated temperatures are higher at the lower surface of the waverider design (where the exposed surface is also larger), compared to the upper surface of the vehicle.

As the flow simulations (especially with the DSMC solver) are of high computational cost, it is difficult (and time consuming) to obtain detailed simulation results for many different flight conditions (different angles of attack, different altitudes and Mach numbers, etc.). Therefore, an extensive simulation campaign is required, if such information is necessary.

Concerning the computation of the infrared signature of the vehicles in the various simulated flow conditions, this requires specialized software, which is not currently available. As it was previously discussed, infrared signature depends on several factors, including the shape and size of the object, temperature and emissivity, reflection of external sources from the object's surface, the background against which it is viewed, and the waveband of the detecting sensor. All these factors should be taken into account in the simulation procedure to address the infrared signature of the simulated vehicle in various conditions.

As future work it would be interesting to:

- Simulate for different flow conditions (different angles of attack, flight altitudes, Mach numbers).
- Explore sensitivity analyses to understand how changes in design parameters impact vehicle performance and efficiency (however, such investigations require large computational resources).
- Possible use of specialized software, in order to simulate the infrared signature of the corresponding vehicles, based on the computed temperature fields. This depends on the availability of such software.

10. Bibliography

[1] J. Anderson Jr, *Hypersonic and High-Temperature Gas Dynamics*, Second Edition: *AIAA*, 2006.

[2] https://www.af.mil/About-Us/Fact-Sheets/Display/Article/104467/x-51a-waverider/.

[3] R.T. Voland, L. D. Huebner, C. R. McClinton, "X-43A Hypersonic vehicle technology development", in *Acta Astronautica*, 59, pp. 181-191, 2006.

[4] I.M. Blankson, S. Schneider, "Hypersonic Engine Using MHD Energy Bypass with a Conventional Turbojet", in *12th AIAA International Space Planes and Hypersonic Systems and Technologies Conference,* Norfolk, Virginia, USA, 2003; paper no. AIAA-2003-6922.

[5] J.J. Bertin, *Hypersonic Aerothermodynamics*, AIAA Education Series, New York, New York, 1994.

[6] R.S. Fry, "A Century of Ramjet Propulsion Technology Evolution", in Journal of Propulsion and Power, 20(1), pp. 27-58, 2004.

[7] D.R. Sandlin, and D.N. Pessin, *Aerodynamic Analysis of Hypersonic Waverider Aircraft*, *NASA-CR-192981*, 1993.

[8] T.R.F. Nonweiler, "Delta wings of shape amenable to exact shock wave theory", in *J. Royal Aero. Society*, 67, p. 39, 1963.

[9] D.R. Sandlin, and D.N. Pessin, "Aerodynamic Analysis of Hypersonic Waverider Aircraft", *NASA-CR-192981*, 1993.

[10] D. Sziroczak, and H. Smith, "A review of design issues specific to hypersonic flight vehicles", in *Progress in Aerospace Sciences*, 84, pp. 1-28, 2016.

[11] T.-T Zhang, Z.-G. Wang, W. Huang, L. Yan, "Parameterization and optimization of hypersonic-gliding vehicle configurations during conceptual design", in *Aerospace Science and Technology*, 58, pp. 225–234, 2016.

[12] K. Kontogiannis, *On Developing Efficient Parametric Geometry Models for Waverider-based Hypersonic Aircraft*, Ph.D. Thesis, University of Southampton, U.K., 2017.

[13] J. Son, C. Son, K. Yee, "A Novel Direct Optimization Framework for Hypersonic Waverider Inverse Design Methods", in *Aerospace*, 9, p. 348, 2022.

[14] J.W. Flower, "Configurations for high supersonic speeds derived from simple shockwaves and expansions", in *Royal Aeronautical Society Journal*, 67, pp. 287-290, 1963.

[15] D. Kuchemann, *The aerodynamic design of aircraft: a detailed introduction to the current aerodynamic knowledge and practical guide to the solution of aircraft design problems*, Oxford Pergamon Press, 1978.

[16] K.G. Bowcutt, "Multidisciplinary optimization of airbreathing hypersonic vehicles", in *Journal of Propulsion and Power*, 17(6), pp.1184-1190, 2001.

[17] C.E. Cockrell Jr., "Interpretation of waverider performance data using computational fluid dynamics", in*Journal of Aircraft*, 31(5), pp. 1095-1100, 1994.

[18] S. Corda, and J. Anderson Jr., "Viscous optimized hypersonic waveriders designed from axisymmetric flow fields", in *26th Aerospace Sciences Meeting*, pp. 369, 1988.

[19] T.R.F. Nonweiler, "Aerodynamic problems of manned space vehicles", in *Royal Aeronautical Society Journal*, 63, pp. 521-528, 1959.

[20] J.D. Anderson, *Introduction to Flight*, 4th ed. Boston: McGraw-Hill, 2000.

[21] J.J. Bertin, *Hypersonic Aerothermodynamics*, AIAA Education Series, New York, New York, 1994.

[22] J.J. Bertin, R.M. Cummings, "Critical Hypersonic Aerothermodynamic Phenomena", in *Annu. Rev. Fluid. Mech.*, 38, pp. 129-157, 2006.

[23] P. Rodi, "Geometrical relationships for osculating cones and osculating flowfield waveriders", in *49th AIAA Aerospace Sciences Meeting Including the New Horizons Forum and Aerospace Exposition*, paper 2011-1188, 2011.

[24] L.L. Chen, X.L. Deng, Z. Guo, Z.X. Hou, and W.K. Wang, "A novel approach for design and analysis of volume-improved osculating-cone waveriders", in *Acta Astronautica*, 161, pp. 430-445, 2019.

[25] W.F. Santos, "Bluntness impact on lift-to-drag ratio of hypersonic wedge flow", *Journal of Spacecraft and Rockets*, 46(2), pp. 329-339, 2009.

[26] X.Q. Chen, Z.X. Hou, J.X. Liu, and X.Z. Gao, "Bluntness impact on performance of waverider", *Computers & Fluids*, 48(1), pp. 30-43, 2011.

[27] D.J. Tincher, and D.W. Burnett, "Hypersonic waverider test vehicle-a logical next step", *Journal of Spacecraft and Rockets*, 31(3), pp. 392-399, 1994.

[28] M.A. Gallis, J.R. Torczynski, S.J. Plimpton, D.J. Rader, and T. Koehler, "Direct Simulation Monte Carlo: The quest for speed", in *Proceedings of the 29th Rarefied Gas Dynamics (RGD) Symposium*, Xi'an, China, July 2014.

[29] J.M. Zhan, Y.T. Li, W.H.O. Wai, and W.Q. Hu, "Comparison between the Q criterion and Rortex in the application of an in-stream structure", in *Physics of Fluids*, 31(12), p. 121701, 2019.

[30] J. Jeong, and F. Hussain, "On the identification of a vortex", in *Journal of Fluid Mechanics*, 285, pp. 69-94, 1995.

[31] W. Huang, L. Ma, Z. Wang, M. Pourkashanian, D.B. Ingham, S. Luo, and J. Lei, "A parametric study on the aerodynamic characteristics of a hypersonic waverider vehicle", in *Acta Astronautica*, 69, pp. 135-140, 2011.

[32] M.W. Oppenheimer, and D.B. Doman, "A Hypersonic Vehicle Model Developed With Piston Theory", in *AIAA Atmospheric Flight Mechanics Conference and Exhibit*, 21 - 24 August 2006, Keystone, Colorado, USA.

[33] M.A. Bolender, D.B. Doman, "A Non-Linear Model for the Longitudinal Dynamics of a Hypersonic Airbreathing Vehicle", in *AIAA Proceedings of the 2005 Guidance, Navigation and Control Conference*, paper no. 2005-6255, August 2005.

[34] C.M. Rondeau, T.R. Jorris, *X-51A Scramjet demonstrator program: waverider ground and flight test*, Air Force Flight Test Center Edwards AFB, CA Test Wing (412th), Operations Group (412th)/Flight Test Squadron (413th), 2013.

[35] R.S. Fry, "A Century of Ramjet Propulsion Technology Evolution", in *Journal of Propulsion and Power*, 20(1), pp. 27-58, 2004.

[36] C. McClinton, et al.,"X-43-scramjet power breaks the hypersonic barrier: Dryden lectureship in research for 2006", in *44th AIAA Aerospace Sciences Meeting and Exhibit*, 2006

[37] J. Bertin Jr., *Hypersonic Aerothermodynamics*, *AIAA*, 1994.

[38] D.S. Dolling, "Fifty Years of Shock-Wave/Boundary-Layer Interaction Research", in *AIAA Journal*, 39(8), 2001.

[39] M. Holden, et al., "Studies of aerothermal loads generated in regions of shock/shock interaction in hypersonic flow", in *26th Aerospace Sciences Meeting*, 1988.

[40] W. Heiser, D. Pratt, D. Daley, U. Mehta, *Hypersonic Airbreathing Propulsion*, *AIAA*, 1994.

[41] G. Choubey, K. M. Pandey, A. Maji, T. Deshamukhya, "A brief review on the recent advances in scramjet engine", in *AIP conference proceedings*, 1859(1), July 2017.

[42] Y. Kaikai, et al. "Optimization and analysis of inverse design method of maximum thrust scramjet nozzles", in *Aerospace Science and Technology,* 105, October 2020, 105948.

[43] F. Christin, "CMC materials for space and aeronautical applications", in *Ceramic matrix composites: fiber reinforced ceramics and their applications*, pp. 327-351, 2008.

[44] Yang Ya-zheng, Jia-ling Yang, Dai-ning Fang, "Research progress on thermal protection materials and structures of hypersonic vehicles", in *Applied Mathematics and Mechanics,* 29, pp. 51-60, 2008.

[45] secretprojects.co.uk/threads/darpa-boeing-x-51a-waverider.7406/page-11.

[46] J.M. Hank, J.S. Murphy, R.C. Mutzman, "The X-51A Scramjet Engine Flight Demonstration Program", in *15th AIAA International Space Planes and Hypersonic Systems and Technologies Conference*, 28 April - 1 May 2008, Dayton, Ohio, paper no.: AIAA 2008-2540.

[47] A.H. Boudreau, "Hypersonic Air-Breathing Propulsion Efforts in the Air Force Research Laboratory", in AIAA/CIRA 13th International Space Planes and Hypersonics Systems and Technologies, paper no.: AIAA 2005-3255.

[48] S.R. Allmaras, T.J. Forrester, and P.R. Spalart, "Modifications and clarifications for the implementation of the Spalart-Allmaras turbulence model", *In Seventh international conference on computational fluid dynamics (ICCFD7)*, vol. 1902, Jul 9 2012.

[49] M. Dahlgren, Getting on Track, *Space and Airborne Sensors for Hypersonic Missile Defense*, Center for Strategic & International Studies, Dec. 2023.

[50] https://www.lockheedmartin.com/en-us/products/sbirs.html.

[51] https://www.spaceforce.mil/About-Us/Fact-Sheets/Article/2197774/defense-support-program-satellites/.

[52] https://spacecenter.org/what-are-the-van-allen-radiation-belts/.

[53] https://en.wikipedia.org/wiki/Space-Based_Infrared_System.

[54] https://en.wikipedia.org/wiki/Infrared_signature.

[55] T.J. Horvath, M.F. Cagle, J.H. Grinstead, D.M. Gibson, "Remote Observations of Reentering Spacecraft Including the Space Shuttle Orbiter", IEEE Aerospace Conference, Big Sky, MT, 2013.

[56] Y. Zhou, et al., "Infrared simulation of aircraft rear fuselage based on a coupled CFD method" International Journal of Turbo & Jet-Engines, 40, pp. s635-s644, 2023. https://doi.org/10.1515/tjj-2022-0081.

[57] Q. Niu, D. Fu, S. Dong, H. Tan, "A simplified model for fast estimating infrared thermal radiation of low-altitude under-expanded exhaust plumes", International Journal of Heat and Mass Transfer, 136, pp. 276-287, 2019.

[58] J. Li, et al., "Analysis of Space-Based Observed Infrared Characteristics of Aircraft in the Air", Remote Sens., 15, 535, 2023.

[59] S.P. Mahulikar, H. R. Sonawane, G. Arvind Rao, "Infrared signature studies of aerospace vehicles", Progress in Aerospace Sciences, 43, pp. 218–245, 2007.

[60] K. Beier, "Infrared Radiation Model For Aircraft And Reentry Vehicle", 32nd Annual International Technical Symposium on Optical and Optoelectronic Applied Science and Engineering, San Diego, CA, United States, 1988. https://doi.org/10.1117/12.948320.

[61] E. Bakker, M. Fair, H. Schleijpen, "Modeling multispectral imagery data with NIRATAM v3.1 and NPLUME v1.6", AeroSense '99, Orlando, FL, United States, 1999. https://doi.org/10.1117/12.352936.

[62] https://www.ansys.com/products/missions/ansys-stk.

[63] https://www.ansys.com/content/dam/amp/2022/june/webpage-requests/stk-product-page/brochures/stk-premium-space-brochure.pdf.

[64] https://www.ansys.com/content/dam/amp/2022/june/webpage-requests/stk-product-page/brochures/stk-premium-air-brochure.pdf.